

ABSTRACT

CHENG, PEI-YUAN. Influence of Residual Stress and Heat Affected Zone on Fatigue Failure of Welded Piping Joints. (Under the direction of Dr. Tasnim Hassan.)

In recent decades, some unexpected fatigue failure occurred in welded joint of metal structures under cyclic loading. In many cases, the cause for the failure could not be detected. A study at NC State University revealed that welding procedure could be one of the factors that was not appropriately considered in current design methodologies. The welding procedure can influence the strain response near weld toe in two ways: one is by generating residual stress, and the other is changing material properties in the heat affected zone (HAZ). It was the primary objective in this investigation to determine the influence of these two factors on strain response by conducting experiments and performing numerical simulations of welded piping joints.

In the experimental study a series of residual stress data were measured, using x-ray and neutron diffraction techniques, for welded piping joints. The measured results revealed that the initial maximum compressive residual stress of stainless steel piping joints is higher than the yield stress of base metal. Moreover, the axial residual stresses of stainless steel piping joints are mostly relaxed after 5 cycles. The change of mechanical material properties due to high temperature exposure was studied by conducting experiments on tubular specimens. It was obtained that some mechanical material properties changed after subjecting to high temperature cycles, and the changed material was correlated to the peak temperatures. A modified thermo-mechanical material heterogeneity model was then developed to improve the initial residual stress simulation at the weld toe. The heterogeneous material properties coupled with the Chaboche model were used for subsequent fatigue response simulation. Quarter-point elements were applied at the stress concentration locations. The analysis results showed that fatigue response and residual stress relaxation can be simulated well. Final two simulations in this research showed that the presence of initial residual stress influences strain amplitude and strain mean, both of which could influence the fatigue life of welded joints.

Influence of Residual Stress and Heat Affected Zone on Fatigue Failure of Welded Piping Joints

by
Pei-Yuan Cheng

A dissertation submitted to the Graduate Faculty of
North Carolina State University
in partial fulfillment of the
requirements for the Degree of
Doctor of Philosophy

Civil Engineering

Raleigh, North Carolina

2009

APPROVED BY:

Dr. K. Linga Murty

Dr. G. Mahinthakumar

Dr. Murthy N. Guddati

Dr. Tasnim Hassan
Chair of Advisory Committee

DEDICATION

This dissertation is dedicated to:

My father Cheng Chao Tien, my mother Tung Chun Hui, and my sister I-Wen Cheng.

題獻

本論文獻給:

我的父親 鄭昭典, 母親 董春惠, 以及姊姊 鄭依雯

BIOGRAPHY

Pei-Yuan Cheng was born in Pingtung, Taiwan. He obtained his Bachelor of Science degree in Civil Engineering from I-Shou University, Kaohsiung, Taiwan in 1995. He completed his Master of Science degree in Civil Engineering from University of New Mexico, Albuquerque, NM in 2003. He joined the Ph.D. program in Civil Engineering at North Carolina State University, Raleigh in the fall of 2003. His research interests are experimental and numerical studies of welded joints, metallic material, and steel structures.

ACKNOWLEDGEMENTS

I want to express the utmost appreciation and respect to my advisor Dr. Tasnim Hassan for his guidance, encouragement, and advice throughout my academic experience at NCSU. He continuously supports me and is always available for discussion. It has truly been an honor to work with him.

Greatest thanks are also given to other graduate committee members, Dr. K. Linga Murty, Dr. G. Mahinthakumar, Dr. Murthy N. Guddati, and Dr. Yong Zhu who gave valuable advice and support during the course of work.

I would also like to thank the staff members of the High Temperature Materials Laboratory at Oak Ridge National Laboratory, specifically Dr. Camden Hubbard and Dr. Thomas Watkins, for their time and effort invested in this research.

I would like to gratefully acknowledge financial support provided by the National Science Foundation, the Center for Nuclear Power Plant Structures, Equipment, and Piping, and the Department of Civil Engineering without which this research could not have been conducted.

I also want to give great appreciation to Patricia Clayton, Thomas Knight, and Darwin D. (Jake) Rhoads for their help on material testing and experimental setup. Special thanks go to Shree Krishna for his assistance in finite element simulation and material parameters determination.

TABLE OF CONTENTS

LIST OF TABLES	viii
LIST OF FIGURES	ix
CHAPTER 1 Introduction	1
BACKGROUND AND MOTIVATION	1
SCOPE AND ORGANIZATION	3
CHAPTER 2 Fatigue Failure Mechanisms of Small Bore Welded Piping Joints	5
ABSTRACT	5
INTRODUCTION	6
LOW-CYCLE FATIGUE EXPERIMENTS ON WELDED PIPING JOINTS	7
Experimental Setup and Specimens	7
Test Results and Discussions	11
Butt-Weld Specimen BW1	11
Socket-Weld Specimen SW1	18
Socket-Weld Specimens SW2 and SW3	19
Strain Gage Zero-Shift	21
SIMULATION	25
Thermal Analysis of Welding Process	25
Residual Stress Simulation of welded Joints	30
Residual Stress Analysis for Socket Welded Joints	33
Fatigue Response Simulation for Socket-Welded Joints	37
DISCUSSION AND CONCLUSIONS	41
CHAPTER 3 Residual Stresses in Small Bore Socket-Welded Piping Joints under Low-Cycle Fatigue Loading	43

ABSTRACT	43
INTRODUCTION	44
WELDED SPECIMENS	47
TECHNIQUES OF RESIDUAL STRESS MEASUREMENTS.....	48
ERRORS OF X-RAY DIFFRACTION RESIDUAL STRESS MEASUREMENTS	50
RESULTS OF RESIDUAL STRESS MEASUREMENTS	51
INFLUENCE OF WELD JOINT GEOMETRY	51
INFLUENCE OF WELD JOINT MATERIAL	53
INFLUENCE OF THE NUMBER OF FATIGUE CYCLE	55
INFLUENCE OF FORCE VERSUS DISPLACEMENT-CONTROLLED CYCLES	57
INFLUENCE OF DEPTH AT THE WELD TOE ON RESIDUAL STRESS	58
SIMULATION OF RESIDUAL STRESS	60
HETEROGENEOUS MATERIAL PROPERTIES DUE TO WELDING	60
RESIDUAL STRESS SIMULATION USING THE MODIFIED THERMAL MODEL	68
EFFECT OF WELD SEQUENCE ON THE INITIAL RESIDUAL STRESS.....	72
CONCLUSIONS	76
ACKNOWLEDGEMENTS.....	77
CHAPTER 4 Improved Numerical Scheme for Simulating Fatigue Responses of Small Bore Welded Piping Joints	79
ABSTRACT	79
INTRODUCTION	80
FATIGUE RESPONSE SIMULATION SCHEME	84
HETEROGENEOUS MATERIAL PROPERTIES	84
CHABOCHE MODEL PARAMETERS DETERMINATION	88
TECHNIQUE OF INCORPORATING MATERIAL HETEROGENEITY IN ANSYS .	91

QUARTER-POINT ELEMENTS AT WELD TOE AND CONVERGENCE STUDY...	93
FATIGUE RESPONSE SIMULATIONS FOR SOCKET WELDED JOINTS.....	96
INFLUENCE OF MATERIAL TYPES AND MATERIAL MODELS.....	96
SIMULATION OF RESIDUAL STRESS RELAXATION.....	100
INFLUENCE OF RESIDUAL STRESS ON FATIGUE RESPONSE.....	103
CONCLUSIONS	107
CHAPTER 5 Conclusions and Recommendations.....	110
CONCLUSIONS	110
Fatigue failure mechanism (Chapter 2).....	110
Residual stress (Chapter 3)	111
Improved fatigue response simulation (Chapter 4).....	111
RECOMMENDATIONS FOR FUTURE RESEARCH.....	112
REFERENCES.....	114

LIST OF TABLES

Table 1.1 Overview of experiments in Lu [2003]	2
Table 2.1. Summary of welded piping joints fatigue tests	11
Table 2.2. Temperature-dependent thermal and mechanical material properties of SS304 [data from Li, 1995, Brickstad and Josefsen, 1998].....	26
Table 2.3. Temperature-dependent mechanical material data of SS304 [data from Kang et al., 2005, and Brickstad and Josefsen, 1998]	31
Table 3.1. Lists of specimens, fatigue loading, and residual stress measurement cycles.....	47
Table 3.2. Weld sequences for initial residual stress simulation.....	72
Table 4.1. Chaboche model and Voce hardening model parameters of temperature conditioned and unconditioned SS304.....	89
Table 4.2. Chaboche model and Voce hardening model parameters of five material sets for fatigue simulation.	91

LIST OF FIGURES

Fig. 2.1. Cantilever setup for welded piping joint fatigue test.	8
Fig. 2.2. Butt- and socket-welded piping joint specimens.....	9
Fig. 2.3. Schematic diagrams of the (a) butt-weld specimen, and (b) socket-weld specimen.....	9
Fig. 2.4. Low-cycle fatigue response at every 20th cycle from the butt-weld fatigue test; (a) load-displacement response, (b) axial-circumferential strain response at the top toe.	13
Fig. 2.5. Amplitude and mean of load responses as a function of number of cycles	13
Fig. 2.6. Positive and negative peaks at the top weld toe at every 10th cycle from the butt weld test shown in Fig. 2.4.....	14
Fig. 2.7. Axial and circumferential strain responses from a straight pipe cyclic bending test at steady internal pressure [data from Rahman et al. 2008].	15
Fig. 2.8. Axial strain peaks (every 10th cycle) at the mid-length pipe top.....	16
Fig. 2.9. Amplitude and mean of axial strain cycles (every 10th cycle) at top and bottom toes.	17
Fig. 2.10. Axial strain amplitudes from the butt and socket weld tests.....	19
Fig. 2.11. Axial strain means from the butt and socket weld tests	19
Fig. 2.12. Axial strain amplitudes at fatigue crack locations from the four butt- and socket-weld tests.	21
Fig. 2.13. Axial strain means at fatigue crack locations from the four butt- and socket-weld tests.....	21
Fig. 2.14. Trial experiment for strain gage zero-shift. (a) Setup of extensometer and strain gages on tubular specimen. (b) Strain-controlled load history.....	23
Fig. 2.15. (a) The relationship of strain gage zero-shift and cycle numbers under various strain amplitudes. (b) Zero-shift rates against strain amplitudes and a quadratic fit.....	23
Fig. 2.16. Zero-shift error corrected axial strain means at fatigue crack locations from the four butt- and socket-weld tests.....	24
Fig. 2.17. An example of element birth and death.	27
Fig. 2.18. The 2D finite element model for a two-pass butt-welded plate joint.....	28

Fig. 2.19. Calculated temperature history during the 1st welding pass in comparison with the experimental data from Murugan et al. [1999].	28
Fig. 2.20. (a) The 3D finite element model for four-pass girth-welded pipe; only half of the pipe is simulated (b) the cross section of groove geometry and weld pass sequence	29
Fig. 2.21. Comparison of temperature history between numerical and experimental results; experimental data from Li [1995].	30
Fig. 2.22. Temperature-dependent stress-strain experimental responses and corresponding bilinear fit	31
Fig. 2.23. Measured and simulated residual stress distributions. (a) Axial residual stress at the outer surface, (b) axial residual stress at the inner surface, (c) circumferential residual stress at the outer surface, and (d) circumferential residual stress at the inner surface.	32
Fig. 2.24. Finite element model of three-pass socket-welded stainless steel pipe joints.	33
Fig. 2.25. Illustrations of finite element modeling of the progressive welding bead deposition during the first weld pass	34
Fig. 2.26. Contact elements CONTACT52 added to the model between the outer surface of the pipe and the inner surface of socket during welding and fatigue loading	34
Fig. 2.27. Illustration of moving temperature (in Kelvin) field during the final quarter welding (a, b, and c) and cooling (d) of the last welding pass.	35
Fig. 2.28. Axial residual stress distribution on pipe outer surface; Angle is measured from location A which is the location of the first tack weld as shown in Fig. 2.30.	36
Fig. 2.29. Circumferential residual stress distribution on pipe outer surface; Angle is measured from location A which is the location of the first tack weld as shown in Fig. 2.30.	37
Fig. 2.30. Finite element model for fatigue simulation under displacement-controlled loading.	38
Fig. 2.31. A comparison of first 5 cycles of force-displacement hysteresis curve from experiment and simulation	39
Fig. 2.32. Load response versus number of cycles from experiment and simulation.	39
Fig. 2.33. Axial strain response at top 5mm from weld toe versus number of cycles from experiment and simulation	40
Fig. 2.34. Axial residual stress distribution on top of pipe outer surface after various cycles from simulation	41

Fig. 3.1. (a) Tack weld and quarter circumferential weld sequences. Sequence of tack welds is A-C-B-D, before circumferential quarter welding in the sequence of 1-1, 1-2, 1-3, 1-4, 2-1, ..., 3-4. (b) Socket weld and three weld bead sequence. (c) Butt weld and 3 weld bead sequence	48
Fig. 3.2. Neutron diffraction measurements of residual stress of piping joints along (a) radial, (b) circumferential, and (c) axial directions	49
Fig. 3.3. (a) Measurement locations on butt weld and socket weld piping joints. (b) X-ray diffraction measurement setup. (c) Neutron diffraction measurement setup.	50
Fig. 3.4. Measured residual stress in reproducibility test (a) axial data, (b) circumferential data. [from Humphreys 2004]	51
Fig. 3.5. Initial axial residual stresses in a butt weld, ASME socket weld and a modified socket weld	53
Fig. 3.6. Initial axial residual stress in stainless steel and carbon steel socket welded joints.....	54
Fig. 3.7. Axial residual stress relaxation of SW7 stainless steel socket welded joint with fatigue cycle N	55
Fig. 3.8. Axial residual stress relaxation of stainless steel socket welded joints with fatigue cycle N	56
Fig. 3.9. Axial residual stress relaxation of carbon steel socket welded joints with fatigue cycle N ...	57
Fig. 3.10. Relaxation of residual stresses of SW9 (force-controlled) and SSPC3 (displacement-controlled) after 100 fatigue cycles.	58
Fig. 3.11. Residual stresses measured at various depths from outer surface at various distances from the toe using neutron diffraction technique (a) axial data before fatigue loading, (b) circumferential data before fatigue loading, (c) radial data before fatigue loading, and (d) after 100 cycles.	59
Fig. 3.12. Temperature history at various locations of the heat affected zone during welding.	61
Fig. 3.13. Tubular specimen dimensions and the types of cyclic loading tests	62
Fig. 3.14. Monotonic responses of unconditioned and temperature conditioned specimens	63
Fig. 3.15. Yield stress evolution of SS304 specimens with peak temperature of temperature conditioning cycle and an elliptic function fit of yield stress evolution.....	64
Fig. 3.16. Temperature dependent experimental yield stress of SS304 and their exponential function fit. Solid circles represent yield stresses data obtained from Kang et al. [2005] and Brickstad and Josefsen [1998].....	65
Fig. 3.17. Basic thermal model (ABCD) and modified thermal model for determining temperature-dependent yield stress evolution.....	66

Fig. 3.18. Temperature-dependent yield stress and plastic modulus of SS304 for five temperature levels in modified thermal model: (a) yield stress evolution, (b) tangent modulus evolution.	68
Fig. 3.19. Finite element mesh of the three-pass SS304 socket-welded piping joint	69
Fig. 3.20. Material state of elements near welding zone. Material sets assigned to elements depend on the peak temperature of the element before and after specific welding steps. (a) before weld starts, (b) after the first tack weld, and (c) after all weld passes are completed and the specimen reaches room temperature.....	70
Fig. 3.21. Initial axial residual stresses from x-ray and neutron diffraction and finite element simulations.....	71
Fig. 3.22. (a) Three-pass quarter-weld sequence. (b) Simulation results of axial residual stress distribution along pipe outer surface from weld toe.....	73
Fig. 3.23. (a) Four-pass, quarter-weld sequence. (b) Simulation results of axial residual stress distribution along pipe outer surface from weld toe.....	73
Fig. 3.24. (a) Four-pass, full-weld sequence (same start-stop location) (b) Simulation results of axial residual stress distribution along pipe outer surface from weld toe.	74
Fig. 3.25. (a) Four-pass, full-weld sequence (different start-stop locations). (b) Simulation results of axial residual stress distribution along pipe outer surface from weld toe.....	74
Fig. 4.1. Cantilever set-up for socket welded piping joint fatigue tests, and weld bead sequence of the specimen.....	83
Fig. 4.2. Finite element mesh of the three-pass SS304 socket-welded piping joint. The elements used in generating the mesh are 8-node SOILD 185.....	83
Fig. 4.3. Temperature history at various locations of the heat affected zone during a weld sequence.	85
Fig. 4.4. Experimental results of conditioned and unconditioned stainless steel SS304 specimens from uniaxial strain-controlled experiments. The temperatures shown in the figure are the specimen conditioning peak temperatures. (a) Axial stress-strain responses from the first cycle. (b) Amplitudes of axial stress peaks from each cycle versus the number of cycles.....	86
Fig. 4.5. Biaxial ratcheting experiments on conditioned and unconditioned stainless steel SS304 coupons. (a) Loading path prescribed. (b) Means of circumferential strain from each cycle versus the number of cycles.	87
Fig. 4.6. Axial, force-controlled loading cycles prescribed in the uniaxial ratcheting experiments. ...	88

Fig. 4.7. Axial force-controlled experimental results of 1050°C-conditioned SS304 coupon, (a) axial stress-strain responses. (b) Mean and amplitude of axial strain from each cycle versus the number of cycles.....	88
Fig. 4.8. Axial stress-strain responses of unconditioned base metal and temperature-conditioned coupons from uniaxial strain-controlled experiments and fit for Chaboche model parameter determination.....	90
Fig. 4.9. Material sets assigned to elements for fatigue response simulation.....	92
Fig. 4.10. Profile of various 3D mesh densities near weld for convergence study.....	93
Fig. 4.11. Numerical simulations of axial strain response at weld toe under a displacement-controlled load from three mesh models. All of the elements are eight-noded SOLID185 elements.	94
Fig. 4.12. Eight-node SOLID185 elements around weld toe are replaced by twenty-node SOLID186 elements for representing the stress-concentration at the weld toe. (a) initial mesh around weld toe composed of SOLID185 elements, (b) modified mesh around weld toe composed of twenty-node SOLID186, connecting and eight-node elements.....	95
Fig. 4.13. Numerical simulations of axial strain response at weld toe under a displacement-controlled load from three modified mesh models with singular elements (SOLID186) at the weld toe.	96
Fig. 4.14. Force-displacement responses from experiment and simulations using various material types and models. (a) Homogeneous and bilinear (b) Heterogeneous and bilinear (c) Homogeneous and Chaboche (d) Heterogeneous and Chaboche	97
Fig. 4.15. Load response versus number of cycles from experiment and simulations using various material types and material models.	98
Fig. 4.16. Axial strain mean and amplitude responses on top pipe surface at 5mm from weld toe from experiment and simulations using various material types and models.....	100
Fig. 4.17. Loading path at loading end of welded piping joints for residual stress relaxation measurements and simulations.	101
Fig. 4.18. Axial residual stress results on top from simulation and experiment (a) before fatigue loading, (b) after 5 cycles, (c) after 20 cycles, (d) after 100 cycles.....	102
Fig. 4.19. Comparison of force-displacement responses from experiment and simulations; (a) simulation without initial residual stresses (b) simulation with initial residual stresses.	104
Fig. 4.20. Mean and amplitude force responses against the number of cycles from experiment and simulations; (a) simulation without initial residual stresses, (b) simulation with initial residual stresses.....	104

Fig. 4.21. Axial strain response at various distances (3mm, 19mm, and 38mm) from weld toe versus number of cycles from experiment and simulations of (a) without initial welding residual stress (b) with initial residual stress 105

Fig. 4.22. Axial strain responses at the weld toe as a function of the number of cycles from simulations with and without initial compressive residual stresses..... 107

CHAPTER 1

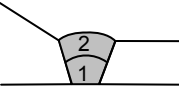
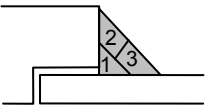
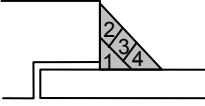
Introduction

BACKGROUND AND MOTIVATION

In recent decades, some unexpected fatigue failure occurred in welded joint of metal structures under cyclic loading. In many cases, the cause for the failure could not be detected. The occurrence of failure might indicate that some factors, which caused unexpected fatigue failure, were not considered in current design methodologies. A study at NC State University (Lu [2003]) revealed that welding procedure could be one of the factors that was not appropriately considered in current design methodologies. Lu [2003] conducted low-cycle fatigue loading tests on welded piping joints that were welded with various welding sequences as shown in Table 1.1 and found that their fatigue lives were quite different as also listed in Table 1.1. As the through-wall cracks of the specimens in Table 1.1 were all at the weld toe of the specimens, strain responses near weld toe were carefully examined. The experimental strain data near weld toe from all specimens were found noticeably different. These observations demonstrated that welding sequence affects strain response near weld toe during fatigue loading, and thus it was concluded that the welding sequence may affect fatigue live of welded joints.

The welding procedure can influence the strain response near weld toe in two ways: one is by generating residual stress, and the other is changing material properties in the heat affected zone (HAZ). The earlier factor was studied at NC State University by Humphreys [2004], who made an effort in measuring initial welding residual stress and its relaxation after fatigue loading for welded piping joints. The residual stress measurements were conducted at Oak Ridge National Laboratory (ORNL) using their x-ray diffraction instruments. It was observed from measured residual stresses that initial compressive residual stress near weld toe could be as high as the yield stress of the base metal, and the residual stresses were almost totally relaxed after hundred cycles.

Table 1.1 Overview of experiments in Lu [2003]

Joint type	Weld sequence	Welding procedure	Fatigue life
Butt-weld (BW1)		Quarter-circumferential	980
Socket-weld (SW1)		Quarter-circumferential	680
Socket-weld (SW2)		Quarter-circumferential	900
Socket-weld (SW3)		Full-circumferential	470

The study of residual stress was also a part of the research of Lu [2003], who performed 3D numerical simulation of welding procedure and fatigue loading on the piping joints using finite element program. On the numerical simulation of welding procedure, sequentially uncoupled nonlinear transient thermo-mechanical analyses with element birth/death feature for imitating the welding procedure were applied. From this welding simulation how the residual stresses are generated from high temperature cycles during welding was demonstrated. Next, fatigue response analysis with the presence of initial residual was conducted. Homogeneous material properties with bilinear material model were employed on the fatigue loading simulation. It was concluded from the simulation results that ratcheting response could not be simulated due to the deficiency of the constitutive models.

From the studies mentioned above some issues remain unclear. For instance, the measured residual stresses showed totally relaxed after hundred cycles, but the relationship of residual stress relaxation with the number of cycles is unknown. Another issue is that the numerical simulation need

to be improved, which would involve study of material properties at the heat affected zone (HAZ) and incorporation of advanced constitutive models for residual stress and fatigue response simulations. With the aim of further exploring the fatigue response, efforts have been made in this study to conduct more welded joint fatigue experiments, measure residual stresses, and perform numerical simulations on welded piping joint specimens.

SCOPE AND ORGANIZATION

The results of this dissertation research are presented in three chapters. Experimental strain responses of small bore welded piping joints under low-cycle fatigue loading from Lu [2003], Humphreys [2004], and current study are compared and discussed in Chapter 2. The difference of strain responses due to the effect of welding sequence is presented. Furthermore, a residual stress simulation and subsequent fatigue response simulation is introduced in Chapter 2. The simulation uses homogeneous base metal properties with bilinear material model for both residual stress and fatigue response simulations.

The study of residual stress is presented in Chapter 3. First, the techniques of measuring residual stress on welded piping joints using x-ray diffraction and neutron diffraction methods is introduced. Second, the measured residual stress of various specimens are illustrated, and the effect of weld design, material, fatigue loading cycles, load control type, depth, and measurement location on residual stress are presented. Third, the use of the heterogeneous material properties at the HAZ in influencing the residual stress and ratcheting response simulation is presented. Finally, simulations of residual stress for several weld sequences are performed, and the results are discussed.

The improved fatigue response simulation is presented in Chapter 4. The improvement was made by including the heterogeneous material properties in the Chaboche material model, and quarter-point

elements at the stress concentration point. A series of cyclic tests on tubular temperature-conditioned specimens to represent material heterogeneity at HAZ were conducted, and their material responses were used to determine material parameters for fatigue simulation. The simulations with and without the heterogeneous material properties are compared. Next, fatigue simulations paused at various intermediate fatigue lives for investigating the residual stress relaxation, and the simulations were verified by measured strain and residual stress data from Chapter 2 and 3. Finally, the fatigue response simulations, one with initial welding residual stress and the other one without initial residual stress, are performed. The effect of initial residual stress on fatigue strain response is presented in this chapter.

Finally, Chapter 5 presents important conclusions of the study and the recommendations for future research.

CHAPTER 2

Fatigue Failure Mechanisms of Small Bore Welded Piping Joints

ABSTRACT

Fatigue failures of small bore piping systems have historically occurred in nuclear power plants, resulting in unanticipated plant downtime and substantial financial loss. If the failures were not caused by defects, the reasons of the initiation of fatigue cracks were not clear in many cases. In order to understand the fatigue failure of welded piping joint, this study conducted a set of low-cycle fatigue experiments on butt- and socket welded piping joints in a cantilever setup. A novel observation made from the experimental responses is the influence of weld sequence on the weld toe fatigue crack initiation. The strain response, both amplitude and ratcheting, near the weld toe seems to be a function of weld sequence and thus influences the fatigue life of welded piping joints. It is observed that the fatigue cracks in all experiments occurred at the weld toe where both the strain amplitude and ratcheting is anticipated to be the largest. A question is raised about how significant is the strain-ratcheting phenomenon in influencing the fatigue crack initiation life at the weld toe. The occurrence of ratcheting under displacement-controlled cyclic loading is unexpected because of the strain-displacement kinematics. In addition, the ratcheting response of the welded joints is questionable because of the zero shift characteristics of the strain gages used. On the other hand, comparison of the welded joint ratcheting responses with those from the cyclic bending of straight pipe and material level experiments indicates that the residual stresses may induce ratcheting strain at the welded joints. At this location, there is no residual stress to induce ratcheting. In addition to the set of experiments stated above this study performed detailed thermo-mechanical analysis in order to explore the welded piping joints fatigue failure mechanism and attempt to address the questions raised in the study.

INTRODUCTION

Fatigue failures in nuclear power plants have resulted in unscheduled plant downtime and considerable financial loss [Smith, 1996, Vecchio, 1996]. An EPRI database shows that 642 fatigue failures have occurred at 86 different operating units over 20 years period [Gosselin, 1994, 2008]. Of those, 122 failures were caused by thermal fatigue and 520 were vibration related. Most of these fatigue failures occurred at welded-joints of small-bore piping or at fillet weld attachments under high- and low-cycle vibration conditions. A database of welded joint fatigue failures that include 74 case studies was developed at the Center for Nuclear Power Plant Structures, Equipment and Piping [Liu, 1998]. An analysis of the database reveals that 32 of these failures occurred in the period 1975-1989 and 42 in 1990-1994. These statistics indicate a growing number of fatigue failures, which is also anticipated due to the aging of structure.

Many of the fatigue failures in welded joints occurred within the first 10 years of life, much earlier than the estimated life of 40 years. These failures came as a surprise to the engineering community since the fatigue design methodologies are generally known to be conservative. Also, if the failures were not caused by defects, the reasons of the initiation of fatigue failure were not clear in many cases [Virginia, 1993]. Among the important factors of fatigue failure, such as, stress concentration, environment (thermal cycle and corrosive), loading and residual stress, the influence of residual stress is usually neglected in the low-cycle fatigue range due to the widely accepted assumption of residual stress relaxation to zero after a couple of inelastic loading cycles.

In addition, this study conducted a set of low-cycle fatigue experiments on butt- and socket welded piping joints in a cantilever setup. A novel observation made from the experimental responses is the influence of weld sequence on the weld toe fatigue crack initiation. The strain response, both amplitude and ratcheting, near the weld toe seems to be a function of weld sequence and thus influences the fatigue life of welded piping joints. It is observed that the fatigue cracks in all

experiments occurred at the weld toe where both the strain amplitude and ratcheting is anticipated to be the largest. A question is raised about how significant is the strain-ratcheting phenomenon in influencing the fatigue crack initiation life at the weld toe. The occurrence of ratcheting under displacement-controlled cyclic loading is unexpected because of the strain-displacement kinematics. In addition, the ratcheting response of the welded joints is questionable because of the zero shift characteristics of the strain gages used. On the other hand, comparison of the welded joint ratcheting responses with those from the cyclic bending of straight pipe and material level experiments indicates that the residual stresses may induce ratcheting strain at the welded joints. This argument is supported by the symmetric strain response (no ratcheting) at the mid-pipe length, which is located away from the welded joint. At this location, there is no residual stress to induce ratcheting. In addition to the set of experiments stated above this study performed detailed thermo-mechanical analysis in order to explore the welded piping joints fatigue failure mechanism and attempt to address the questions raised in the study. The experimental and analytical results from this study are presented below.

LOW-CYCLE FATIGUE EXPERIMENTS ON WELDED PIPING JOINTS

Experimental Setup and Specimens

Welded piping joints were tested in a cantilever setup as shown in Fig. 2.1. In this figure, it is shown that the welded joint to be tested is located near the heavy and stiff support column. The fatigue loading cycle is applied to the other end of the pipe using the actuator of a servo-hydraulic testing machine through a pin end fixture setup (Fig. 2.1). The pin end fixture consists of a self-aligning ball bearing and a pin, which is snugly fitted to the ball bearing and tightly attached to the end fixture. One of the pin end fixtures is tightly screwed to the actuator rod and the other welded to the specimen. The stiff support column is rigidly fastened to the T-slot table of the testing machine. End fixtures at both ends of the pipe specimen were machined with small access holes to fill the

specimen with oil and apply a small internal pressure of 100-150 psi (0.69-1.03 MPa), using a pneumatic pump, for detecting the occurrence of through-wall fatigue crack.

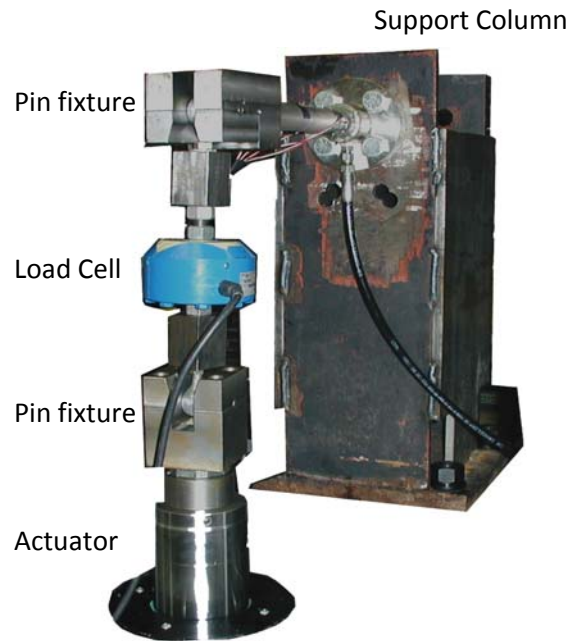


Fig. 2.1. Cantilever setup for welded piping joint fatigue test.

Test specimens for butt- and socket-welded joints are shown in Figs. 2.2 and 2.3. The material of the pipe specimen was stainless steel (SS) 304L and the weld filler was SS 308L. The butt- and socket ends and other end fixtures of the test specimens were machined from SS 304L blocks. The pipe specimen has a nominal diameter of 1.25 inches (31.75 mm) and wall thickness of 3/16 inches (4.76 mm). The length of the pipe in butt weld specimens was set to be 10.125 inches (257.18 mm) and that in socket weld specimens 11 inches (279.4 mm) in order to have 10.125 inches (257.18 mm) of pipe from weld toe to the loading point for both types of weld joint specimens. This requirement was set in order to have the same applied bending moment at the weld toe of both specimens. Weld joint dimensions were determined according to the ASME Code. Specimens with various weld sequences

were tested in order to demonstrate the influence of residual stress on the fatigue failure of welded piping joints at the weld toe.



Fig. 2.2. Butt- and socket-welded piping joint specimens

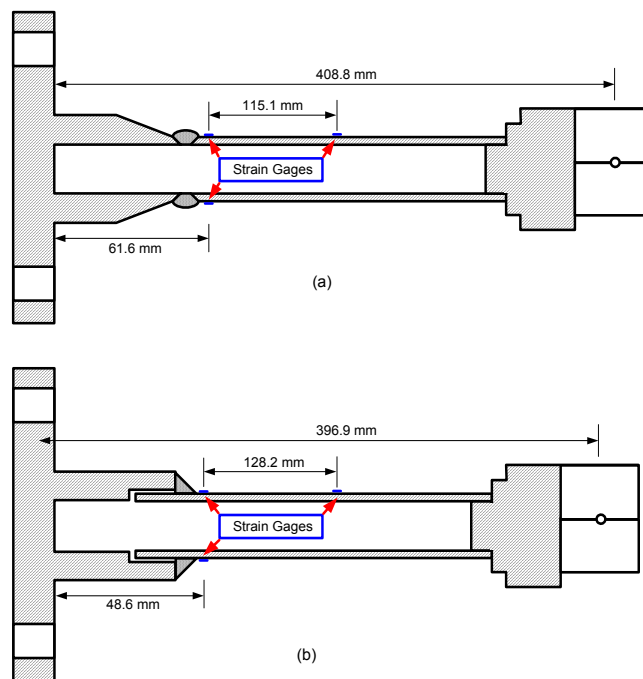


Fig. 2.3. Schematic diagrams of the (a) butt-weld specimen, and (b) socket-weld specimen.

Welding for all the specimens tested was carried out manually by a certified welder for nuclear power plant welding. Welding was performed in a vertical position of the specimens. In order to minimize distortion of the specimens due to welding, four tack welds were put first at circumferential quarter points. Subsequent to tack welds, welding was performed for each quarter of the circumference at a time. With this method of welding, distortion of specimens was found to be small (not noticeable with naked eyes) compare to full-circumferential welding for each pass. One socket weld specimen with full- circumferential welding for each pass was measured to have about 5° of distortion of the pipe compared to the end fixture. To minimize distortion from welding, another step taken was sufficient cooling period between each start and stop of welding passes.

The fatigue tests in the cantilever setup were performed by prescribing a displacement-controlled saw-tooth loading cycle with amplitude of 14.5 mm (0.57 inches). The period for each cycle was 4 seconds (1/4 Hz). During the fatigue test, the pipe was subjected to a small hydraulic pressure (varied between 100-150 psi [0.69-1.03 MPa]) in order to detect the number of cycles at which fatigue crack became through-wall. The cycle for initiation of the fatigue crack was also detected manually by frequently checking the critical weld toe area and monitoring strain changes.

Axial and circumferential strains were recorded at various locations using strain gages during fatigue tests. In most tests, three strain gages were used as shown in Fig. 2.3. Two biaxial, 90° stacked strain gages were set near the weld toe, one on the top and the other at the bottom of the specimen. These strain gages were set as close as possible to the weld toe. A uniaxial strain gage was set on the top, mid-length of the pipe (see Fig. 2.3). Other data monitored were forces using a 5000 lbs load cell (see Fig. 2.1), displacement using a Linear Variable Differential Transformer (LVDT), and pressure using a pressure gauge. All these measured parameters were digitized and stored at every 0.032 second using a LabView data acquisition program.

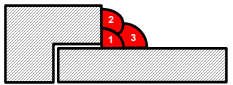
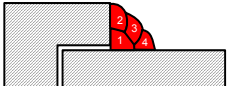
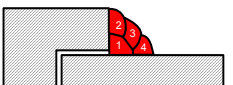
Test Results and Discussions

A total of four welded joints, one butt-weld and three socket-welds were tested (see Table 2.1). The specimen details and results are discussed below.

Butt-Weld Specimen BW1

The butt-welded joint was fabricated by conducting tack welds at quarter points first and then depositing two weld passes (see the inset in Table 2.1) using the quarter-circumference welding sequence. As mentioned in the last section, the fatigue test of the welded piping joints were performed using a cantilever setup (Fig. 2.1) and by prescribing a displacement controlled saw-tooth cycle of amplitude 14.5 mm (0.57 inches). The recorded load-displacement response at the loading end of the specimen is shown in Fig. 2.4a, where the hysteresis loops depict the inelastic response of the welded pipe specimen. The fatigue crack in this test was first noticed after 800 cycles exactly at the toe, at top of the specimen along the circumferential direction. The crack propagated through the thickness of the pipe after 980 cycles, which is when the oil started leaking and the test was stopped. No crack was observed at the bottom toe of the pipe.

Table 2.1. Summary of welded piping joints fatigue tests

Joint Type	No. of Passes	Weld Sequence	Weld Method	Cycles to Initial Crack	Cycles for Through Crack
Butt-Weld (BW1)	2		Quarter	800	980
Socket-Weld (SW1)	3		Quarter	500	680
Socket-Weld (SW2)	4		Quarter	560	900
Socket-Weld (SW3)	4		Full	300	470

The amplitude and mean of the force response as a function of number of cycle are shown in Fig. 2.5. In this figure, it is observed that the mean of the load cycle is almost zero, which means that the load response is almost symmetric. The force amplitude response in Fig. 2.5 demonstrates cyclically softening. The axial strain versus circumferential strain response from the top toe gage is shown in Fig. 2.4b. This figure demonstrates that both axial and circumferential strains are gradually increasing with cycles, which is known as ratcheting or sometime referred to as cyclic creep. Larger amplitude strain cycle and larger rate of ratcheting along the axial direction compared to the amplitude and rate of ratcheting along the circumferential direction explains the circumferential fatigue crack in this test.

For the readers unfamiliar with the ratcheting phenomenon, they are referred to, (i) a uniaxial ratcheting response, Fig. 3 in Hassan and Kyriakides [1992], where a stress-strain response under a uniaxial stress-controlled loading cycle with a mean stress is shown, (ii) a biaxial ratcheting response, Fig. 3 in Hassan and Kyriakides [1994b], where material responses under axial strain-controlled cycle and steady circumferential stress are shown, and (iii) a second biaxial ratcheting response, Fig. 6 in Hassan and Kyriakides [1994b], where material responses under axial stress-controlled cycle and steady circumferential stress are shown. In case of uniaxial ratcheting, the mean stress in the prescribed stress cycle is the driving force that induces ratcheting. For the first biaxial loading case, ratcheting occurred in the circumferential direction mainly due to the steady stress in this direction. For the second biaxial loading case, where prescribed loading in both axial and circumferential directions are stress-controlled, ratcheting of strains occurs in both directions. Similarly, ratcheting at a material point in a structure under cyclic loading can occur along the directions of stress-controlled cycle or steady stress. The readers referred to Hassan and Kyriakides [1992, 1994a, 1994b], Hassan et al. [1992] and Corona et al. [1996] for a detailed discussion on ratcheting.

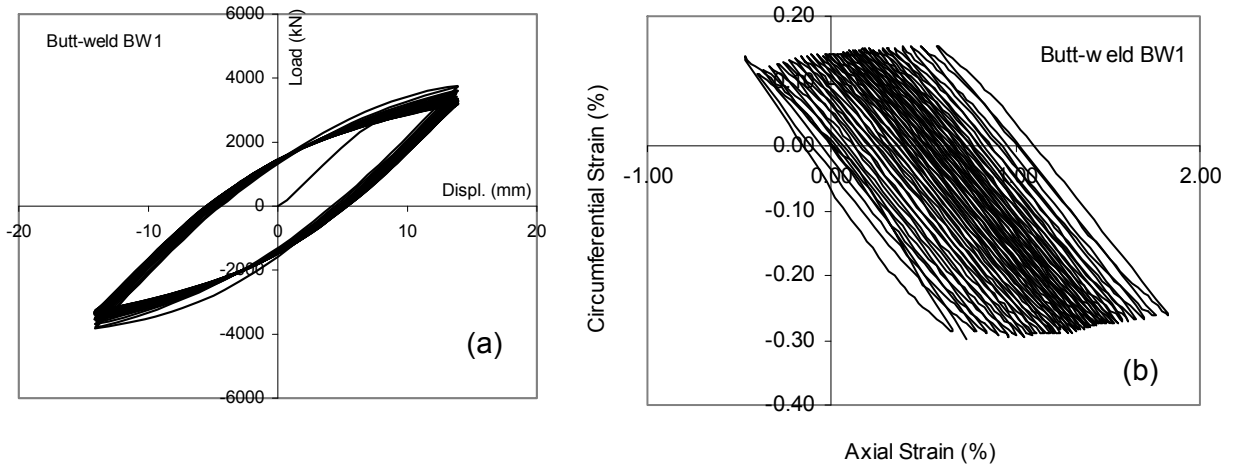


Fig. 2.4. Low-cycle fatigue response at every 20th cycle from the butt-weld fatigue test; (a) load-displacement response, (b) axial-circumferential strain response at the top toe.

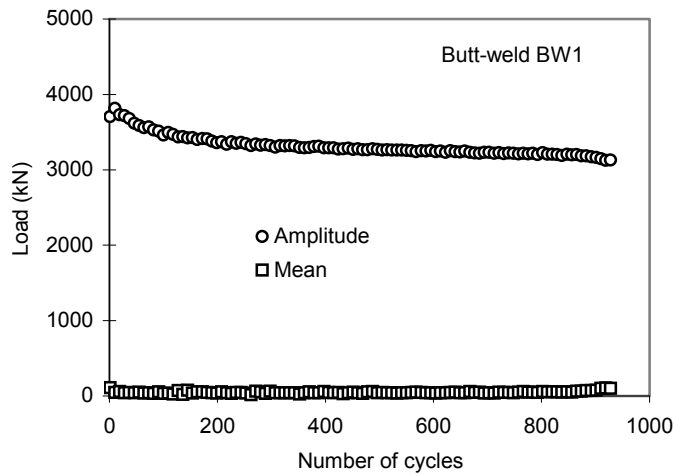


Fig. 2.5. Amplitude and mean of load responses as a function of number of cycles

For the butt-weld fatigue test presented above, the axial strain ratcheting response is shown in Fig. 2.6, where strains at both positive and negative load peaks at every 10th cycle are plotted as a function of the number of cycles. It is quite surprising to find that the axial strain is ratcheting in this test under displacement-controlled loading cycle. This is the first time that such a ratcheting response of the material at the weld toe is demonstrated. Hence the results are critically analyzed and discussed below.

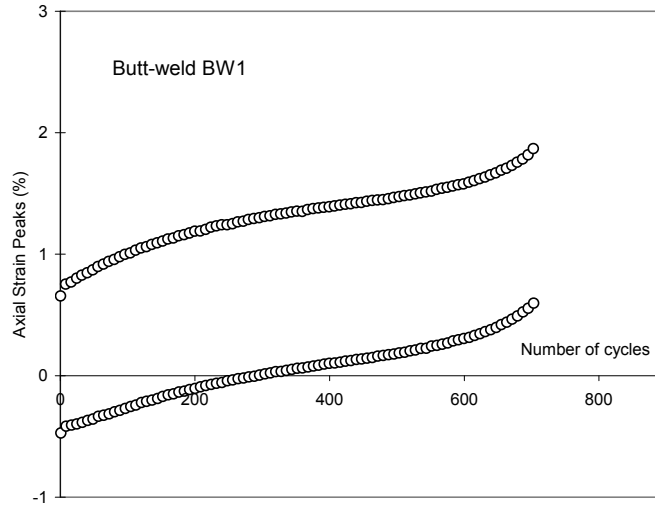


Fig. 2.6. Positive and negative peaks at the top weld toe at every 10th cycle from the butt weld test shown in Fig. 2.4.

In order to interpret butt-weld ratcheting response, response of a straight pipe subjected to fully-reversed, curvature-controlled (pure bending) cycle in the presence of internal pressure, developed by Rahman et al. [2008], is discussed first. The axial-circumferential strain response at the top mid-pipe section is shown in Fig. 2.7. It is seen in this figure that the axial strain response is almost fully reversible; a very small axial strain ratcheting is observed. However, considerable ratcheting in the circumferential direction is observed in this test. The ratcheting in the circumferential direction results from the circumferential stress induced mainly by the internal pressure. The circumferential ratcheting in this test may partly be induced by the ovalization of the pipe (See Corona et al. [1996] for related discussion).

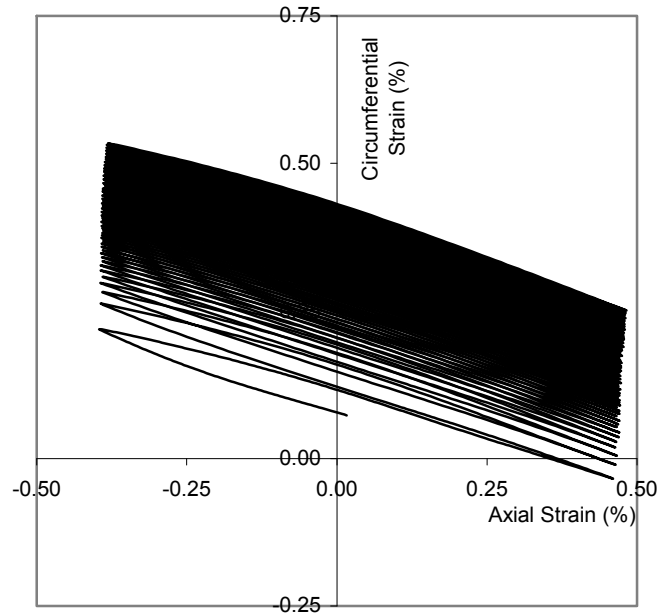


Fig. 2.7. Axial and circumferential strain responses from a straight pipe cyclic bending test at steady internal pressure [data from Rahman et al. 2008].

What is surprising in the butt-weld test is that even under fully reversed displacement-controlled cycle, the axial strain has ratcheted about 1.21% in 700 cycles, whereas in the straight pipe cyclic bending test almost no axial strain ratcheting is observed. So, hypothesis drawn from this observation is that the residual stresses at the weld toe has acted as a mean stress to the stress cycle at the weld toe and thus induced strain ratcheting at the toe of the welded joint. The axial strain response in Fig. 2.6 also demonstrates that the ratcheting rates (strain accumulation per cycle) gradually decrease during the first 250 cycles and then continues at a constant rate up to about 600 cycles when the rate of ratcheting gradually accelerates and initiates a fatigue crack at 800 cycles (strain gage failed around 700 cycles). In the subsequent cycles, the crack propagates to become a through-wall crack at 980 cycles. This response is typical of ratcheting response of SS 304 [Hassan and Kyriakides, 1994a]. It is also interesting to note in Fig. 2.4 that the circumferential strain is also ratcheting in the tensile direction with a small rate. The occurrence of circumferential strain ratcheting in the tensile direction

also indicates the presence of tensile circumferential residual stress. The hypothesis of strain ratcheting near the weld toe is also validated by the axial strain response from the top mid-pipe length strain gage as shown in Fig. 2.8. No ratcheting is observed at this location; the strain response is almost symmetric, as no or very small residual stresses are present at this location. The gradual decrease in strain amplitude at his location might be related to the cyclic softening of the load response shown in Fig. 2.5.

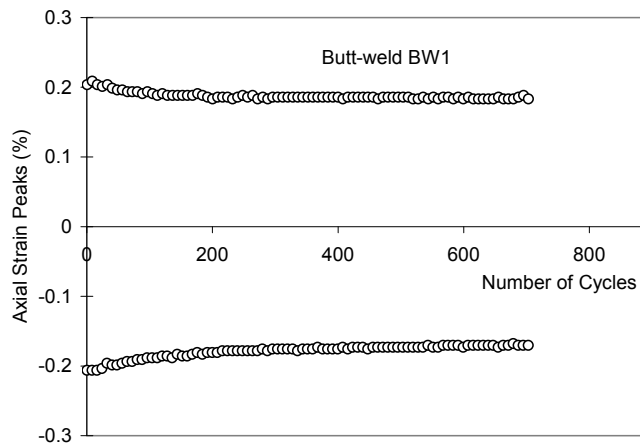


Fig. 2.8. Axial strain peaks (every 10th cycle) at the mid-length pipe top.

This biaxial ratcheting phenomenon under multiaxial loading cycle is a complex phenomenon as can be realized from analyzing the experimental ratcheting responses developed by Hassan and Kyriakides [1994a, see Figs. 10-13 in the reference]. In these experiments, they prescribed the same stress-controlled axial cycle to straight pipe specimens (material test specimen) under the presence of various levels of internal pressure. When the internal pressure was zero, axial strain ratcheting was observed in the tensile direction due to the tensile mean stress of the stress cycle. The circumferential strain ratcheting, on the other hand, occurred in the compression direction due to the Poisson's effect (see Fig. 10 in Hassan and Kyriakides [1994a]). As the internal pressure is prescribed, it induces circumferential strain ratcheting in tensile direction, which in effect reduced the rate of axial strain

ratcheting because of the Poisson's effect. As the pressure level is gradually increased, the axial strain eventually changed its ratcheting direction towards compression when considerable circumferential strain ratcheting occurred in the tensile direction. Comparison of these material test strain ratcheting responses with the butt-weld toe strain responses (Fig. 2.4) supports the conclusion that residual stresses are the driving force in inducing ratcheting at the weld toe. However the exact mechanism of the influence of residual stress is not known or understood well.

Similar to the top toe, strains at the bottom toe also demonstrates ratcheting as shown in Fig. 2.9, where the amplitude and mean of the axial strain responses, at every 10th cycle, at the top and bottom toes are plotted. Comparison of these responses demonstrates that the axial strain values at the top toe are always larger than those at the bottom, which might be a reason for the fatigue crack initiation at the top toe. However, the axial strain amplitude at the top toe is also larger than at the bottom toe (Fig. 2.8). Hence it is not known if the strain amplitude or the strain ratcheting is more influential in initiating fatigue cracks at the welded joints.

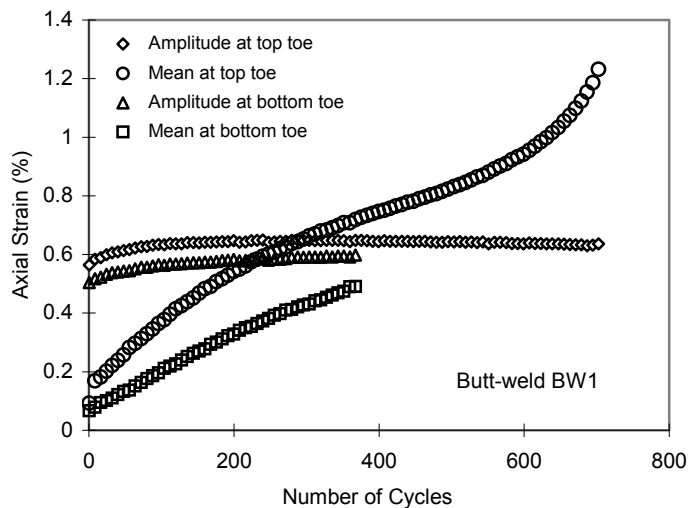


Fig. 2.9. Amplitude and mean of axial strain cycles (every 10th cycle) at top and bottom toes.

Socket-Weld Specimen SW1

A socket weld specimen is shown in Fig. 2.2 and a sketch of the specimen showing the locations of strain gages is shown in Fig. 2.3. The SW1 weld joint was fabricated through four tack welds and three weld-passes (see the inset in Table 2.1) using the quarter-circumferential welding sequence. The fatigue test of the socket-weld was performed using the cantilever setup (Fig. 2.1) and by prescribing a displacement-controlled saw-tooth cycle of amplitude 14.5 mm (0.57 inches). The load-displacement and strain responses of socket weld specimen SW1 are very similar to those obtained from the butt-weld specimen BW1 test and hence are not shown here. The fatigue crack in this test was first noticed after 420 cycles at the bottom toe of the socket weld along the circumferential direction. Then crack at the top-toe was manually detected around 500 cycles. The bottom-toe crack propagated through the thickness after about 680 cycles.

Comparison of axial strain amplitudes and means at the top and bottom welds for the socket weld (SW1) and butt weld (BW1) are shown in Figs. 2.10 and 2.11. It is shown in these figures that for the socket weld, the axial strain amplitude and mean values at the bottom toe are greater than those at the top toe. This may be the reason that the crack initiated at the bottom toe first, whereas for butt-weld the result is reversed (Fig. 2.9). It is also shown that the amplitude and mean values of axial strains in the socket-weld are larger than that in the butt weld as expected due to the higher stress concentration at socket-weld compare to that at butt-weld. The higher strain amplitude and mean values in the socket-weld leads to the shorter fatigue life (680 cycles) compare to the butt-weld life (980 cycles).

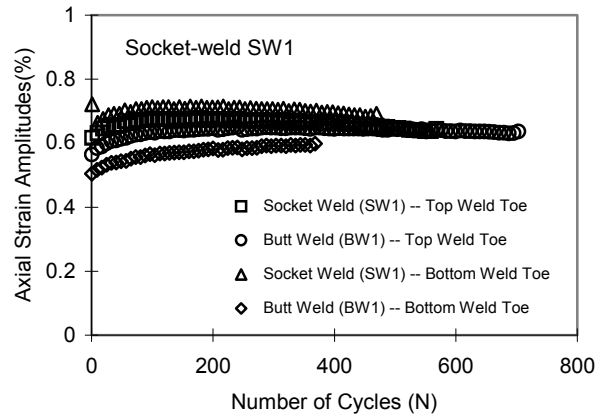


Fig. 2.10. Axial strain amplitudes from the butt and socket weld tests

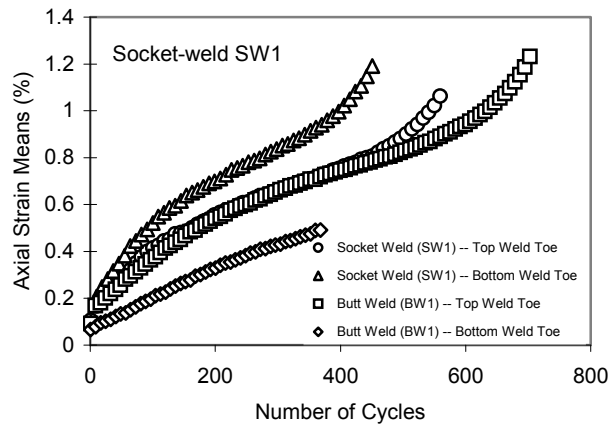


Fig. 2.11. Axial strain means from the butt and socket weld tests

Socket-Weld Specimens SW2 and SW3

Two more socket weld tests were performed with the cantilever setup and prescribing a displacement-controlled saw-tooth cycle of amplitude 14.5 mm (0.57 inches). The socket-weld specimen SW2 was fabricated using tack welds and quarter-circumferential welding sequence, similar to specimen SW1 but this specimen had four weld passes (see Table 2.1). The fatigue crack in this test was first noticed after 560 cycles at the bottom toe of the socket weld along the circumferential direction. This crack propagated through the thickness at the bottom toe after about 900 cycles as

detected by the leakage of pressurized oil. The load-displacement and strain responses in this test are similar to that observed in specimen SW1.

The socket-weld specimen SW3 was fabricated using four full-circumferential weld passes as shown in the inset in Table 2.1. The tack welding was performed as in other cases before the weld bead sequences. Because of the full-circumferential welding, the pipe of the specimen distorted about 5° (0.96 inch drift was measured at the pipe end with respect to the socket) with respect to the socket axis. The fatigue crack in this test was first noticed after 300 cycles at the top toe of the socket weld along the circumferential direction. This crack propagated through the thickness after about 470 cycles. The strain responses again demonstrate the occurrence of ratcheting in a similar manner as in the earlier butt and socket weld tests.

The fatigue lives from the four welded joint tests are summarized in Table 2.1 and the amplitude and mean axial strain responses at fatigue crack locations from the four tests are summarized in Figs. 2.12 and 2.13. Comparison of fatigue lives in Table 2.1 demonstrates the influence of weld bead sequence on the fatigue life of socket welded joints. The socket-weld with four weld passes (SW2) has a higher fatigue life than that with three weld passes (SW1). Weld joint fabricated with quarter circumferential weld sequence (SW2) yields higher fatigue life compare to that with full circumferential weld sequence (SW3). It is observed in Figs. 2.12 and 2.13 that the axial strain amplitudes and ratcheting rates in the sequence of lowest to the highest value is obtained in the order of BW1, SW2, SW1 and SW3. On the other hand from Table 2.1, it is observed that the highest to lowest fatigue life sequence is obtained in the order of BW1, SW2, SW1 and SW3. So, it can be concluded that both the higher axial strain amplitude and ratcheting strain leads to shorter fatigue life. However, the question remains how the strain responses at the weld are affected by the strain zero-shift of the gages. In order to understand the influence of weld toe strain response on the fatigue crack initiation, an investigation on the strain gage zero-shift is conducted as discussed below.

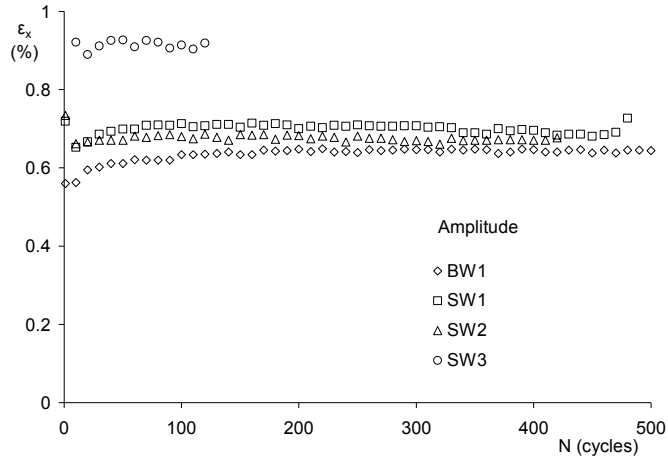


Fig. 2.12. Axial strain amplitudes at fatigue crack locations from the four butt- and socket-weld tests.

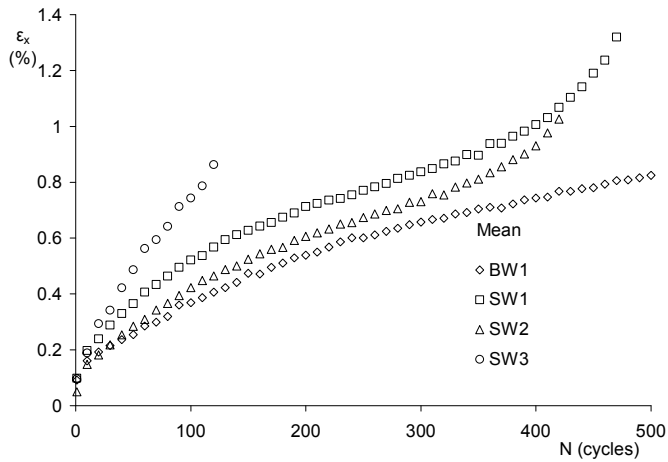


Fig. 2.13. Axial strain means at fatigue crack locations from the four butt- and socket-weld tests.

Strain Gage Zero-Shift

The type of strain gages used in the study is CEA manufactured by MicroMeasurment. It is stated in the manufacturer manual that for this gage there would be a strain zero-shift for cyclic strain amplitudes above 0.15%. This information was realized after all the weld experiments were completed. Hence, in order to determine the magnitude of errors in the recorded strain responses an experimental study was conducted. A set of uniaxial strain-controlled experiments on dog-bone

coupons was conducted. Both the extensometer and the strain gage data were recorded simultaneously during the tests.

A trial experiment in the setup shown in Fig. 2.14a was conducted first. Three CEA-series strain gages were installed on outer surface of a tubular specimen. The specimen was prescribed with strain-controlled load at the amplitudes of 0.2%, 0.4%, 0.6%, and 0.8% sequentially for a total of 80 cycles as shown in Fig. 2.14b. The experimental results showed that strain data from extensometer and strain gages were very close during the first two amplitudes, 0.2% and 0.4%. Zero-shift phenomena of strain gage were observed after the third amplitude. The test results illustrated that zero-shift error occurred when strain amplitude of strain gage is larger than 0.4%. Another observation from the experiment is that as the strain responses from all three strain gages were very similar, the coupon can be assumed homogeneous. Therefore, the difference of strain responses on extensometer and strain gages is zero-shift error rather than local strain difference, although the gage lengths of extensometer and strain gages are different.

Four more zero-shift experiments were conducted to understand the relationship of strain amplitude and zero-shift error. This relationship will be used to correct strain mean data that were obtained from fatigue tests on welded piping joints. The zero-shift experiments were conducted on four specimens by prescribing different strain amplitudes, which are 0.4%, 0.6%, 0.7%, and 0.95%. The cyclic tests on these four specimens were stopped when the strain amplitude of strain gage did not match that of extensometer. Experimental axial strain means from each cycle are calculated using:

$$Mean = \frac{\varepsilon_{max} + \varepsilon_{min}}{2},$$
 and the valid data are plotted against the number of cycles in Fig. 2.15a. The

experimental data in Fig. 2.15a demonstrated that zero-shift error is mainly linear correlated to number of cycles, so linear fits of strain mean were determined to represent zero-shift rates. The zero-

shift rates against strain amplitudes were plotted in Fig. 2.15b, which also includes a quadratic fit of the zero-shift rates.

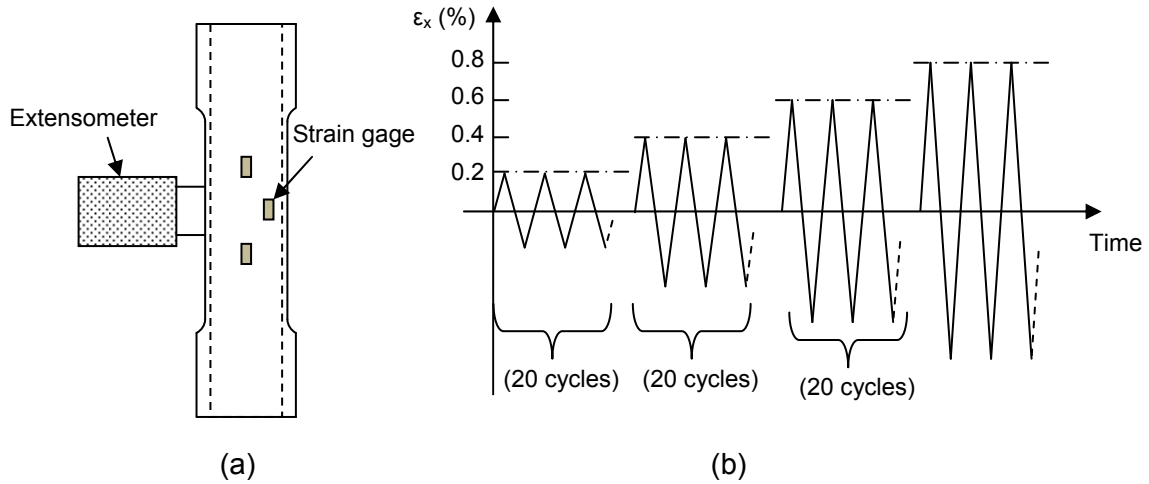


Fig. 2.14. Trial experiment for strain gage zero-shift. (a) Setup of extensometer and strain gages on tubular specimen. (b) Strain-controlled load history.

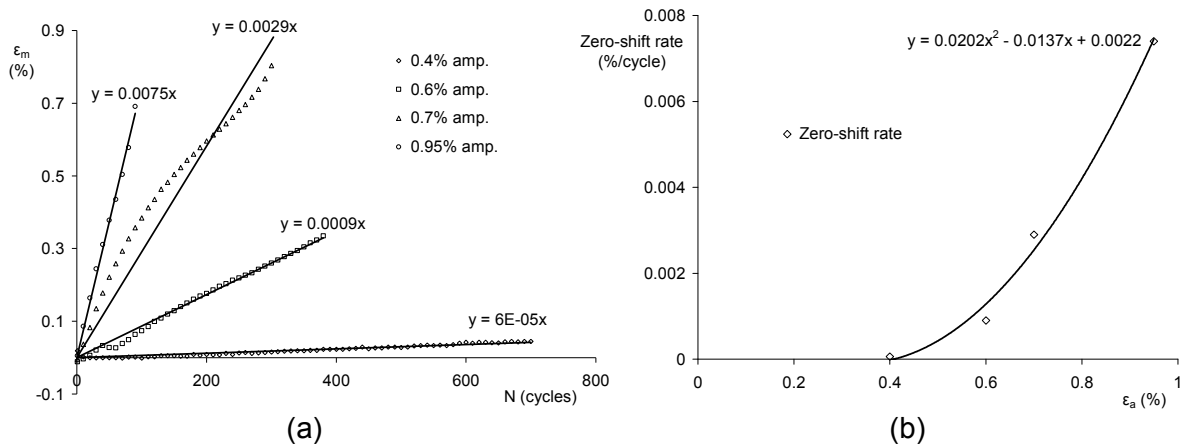


Fig. 2.15. (a) The relationship of strain gage zero-shift and cycle numbers under various strain amplitudes. (b) Zero-shift rates against strain amplitudes and a quadratic fit.

The concept of correcting strain mean data of previous fatigue loading tests on welded piping joints is that the strain mean value obtained from gage is the combination of correct strain mean and zero-shift error. Thus, the correct strain mean can be calculated by the following Eq. (2.1):

$$\epsilon_{correct}^{mean} = \epsilon_{strain-gage}^{mean} - \epsilon_{zero-shift}^{mean} \quad (2.1)$$

The zero-shift error, $\epsilon_{zero-shift}^{mean}$ in Eq. (2.1), is determined from the quadratic function in Fig. 2.15b as a function of strain amplitude. The correction of strain mean is made on each cycle using the Eq. (2.1) when the strain amplitude of the cycle is larger than 0.4%. If the strain amplitude in a cycle is not larger than 0.4%, the strain mean of the cycle would not be modified.

The strain means in Fig. 2.13 were corrected with zero-shift error and the data after the correction are plotted in Fig. 2.16. The corrected ratcheting trends for all the welded joints are similar that ratcheting rates are positive, then negative, and finally going positive again as loading cycles process. The ratcheting rates of all welded joints are closed during the first 50 cycles. The corrected ratcheting data in Fig. 2.16 seem do not have much relationship with their fatigue lives.

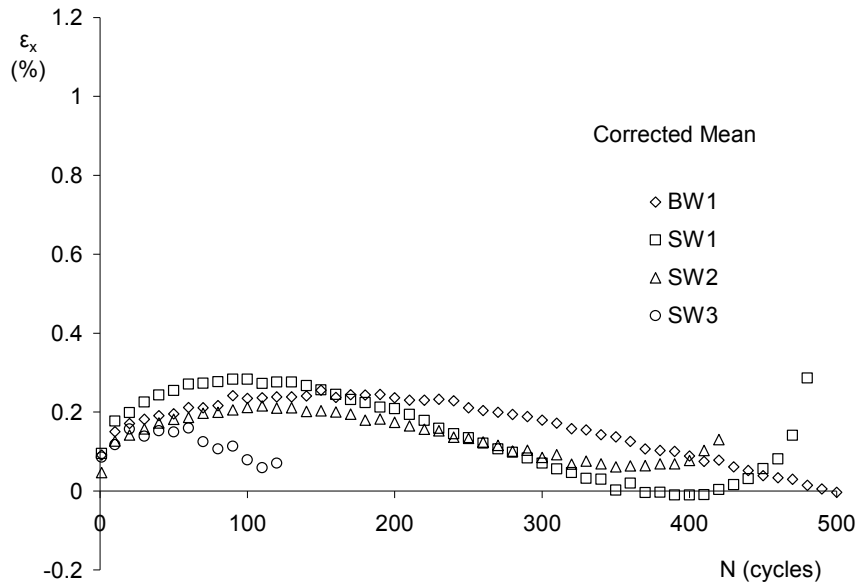


Fig. 2.16. Zero-shift error corrected axial strain means at fatigue crack locations from the four butt- and socket-weld tests.

SIMULATION

Numerical schemes with FE program ANSYS and ABAQUS were developed to simulate welding process, and hence the residual stress and subsequent fatigue responses of welded joints. In welding process simulation, sequentially uncoupled, nonlinear, transient, thermo-mechanical analyses were employed to calculate temperature history and initial residual stresses. Finally, the fatigue responses of welded joints with the initial residual stress fields were simulated by prescribing displacement-controlled cyclic loading. Detailed simulation techniques and simulation results are presented below.

Thermal Analysis of Welding Process

In the thermal finite element analysis, the boundary condition assigned to the model is material surface. Heat loss occurs from the material surface through both convection and radiation, which are related to film coefficient and radiation constant, respectively. In the simulation, the material surface is not fixed through the whole welding process. Some part of the material surface has to be removed or added as the welding arc advances. The temperature-dependent material properties assigned for thermal simulation, obtained from Li [1995], Brickstad and Josefsen [1998], are listed in Table 2.2.

In thermal simulation the applied heat source is heat flow Q , which was calculated by the following function [Radaj, 1992]:

$$Q = \eta UI$$

where, η = arc coefficient (between 0 and 1)

U = arc voltage (Volt)

I = arc current (Amp)

The value of arc coefficient (η) is dependent mostly on the welding environment, and could be different from one welding case to the other. Heat flow Q is then divided into heat contents Q_s and Q_b for surface heat flux and body heat flux, respectively. In ANSYS and ABAQUS the heat loads applied are q_s (surface heat flux) and q_b (body heat flux), which can be expressed by,

$$q_s = Q_s / S$$

$$q_b = Q_b / V$$

where, S is the surface area, and V is the volume.

Table 2.2. Temperature-dependent thermal and mechanical material properties of SS304 [data from Li, 1995, Brickstad and Josefsen, 1998]

Temperature (K)	Specific heat (J kg ⁻¹ , °K)	Conductivity (W m ⁻¹ , °K)	Enthalpy (J m ⁻³)	Film coefficient (W m ⁻² °K)
0	465.40	8.12	0.00E+08	1.00
100	478.76	9.73	3.78E+08	1.00
200	492.12	11.35	7.66E+08	1.00
300	505.48	12.97	1.17E+09	1.80
400	518.84	14.59	1.57E+09	8.48
500	532.20	16.21	2.00E+09	15.16
600	545.56	17.82	2.43E+09	21.84
700	558.92	19.44	2.87E+09	28.52
800	572.28	21.06	3.32E+09	35.20
900	585.64	22.68	3.78E+09	62.74
1000	599.00	24.30	4.26E+09	85.84
1100	612.36	25.91	4.74E+09	108.94
1200	625.72	27.53	5.24E+09	132.04
1300	639.08	29.15	5.74E+09	155.14
1400	652.44	30.77	6.26E+09	178.24
1500	665.80	32.39	6.79E+09	201.34
1600	679.16	34.00	7.33E+09	224.44
1613	688.91	35.19	7.72E+09	241.30
1663	688.91	35.19	9.84E+09	241.32
1723	788.00	41.36	1.01E+10	252.85
3100	788.00	211.11	1.88E+10	570.94

In the thermal finite element analysis, in order to simulate the multi-pass welding process, one needs to model the addition of filler material as new weld passes are deposited and the geometry of the welded joint is built-up. This is done through the element birth/death technique in ANSYS and ABAQUS. The steps of using this technique are depicted in Fig. 2.17 for a butt-welded plate. With this technique, a finite element mesh of the welded joint including the weld beads is generated first. Subsequently, the element groups representing each weld pass are deactivated (element death) before

welding is included in the analysis. These elements are reactivated (element birth) sequentially as the welding arc (heat source) advances along the circumferential direction.

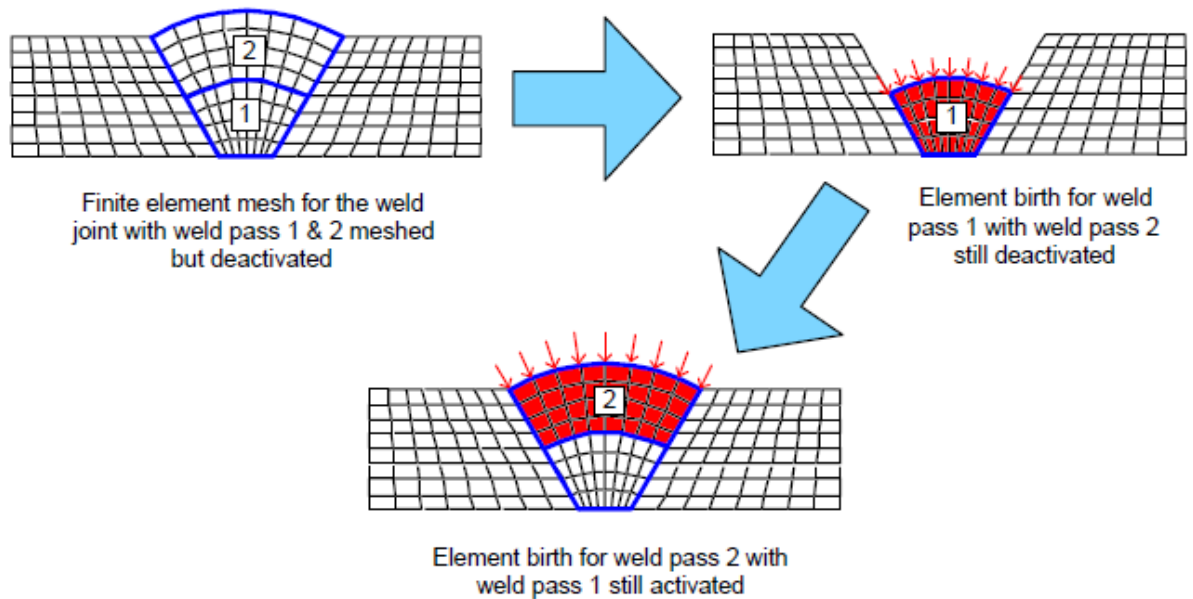


Fig. 2.17. An example of element birth and death.

The thermal analysis was first validated by performing a 2D finite element analysis for a two-pass butt-welded stainless steel plate joint as shown in Fig. 2.18, and a 3D girth-welded stainless steel pipe, shown in Fig. 2.20. In the 2D plate simulation thermal element PLANE55 was used in the modeling. The numerical results of temperature history during the 1st welding pass and the corresponding experimental data from Murugan et al. [1999] are compared in Fig. 2.19. This figure shows that the temperature history at mid-thickness points at distances of 11.5 mm, 16.5 mm, 21.5 mm and 26.5 mm from weld edge at the bottom (see Fig. 2.18) are simulated quite well.

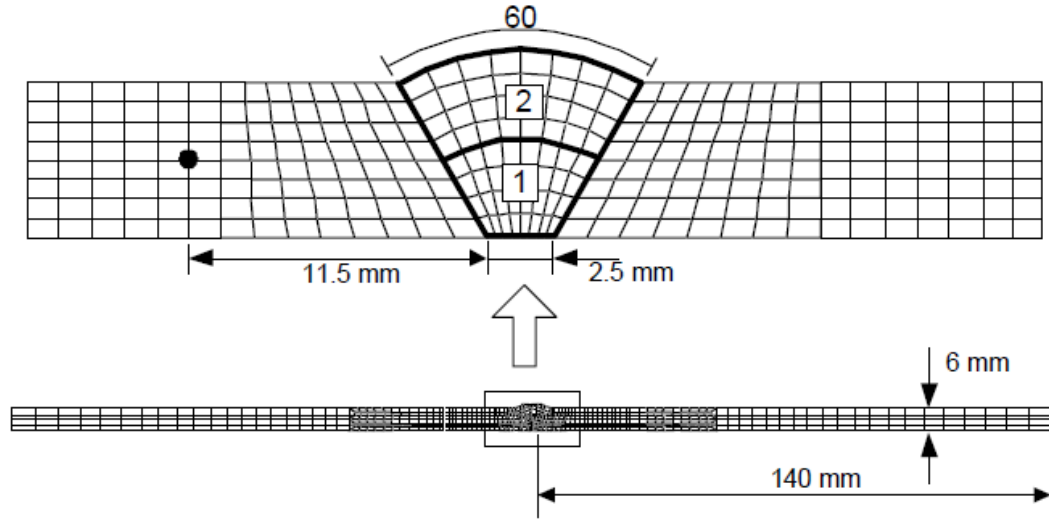


Fig. 2.18. The 2D finite element model for a two-pass butt-welded plate joint.

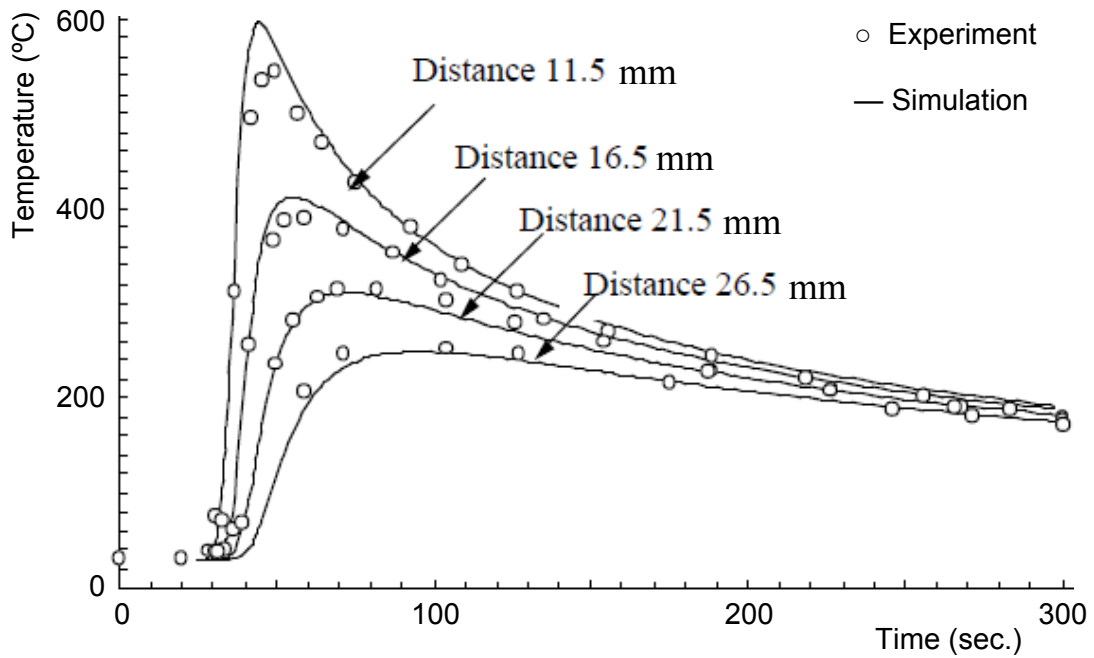


Fig. 2.19. Calculated temperature history during the 1st welding pass in comparison with the experimental data from Murugan et al. [1999]

The thermal analysis of the 3D girth-welded stainless steel pipe, shown in Fig. 2.20, was conducted using ANSYS and ABAQUS. The weld was completed in four continuous welding passes

with one start-stop position. The analysis assumes that symmetry exists about the centerline of the weld bead, so only half of the weld bead is modeled. Eight-noded 3D thermal solid elements SOLID70 were used for the thermal analysis. In Fig. 2.21, a comparison between the calculated and experimentally measured temperature histories during all four welding passes (from Li [1995]) at location 6.35 mm from weld centerline on the inner surface (see inset in the figure) is shown. As seen in this figure, the correlation between the experimental and finite element results from both ANSYS and ABAQUS is quite satisfactory.

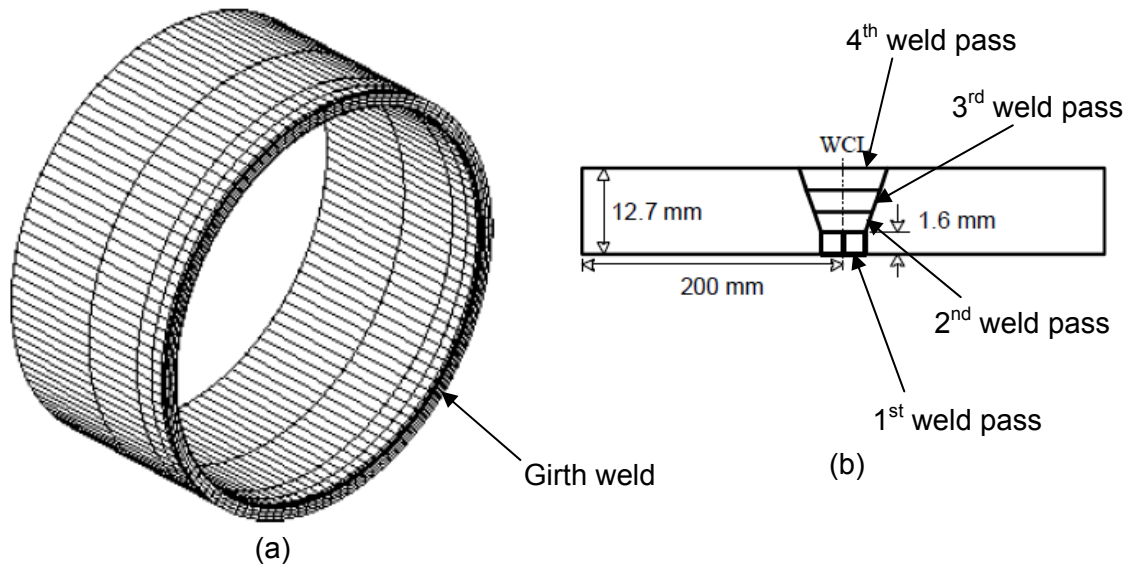


Fig. 2.20. (a) The 3D finite element model for four-pass girth-welded pipe; only half of the pipe is simulated (b) the cross section of groove geometry and weld pass sequence

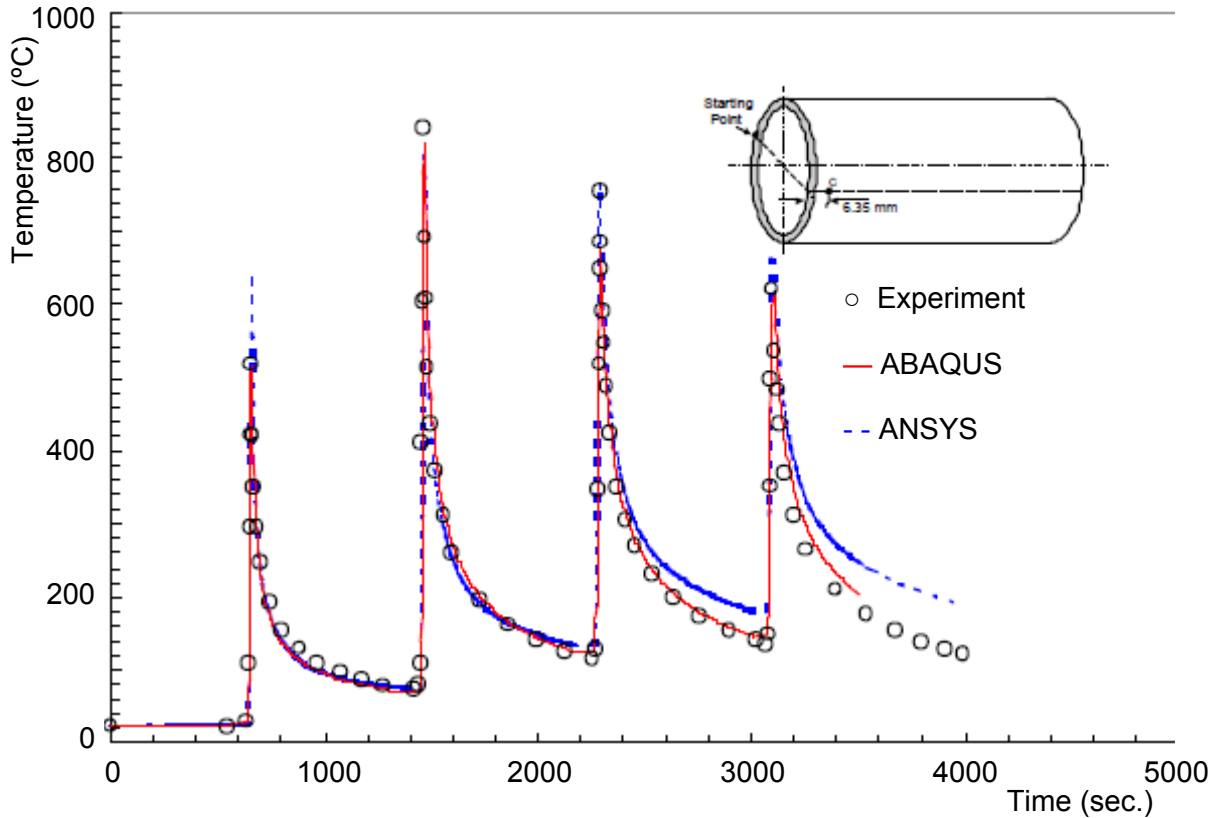


Fig. 2.21. Comparison of temperature history between numerical and experimental results; experimental data from Li [1995]

Residual Stress Simulation of welded Joints

The residual stress analysis was conducted and validated against the data from the literature on butt-welded stainless steel pipe as shown in Fig. 2.20, before performing the analysis of socket welded piping joints. For residual stress calculation, the time-dependent temperature field determined from the thermal analysis was prescribed as input. Hence, the node labels of the structural mesh must match to those of the thermal analysis mesh. To satisfy this requirement in ANSYS, the finite element model for residual stress analysis was established from the thermal model by issuing the command ETCHG to change element types. Similar to the thermal analysis, element birth/death was also used in the residual stress analysis.

The temperature-dependent parameters which were used in the residual stress simulation are listed in Table 2.3. The bilinear kinematic hardening model was employed and the model parameters were obtained through the fit shown in Fig. 2.22. The temperature dependent material data used for the bilinear fit were obtained from Kang et al. [2005] and Brickstad and Josefsen [1998]. Note that there is no material data available for the temperature range 700-1400°C, for which linear interpolation method was used to obtain model parameters.

Table 2.3. Temperature-dependent mechanical material data of SS304 [data from Kang et al., 2005, and Brickstad and Josefsen, 1998]

Temperature (°C)	Poisson's ratio	Yield stress (MPa)	Thermal expansion (1/°C)	Elastic Modulus (GPa)	Tangent Modulus (GPa)
25	0.28	338	19E-06	238.03	5.13
200	0.29	200	19E-06	210.53	2.21
400	0.30	144	19E-06	197.26	3.34
600	0.31	120	19E-06	179.10	4.07
700	0.32	90	19E-06	120.00	3.78
1400	0.36	10	19E-06	10.00	0.00

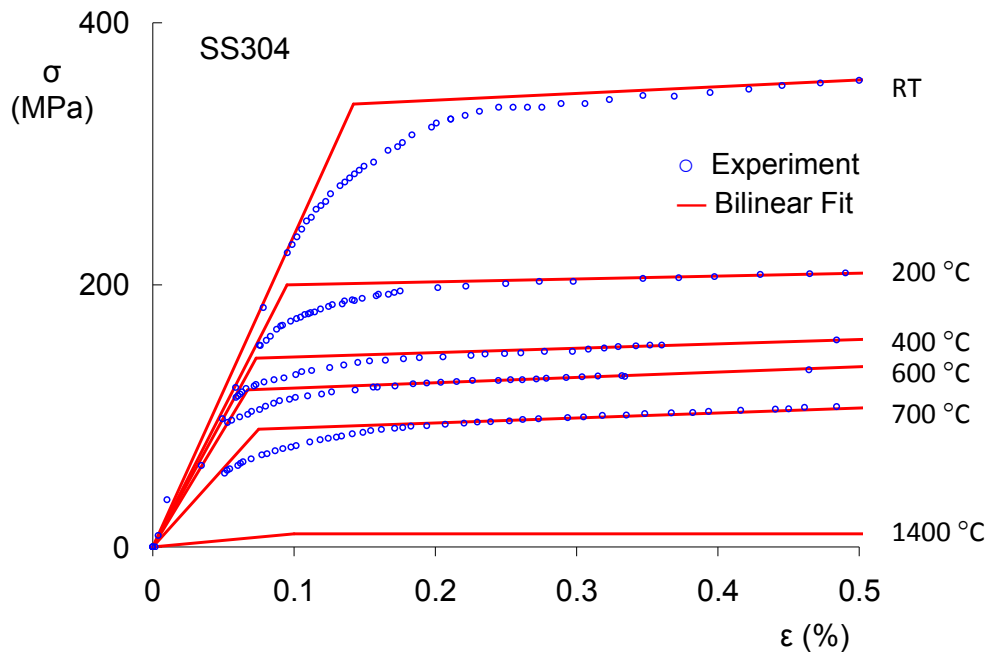


Fig. 2.22. Temperature-dependent stress-strain experimental responses and corresponding bilinear fit

The butt-welded piping joint in Fig. 2.20 is modeled using SOLID45 (corresponding structural element to the thermal element SOLID70). The axial and circumferential residual stress distributions for the butt-weld joint on the outer and inner surface of the pipe as a function of distance from weld centerline is shown in Fig. 2.23. The residual stresses shown in this figure are at a location 180° away from the welding start/stop point. In Fig. 2.23, it is observed that the finite element results from ANSYS and ABAQUS generally agree with the measured residual stresses, except for the circumferential residual stress at the inner surface. The reason for this discrepancy could not be identified.

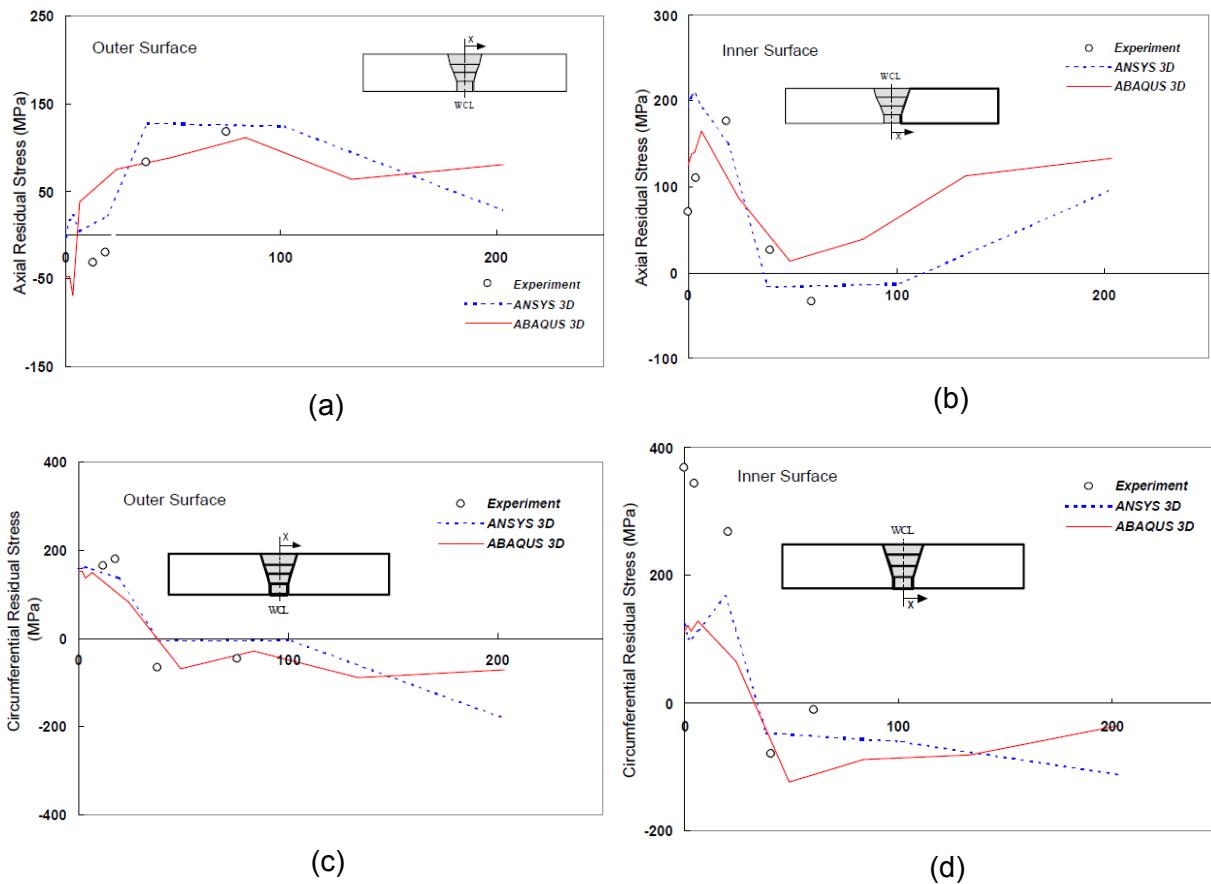


Fig. 2.23. Measured and simulated residual stress distributions. (a) Axial residual stress at the outer surface, (b) axial residual stress at the inner surface, (c) circumferential residual stress at the outer surface, and (d) circumferential residual stress at the inner surface.

Residual Stress Analysis for Socket Welded Joints

The thermal and residual stress analyses for the three-pass socket-welded piping joint were performed following the validation of the analysis tools. A 3D finite element model was created using ANSYS, as shown in Fig. 2.24. Eight-noded 3D heat transfer elements SOLID70 were employed for thermal analysis. Meshing of the model was developed carefully with finer elements near welding. The model of the socket welded joint was composed of the pipe, socket, flange, stiff loading head, stiff support. Displacement-controlled cyclic loading was prescribed at the end of the stiff head for fatigue response simulation. The stiff support represents the metal table on which flanged socket was resting during welding to represent the heat transfer more accurately, and represents the stiff support column during fatigue tests (see Fig. 2.1). The heat absorption by the metal table during welding influenced the cooling rate of the piping joint, hence was essential to include stiff support. The progressive weld bead deposition during first weld pass from start is demonstrated in Fig. 2.25.

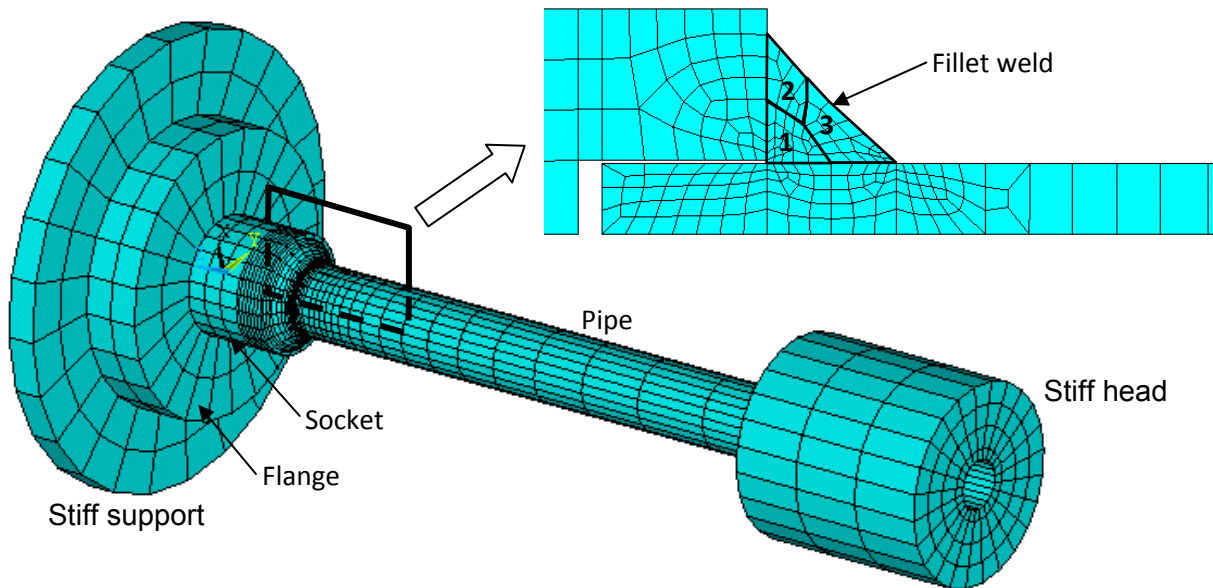


Fig. 2.24. Finite element model of three-pass socket-welded stainless steel pipe joints

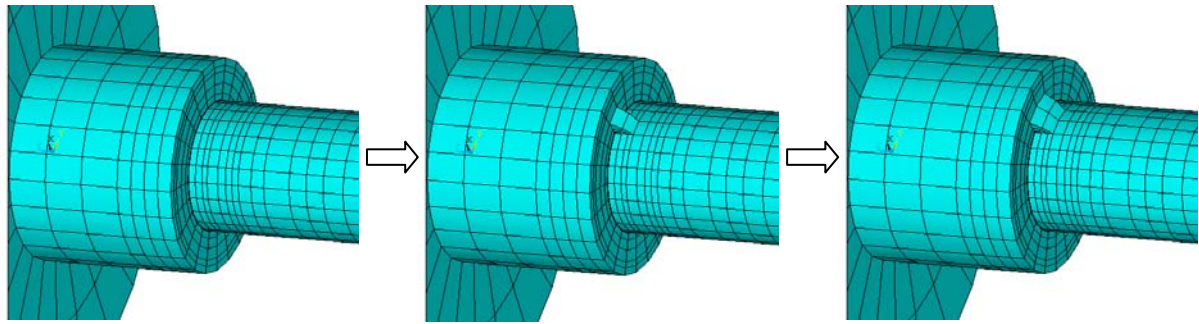


Fig. 2.25. Illustrations of finite element modeling of the progressive welding bead deposition during the first weld pass

Using a similar numerical technique as described above for the butt-welded pipe, 3D finite element thermal and residual stress analyses for a three-pass socket-welded joint (Fig. 2.24) was performed using ANSYS. Solid elements SOLID185 instead of the SOLID 45 used earlier in the butt-weld simulation were used for finite element mesh generation, as the latter element yielded convergence problem. In addition, 3D point-to-point contact elements CONTACT52 were added to the model to simulate the contact between the outer surface of the pipe and the inner surface of the socket during welding and fatigue loading as shown in Fig. 2.26.

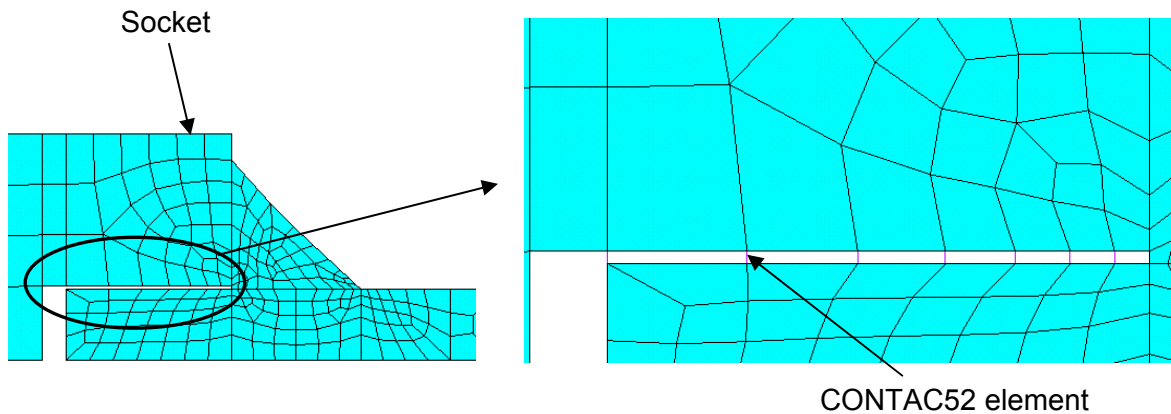


Fig. 2.26. Contact elements CONTACT52 added to the model between the outer surface of the pipe and the inner surface of socket during welding and fatigue loading

An example of the thermal analysis results for socket-welded joints moving temperature field during the last quarter of the last welding pass is demonstrated in Fig. 2.27. In this figure, we see that the high temperature field moves with the welding arc.

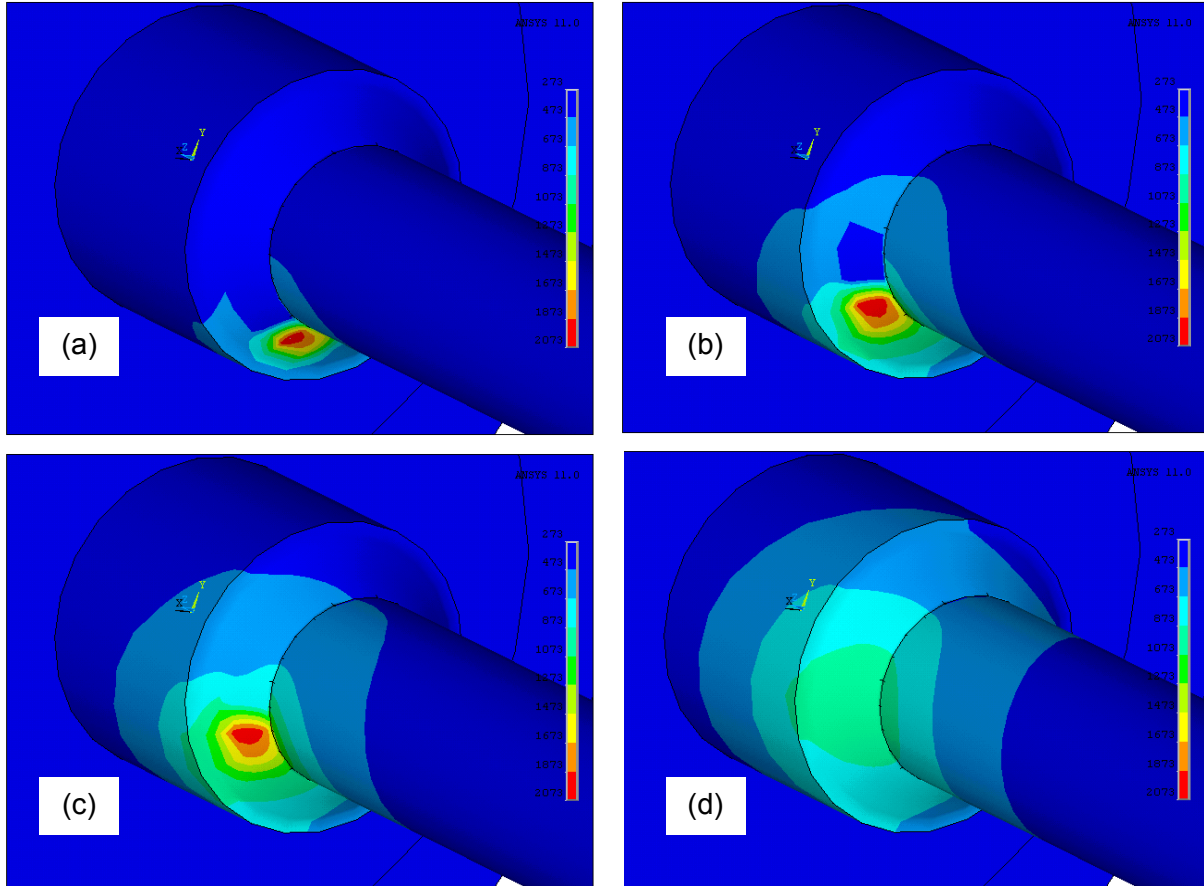


Fig. 2.27. Illustration of moving temperature (in Kelvin) field during the final quarter welding (a, b, and c) and cooling (d) of the last welding pass.

The axial residual stress distribution on pipe outer surface near weld toe is plotted in Fig. 2.28. In this figure, angles 0° , 90° , 180° , and 270° represents the tack weld and welding start/stop locations A, B, C, and D, as shown in Fig. 2.30. It is observed in Fig. 2.28 that the residual stresses are maximum tensile or compressive near weld toe and decreases to zero within the 40 mm from the toe. Axial residual stress at or near the weld toe are compressive between 0° and 90° and between 180° and 315° , which are the top and bottom sides of the specimen during fatigue testing. The maximum

compressive axial stress, located at top weld toe, at the middle of A and B, is about -450 MPa, which is higher than the yield stress of stainless steel base metal (350 MPa). The circumferential residual stress distribution on pipe outer surface near weld toe is plotted in Fig. 2.29. The maximum compressive circumferential residual stress, located at top weld toe, at the middle of A and B, is about -300 MPa.

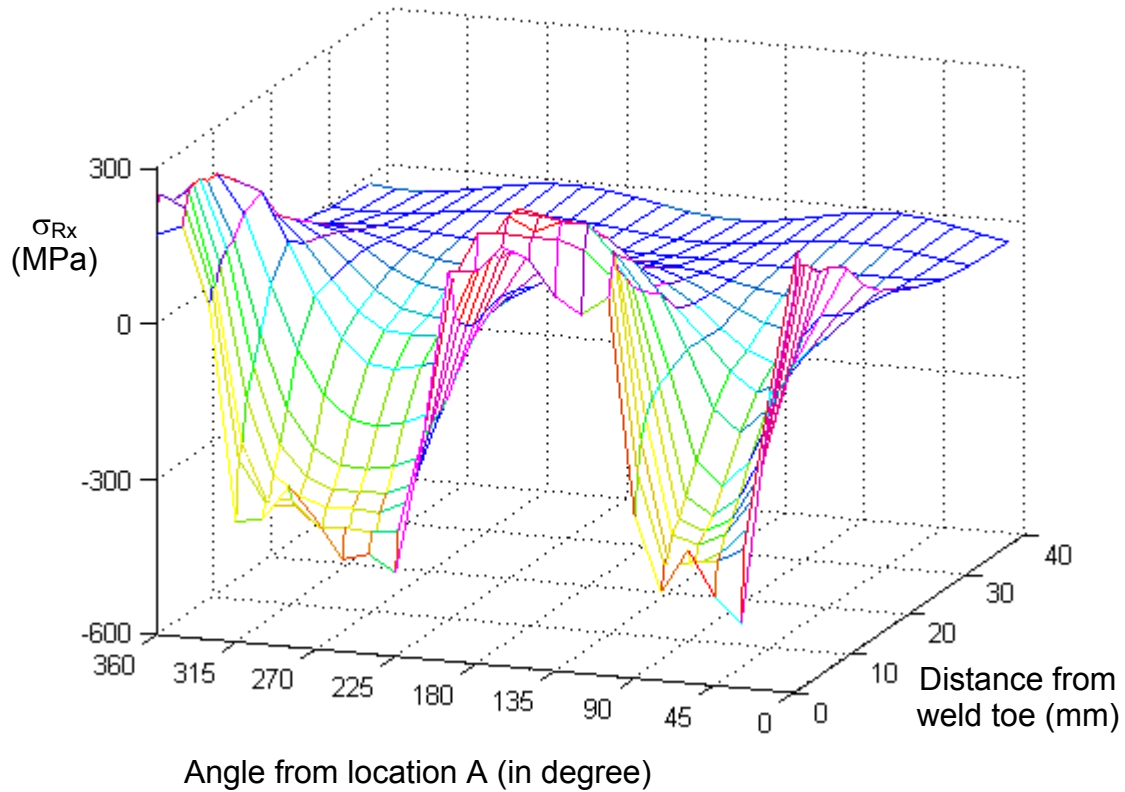


Fig. 2.28. Axial residual stress distribution on pipe outer surface; Angle is measured from location A which is the location of the first tack weld as shown in Fig. 2.30.

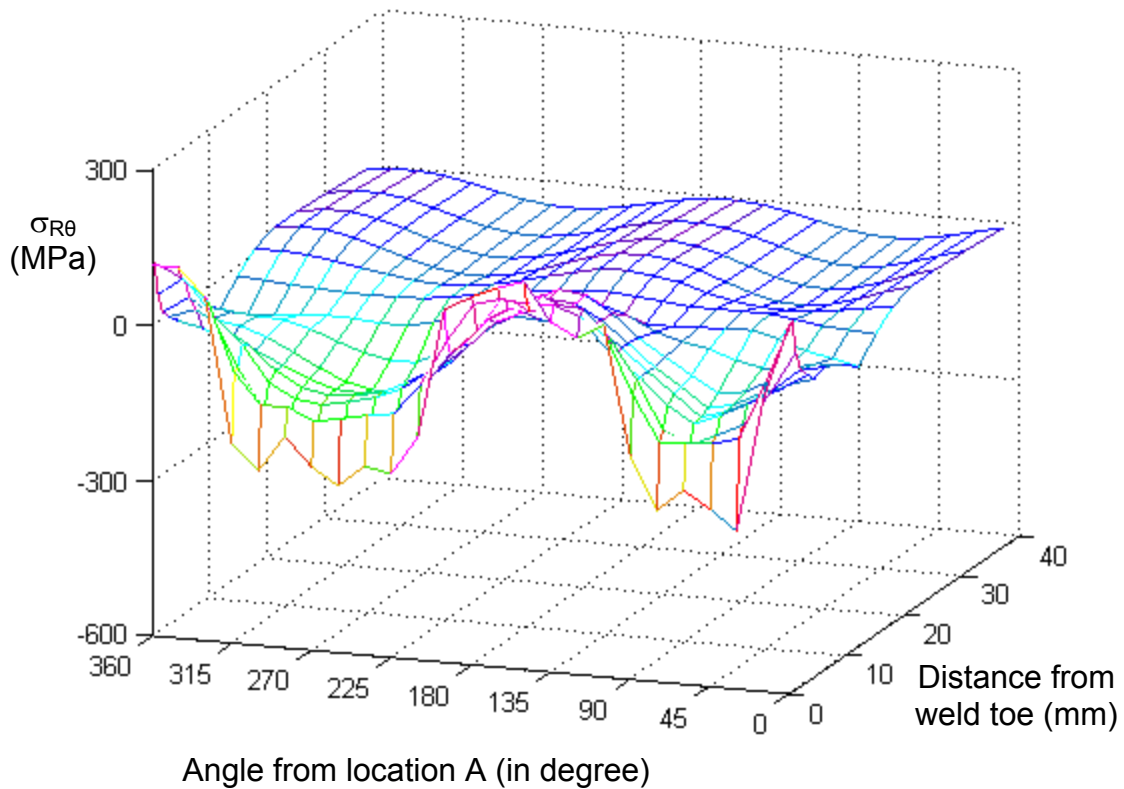


Fig. 2.29. Circumferential residual stress distribution on pipe outer surface; Angle is measured from location A which is the location of the first tack weld as shown in Fig. 2.30.

Fatigue Response Simulation for Socket-Welded Joints

Quasi-static fatigue response simulation for the socket-welded piping joint under displacement-controlled cyclic loading is performed in the presence of the initial residual stress field computed above. The finite element mesh adopted is the same as in the residual stress analysis with solid elements SOLID185 and contact element CONTACT52 as shown in Fig. 2.26. Base metal material properties at room temperature using the bilinear kinematic hardening model fit was used in the fatigue response simulation. Displacement-controlled cyclic loading with amplitude of 14.5 mm was applied at the head end of the model as shown in Fig. 2.30.

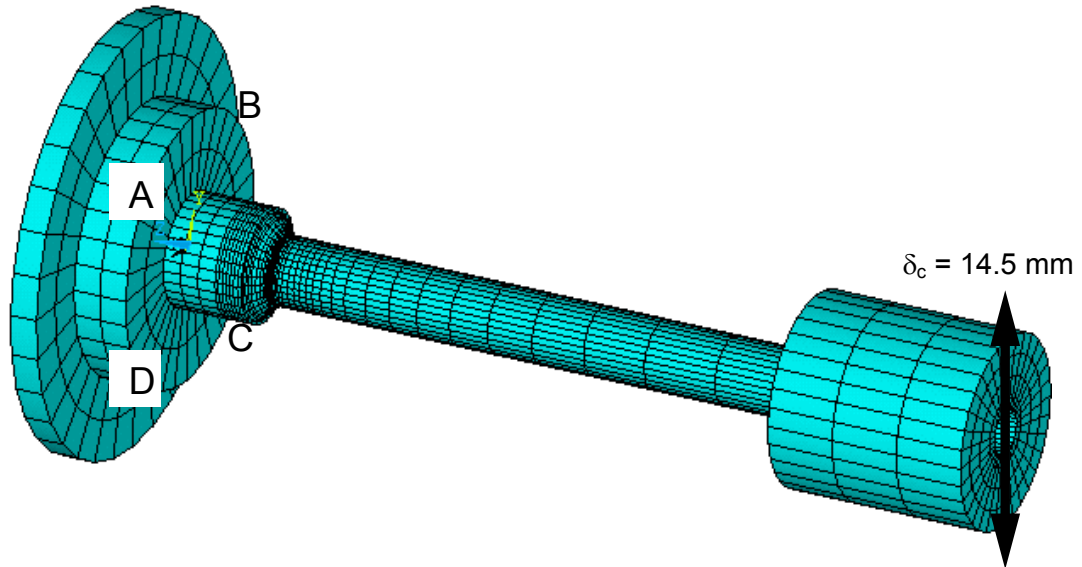


Fig. 2.30. Finite element model for fatigue simulation under displacement-controlled loading.

Comparison between the finite element computed and experimentally measured force-displacement responses for the first five loading cycles are shown in Fig. 2.31. The simulated force peaks matched the experimental peaks well, but the simulated hysteresis curves do not compare well to the experimental hysteresis curves. The force amplitude and mean as a function of the number of cycles from experiment and simulation compares well as shown in Fig. 2.32. The axial strain amplitude and mean responses at top of the pipe, 5mm away from weld toe, from experiment and simulation are plotted against number of cycles in Fig. 2.33. Since the simulated results of force and axial strain response do not change after 10 cycles, only 20 cycle responses are shown in Figs. 2.32 and 2.33. The experimental force response show cyclic hardening in the first five cycles and then gradually softened; The simulation does not show any hardening or softening, because stable material properties with the bilinear kinematic hardening model was used. Fig. 2.33 demonstrated significant overprediction of strain amplitudes and shakedown of the axial strain mean responses. This drawback in simulating the strain responses could be attributed to the bilinear model, which demonstrated earlier by Rahman et al. [2008] and Bari and Hassan [2000]. Other material models like Chaboche or

Ohno model [Chaboche, 1991, Abdel-Karim and Ohno, 2000] may improve the strain response simulation. Another reason for the erroneous prediction of strain response could be the use of base metal material properties in the simulation. During welding the heat affected zone (HAZ) metals experienced high temperature cycles, which may change the material properties of the HAZ metals.

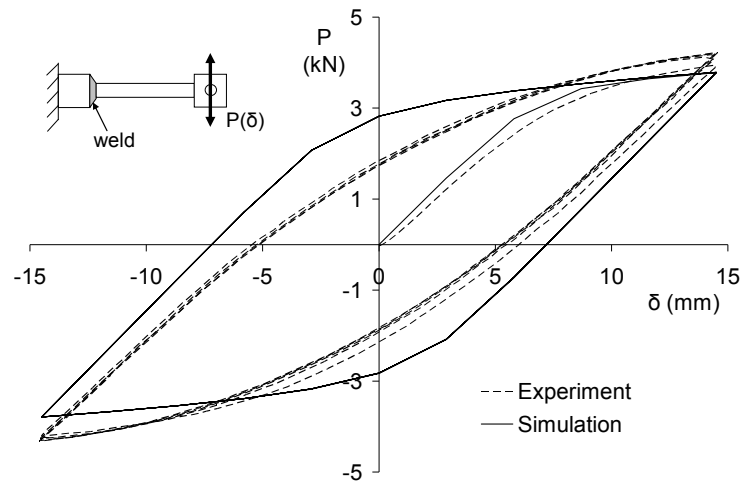


Fig. 2.31. A comparison of first 5 cycles of force-displacement hysteresis curve from experiment and simulation

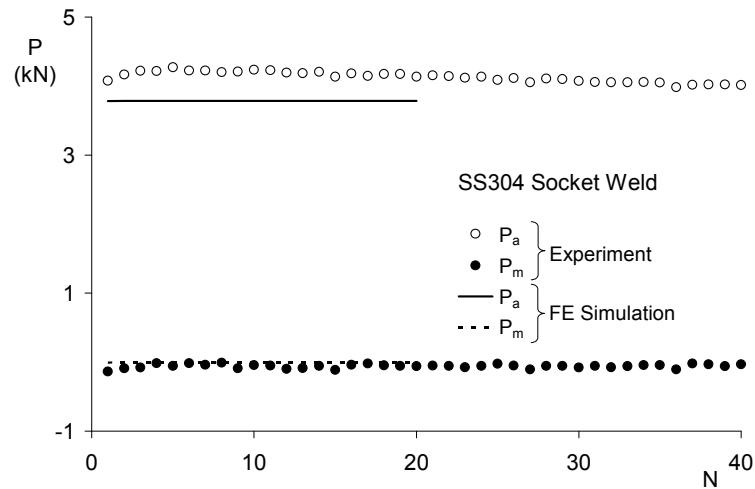


Fig. 2.32. Load response versus number of cycles from experiment and simulation

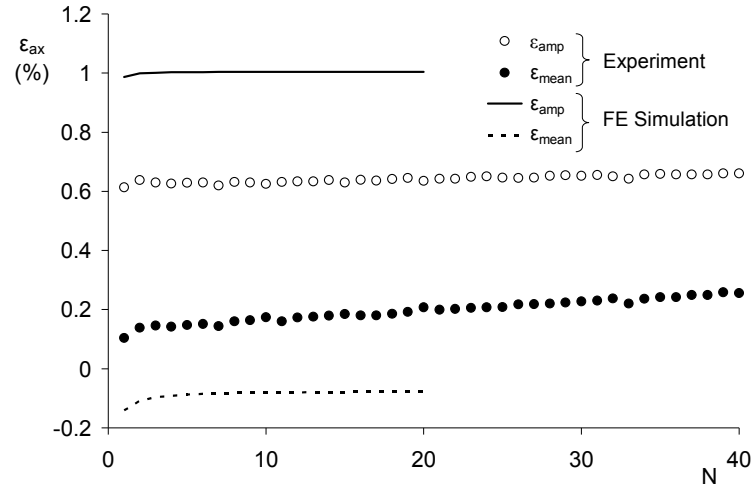


Fig. 2.33. Axial strain response at top 5mm from weld toe versus number of cycles from experiment and simulation

The axial welding residual stress and the relaxation after loading cycles on top of pipe outer surface from simulation are plotted in Fig. 2.34. Only few cycles of residual stress data are shown in Fig. 2.34 because residual stress distribution does not change after 3rd cycle. The welding residual stresses (cycle 0) are compressive and post-fatigue residual stresses are positive. The residual stresses were always larger near weld toe and decrease with distance from weld toe. It is not sure if the residual stresses were correctly simulated. The measurement of residual stress is needed to verify the simulation.

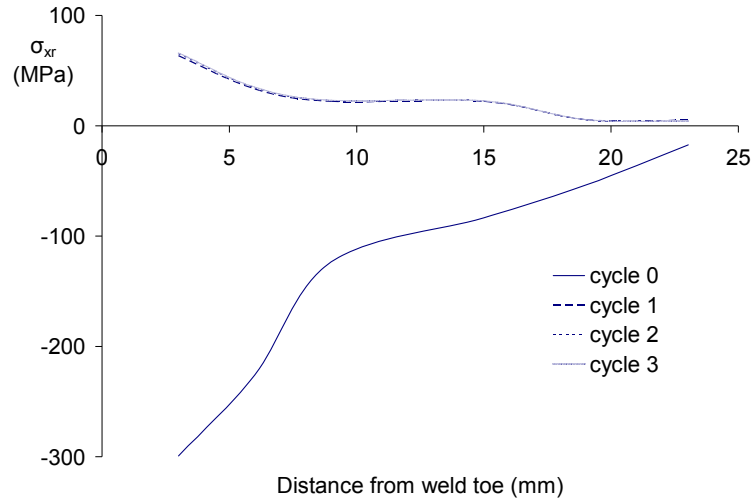


Fig. 2.34. Axial residual stress distribution on top of pipe outer surface after various cycles from simulation

DISCUSSION AND CONCLUSIONS

A technique of simulating welding procedure using FE program was introduced. This technique is using sequentially uncoupled nonlinear transient thermo-mechanical method, which calculates temperature from thermal simulation before applying temperature history as input for the mechanical simulation. Element birth/death technique was employed to represent the weld beads. Temperature dependent material properties were used on both welding thermal simulation and welding mechanical simulation. Bilinear kinematic hardening model was used on mechanical simulation. The calculated temperature history from thermal simulation was verified with measured data, and found to be in good agreement with measured data. The calculated initial welding residual stresses from mechanical simulation were also verified with experimental data, and the agreement was reasonable.

The FE model used on welding simulation was kept for subsequent fatigue response simulation. Bilinear kinematic hardening model was used on fatigue response simulation. The calculated force response from simulation could not simulate material hardening behavior observed from experiments. The force-displacement curve from simulation does not fit experimental data very well, either. In addition, strain amplitudes near weld toe were overpredicted.

Some recommendations are made regarding welded piping joint fatigue loading tests for future research. One is to use a proper method to measure strain response at weld toe, the crack tip. Since weld toe is a location of geometry discontinuity, installing strain gage is infeasible. Another change might be needed on measuring strain is to avoid zero-shift problem from strain gage.

The recommendation for numerical simulation as future work would be making some adjustments to the simulation. One part of modifications can be made is using a better material model on fatigue response simulation. For instance, using the Chaboche model or other advanced constitutive model would improve the force prediction to make force-displacement curve closer to experimental data. Also, the ratcheting response observed from experiments could be simulated using the new model. Another modification can be made is using proper material properties at HAZ that could make better strain response prediction near weld toe. This part of work would require material tests on temperature-conditioned material and parameter determination.

CHAPTER 3

Residual Stresses in Small Bore Socket-Welded Piping Joints under Low-Cycle Fatigue Loading

ABSTRACT

Early fatigue failures of small bore socket-welded piping joints have been a major problem in nuclear power industry during the past couple of decades. Residual stresses, generated near welded joint as a consequence of local plastic deformation during rapid heating and slow cooling process of welding, is one of the factors causing fatigue failure of welded joints. This chapter makes effort to determine the initial residual stress state in small bore pipe welded joints and how it is influenced by the weld sequence. This study presents experimental measurements and finite element simulations of residual stress on welded piping joints. The initial residual stresses on welded piping joints, measured using x-ray and neutron diffraction methods, was observed both large tensile and compressive at HAZ and the magnitude is large near weld toe. The axial residual stresses of stainless steel piping joints are mostly relaxed after 5 cycles. The change of mechanical material properties due to high temperature exposure was also studied. It was obtained that some mechanical material properties changed after subjecting to high temperature cycles, and the changed material was correlated to the peak temperatures. A modified thermo-mechanical material heterogeneity model was developed to improve residual stress simulation at HAZ.

INTRODUCTION

Early fatigue failures of small bore socket-welded piping joints have been a major problem in nuclear power industry during the past couple of decades. It is indicated in the last chapter that the factors causing fatigue failure of welded joints include stress concentrations, material heterogeneity, and residual stresses. This chapter will make effort to determine the initial residual stress state in small bore pipe welded joints and how it is influenced by the weld sequence. Residual stresses are generated near welded joint as a consequence of local plastic deformation during rapid heating and slow cooling process of welding. The magnitude of residual stress at welded joints could be higher than the yield stress of base metal [Zhang et al., 2005].

It has been concluded by many studies that compressive residual stress is beneficial while tensile residual stress is detrimental to fatigue strength [Chiarelli et al., 1999, Higuchi et al., 1998, Iida et al., 1997, Mochizuki et al., 2000, and Teodosio et al., 2003]. Riccardella et al. [1998] also observed that post weld heat treatment (PWHT) increased fatigue life by significantly relieving residual stresses. However, some studies published recently stated that the relationship between the welded joint residual stress and fatigue life is not clearly understood. Nikitin and Besel [2008] concluded that the correlation between cyclic lifetime to failure and residual stress for conventional deep rolled AISI 304 as well as SAE 1045 is not pronounced. The fatigue test result of Barsoum [2008] showed no increase in fatigue strength for the stress relieved tubular structures compared with the as-welded, due to the relieving of the compressive residual stresses.

It is well accepted that the initial residual stresses relax with fatigue loading cycles. The magnitude of relaxation of residual stresses depends on load type, load amplitude, and number of cycles. Iida et al. [1997] discovered that the welding residual stresses are considerably relieved by the first loading cycle, and then gradually relieved with an increasing number of repetitions of the same stress amplitude. After repetition of 10^4 cycles of the same stress amplitude, the residual stress

relaxed to a value of 46% of the initial value. Blom [1995] indicated significant stress relaxation (50% or more) that occurred early in the fatigue life (within 8% of total specimen life) at stress levels for which fatigue life is about 10 million. Lachmann et al. [2000] also observed that after the first load cycle, the residual stresses in the weld seam relax significantly dependent on the load stress. The magnitude of this residual stress relaxation normally increases with a higher load stress due to the increase in plastic deformations. Nikitin and Besel [2008] concluded that the residual stress can be correlated to the plastic strain amplitude.

The residual stress measurement techniques widely used are hole drilling, x-ray diffraction, and neutron diffraction. Hole drilling method is relatively handy and cheap, but could introduce extra residual stresses in steels caused by various material-removal processes [Withers and Bhadeshia, 2001 and Ruud, 2002]. Non-destructive methods like x-ray diffraction and neutron diffraction can provide more accurate results. X-ray diffraction method is used to measure residual stresses within the top layer of about 20 μm in thickness [Joseph et al., 2005]. The surfaces of measurement locations have to be electro polished prior to the measurement. Different surface conditions (sanding and/or electro polishing) could induce residual stress up to 60% of the yield stress (365 MPa) in SS304 pipe [Humphreys, 2004]. Neutron diffraction method can measure the change in lattice spacing several centimeters deep into metals [Webster, 2000]. Different measurement techniques at the same location yield different results. For example, Smith et al. [2001] obtained complete relaxation from a specimen after large plastic strain cycles using hole drilling, but obtained -150 MPa residual stress using x-ray diffraction.

Most of the fatigue studies presented above are related to high-cycle fatigue. Residual stresses are usually assumed to relax completely after a few cycles of low-cycle fatigue. However, Lu [2003] and Humphreys [2004] observed ratcheting behavior on welded piping joints under low-cycle fatigue.

Ratcheting usually happens when a mean stress exists in the material. Therefore, it is anticipated that the residual stresses in welded specimens may not completely relax with fatigue cycles and acted as the mean stresses causing ratcheting behavior. To explore the state of residual stress with fatigue cycle will be the main objective of this research.

This study presents experimental residual stress measurements on socket welded piping joints at various stages of fatigue life and finite element simulations of initial residual stresses induced by welding. Low-cycle fatigue experiments under displacement-controlled and force-controlled loading cycles were conducted on welded piping joints in a cantilever setup. Residual stresses in the welded piping joints of stainless steel (SS304) and carbon steel (CS1020, ASTM A513/5) were measured before and after fatigue loading cycles using x-ray and neutron diffraction techniques at Oak Ridge National Laboratory. Numerical simulations for initial residual stresses were performed using finite element program ANSYS and ABAQUS. Change in material properties at the heat affected zone (HAZ) due to the exposure of high temperature cycles during welding was studied. A material model is developed to incorporate the changes of material properties of the HAZ in the finite element simulation. Finally, the relaxation of residual stresses due to the fatigue loading cycles is presented.

WELDED SPECIMENS

Welding of specimens was carried out manually using Tungsten Inert Gas (TIG) arc welding technique. The list of specimens in Table 3.1 includes type of material (stainless steel (SS)/ carbon steel (CS)), type of welded joint (butt weld/ socket weld), and type of design (ASME/ modified ASME). The type of welded joint studied was fabricated using 3 weld passes, initially tack welded followed by quarter circumferential weld beads to avoid distortion of specimens. The sequence of the tack and quarter circumferential welding is shown in Fig. 3.1.

Table 3.1. Lists of specimens, fatigue loading, and residual stress measurement cycles

Material	Specimen	Weld type	Fatigue loading	Fatigue loading rate	σ_R at N			Weld Design
SS	BW2	Butt	$\delta_c = 14\text{mm}$	4sec/cyc	0	400		ASME
	SW5	Socket	$\delta_c = 14\text{mm}$	4sec/cyc	0	400		Modified
	SW6	Socket	$P_c = 3.5\text{kN}$	4sec/cyc	0	200		Modified
	SW7	Socket	$\delta_c = 14\text{mm}$	4sec/cyc	0	160	480	Modified
	SW8	Socket	$\delta_c = 10\text{mm}$	3sec/cyc	0			Modified
	SW9	Socket	$P_c = 3.5\text{kN}$	4sec/cyc	0	100		ASME
	SSPC2	Socket	$\delta_c = 10\text{mm}$	4sec/cyc	0	20		ASME
	SSPC3	Socket	$\delta_c = 10\text{mm}$	4sec/cyc	0	100		ASME
	SSPC4	Socket	$\delta_c = 10\text{mm}$	4sec/cyc	0	5		ASME
CS	CSPC5	Socket	$\delta_c = 11\text{mm}$	4sec/cyc	0	50		ASME
	CSPC6	Socket	$\delta_c = 11\text{mm}$	4sec/cyc	0	20		ASME
	CSPC7	Socket	$\delta_c = 10\text{mm}$	4sec/cyc	0	5		ASME

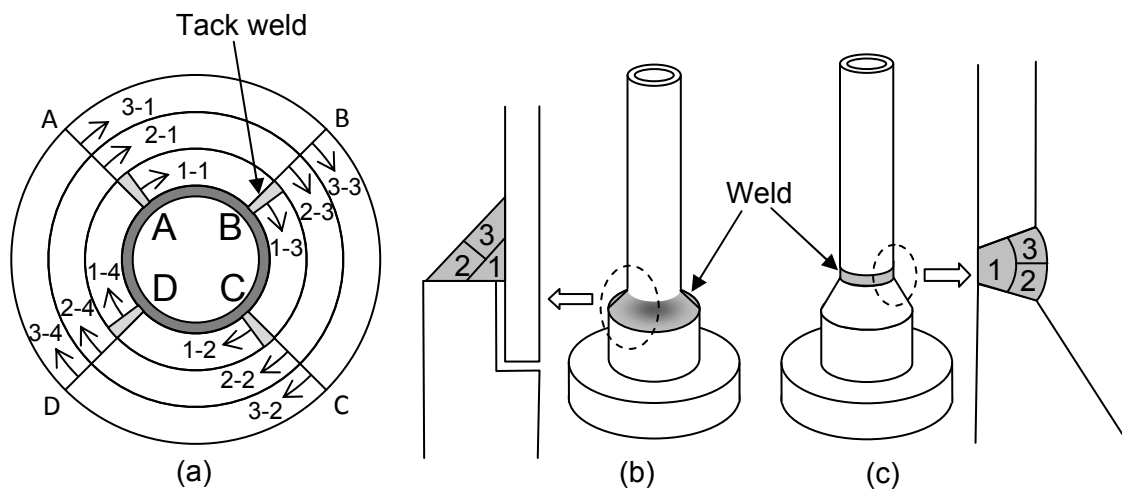


Fig. 3.1. (a) Tack weld and quarter circumferential weld sequences. Sequence of tack welds is A-C-B-D, before circumferential quarter welding in the sequence of 1-1, 1-2, 1-3, 1-4, 2-1, ..., 3-4. (b) Socket weld and three weld bead sequence. (c) Butt weld and 3 weld bead sequence

TECHNIQUES OF RESIDUAL STRESS MEASUREMENTS

Initial residual stresses near the weld toe were measured using x-ray diffraction and neutron diffraction techniques. The specimens were then subjected to displacement-controlled or force-controlled fatigue loading cycles as shown in Table 3.1 before measuring the residual stresses again. For the specimen SW7 residual stresses were measured twice, after 160 and 480 cycles. As the measurements of residual stresses before fatigue and at intermediate fatigue life were needed in this research, the sequence of steps mandated that the method of measurement be nondestructive in nature. Hence, x-ray and neutron diffraction techniques of residual stress measurement were considered in this study.

In x-ray diffraction, a dimension in the crystal lattice of the metal—the distance between atomic planes—is measured. The atomic planes act as strain gages. The atomic distance when the metal is subjected to stress is transformed to strain via comparison to the interplanar atomic spacing of the unstressed metal. Operating under the assumption that stress is proportional to strain, stress values

can be obtained by applying the elastic constant to the strains calculated from the measured interplanar atomic distances [Lu et al., 1994]. For a more thorough treatment of the theoretical background of x-ray diffraction, the readers are referred to Noyan and Cohen [1987].

Like x-ray diffraction, neutron diffraction is a nondestructive residual stress measurement technique in which the spacing between crystallographic planes is measured and used to determine the residual stress that exists in the metal [Ruud, 2002]. With the neutron diffraction, measurements of residual stresses can be obtained at depths up to a few centimeters. However, this technique cannot be used to measure the residual stresses on the surface. Fig. 3.2 shows the technique that the spacing in three orientations of a piping joint was measured using neutron diffraction method.

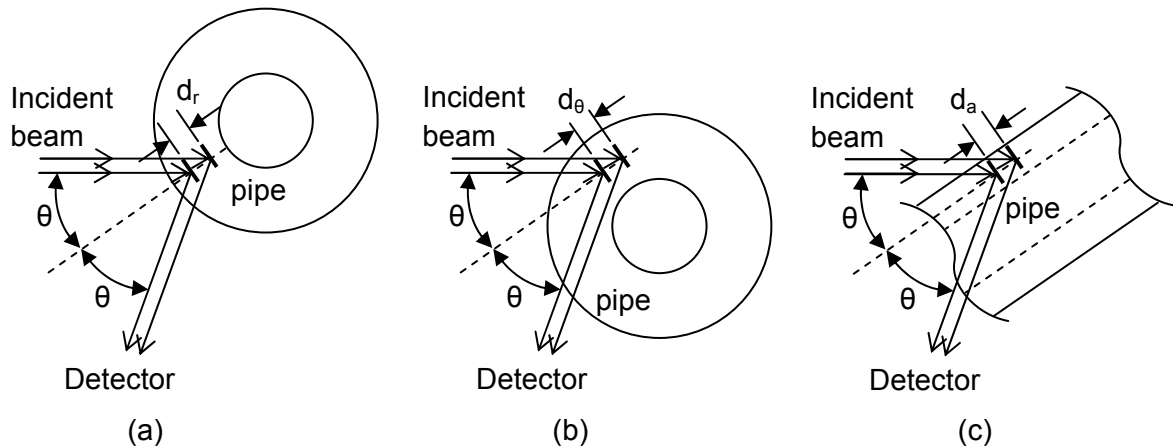


Fig. 3.2. Neutron diffraction measurements of residual stress of piping joints along (a) radial, (b) circumferential, and (c) axial directions

Most of the measurements were made along the middle of either AB or BC side (see Fig. 3.1). Residual stresses at multiple spots within 40 mm from weld toe were measured, as shown in Fig. 3.3. In the present study, axial and circumferential stresses on pipe outer surface were obtained using x-ray method. Additionally, axial, circumferential, and radial stresses at depths of 1, 2.5, and 4 mm from outer surface were obtained using the neutron diffraction method. All of the measurements were

conducted at Oak Ridge National Laboratory (ORNL) through the user program of the High Temperature Materials Laboratory (HTML).

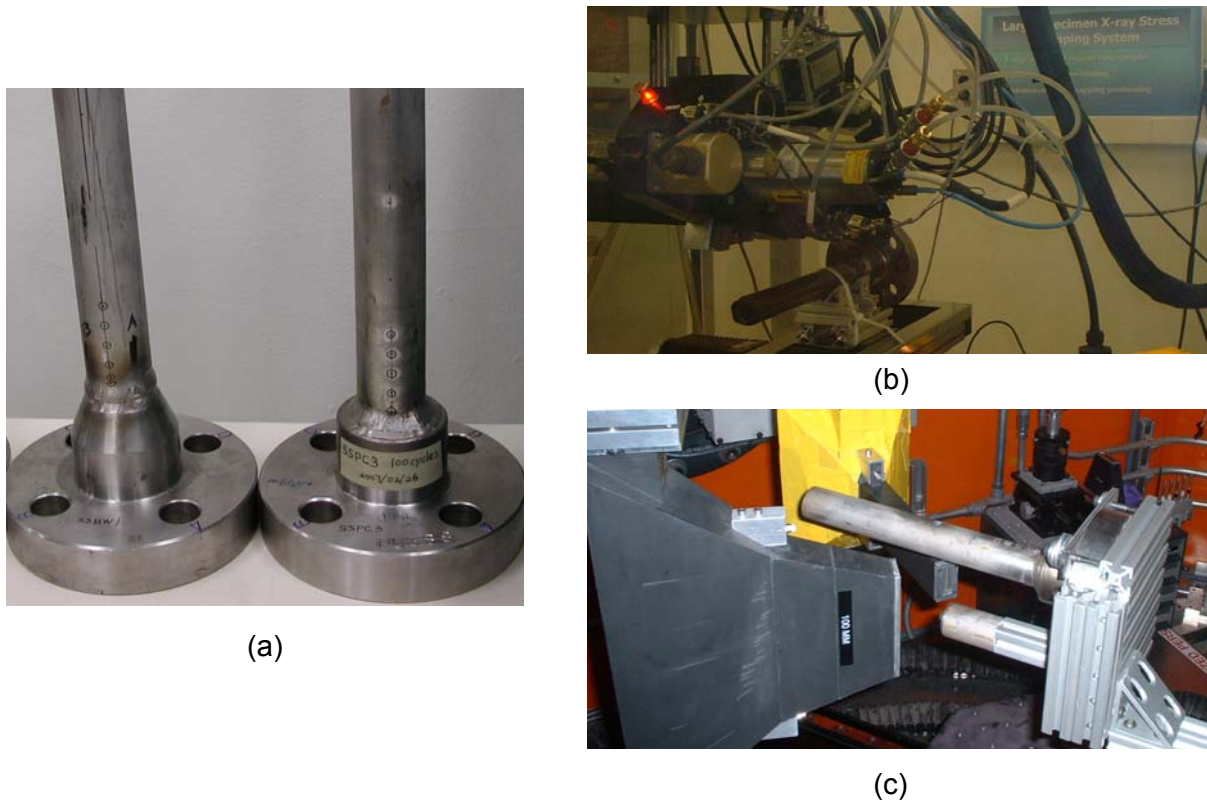


Fig. 3.3. (a) Measurement locations on butt weld and socket weld piping joints. (b) X-ray diffraction measurement setup. (c) Neutron diffraction measurement setup.

ERRORS OF X-RAY DIFFRACTION RESIDUAL STRESS MEASUREMENTS

A reproducibility test was conducted in Humphreys [2004] in an effort to establish practical error bars for interpretation of x-ray diffraction residual stress measurement results. The test is to repeat the measurements on a welded piping joint for five times. The axial and circumferential residual stress results are plotted in Figs. 3.4a and 3.4b, respectively. It can be seen in Fig. 3.4 that the general trends of residual stresses in both the axial and circumferential directions were well maintained in all five runs. The standard deviation at the measurement location where the largest difference between the maximum and minimum residual stress measurements existed was found to be 60 MPa. Therefore,

the error bars established for interpretation of x-ray diffraction measurements in this study were ± 60 MPa. Error in x-ray diffraction measurements is a combination of statistical error, arising from uncertainty in the absolute intensity of the diffracted beam at any position θ , and instrumental error, arising from specimen alignment and curvature and various other geometrical factors [Noyan and Cohen, 1987].

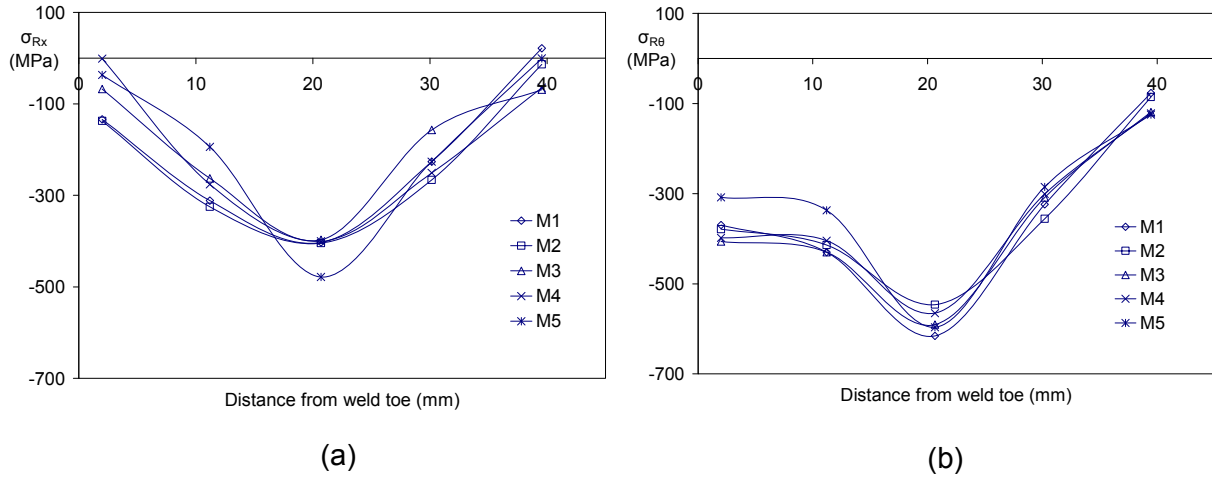


Fig. 3.4. Measured residual stress in reproducibility test (a) axial data, (b) circumferential data. [from Humphreys 2004]

RESULTS OF RESIDUAL STRESS MEASUREMENTS

The residual stresses measured using the x-ray diffraction and neutron diffraction techniques are presented in this section. To understand the effect of weld design, material type, fatigue cycle, loading type, and depth from surface, the data are presented in separate groups. During fatigue loading, the maximum strain responses obtained are at middle of AB (top of the specimen), hence only the residual stresses at middle of AB are presented.

INFLUENCE OF WELD JOINT GEOMETRY

In the ASME code, an axial gap (usually 1/16 inch) is required for socket welded joints. Several specimens with a modified design of socket welded joint without a gap were tested and longer fatigue

life were obtained compare to original ASME design . In Table 3.1, the specimens SW5, SW6, SW7, and SW8 are fabricated using the modified design, and others are original ASME design. The modified design and the fatigue life improvement will be presented in a future paper.

The initial axial residual stresses of stainless steel butt weld, socket weld with ASME design, and socket weld with modified design are plotted in Fig. 3.5. The magnitude of residual stresses and basic distribution trend along the pipe surface length of all three specimens is similar, which is higher compressive stress near weld toe and gradually decreases as the distance increases from the weld toe. A minor difference in the stress distribution between the socket and butt-weld is that the maximum compression in the butt weld occurs at the weld toe, whereas in socket weld the maximum compression stress occurs away from the weld toe. It is surprising that despite the higher stress concentration factor of the socket weld compare to the butt weld, the residual stresses at the toe are of comparable magnitude.

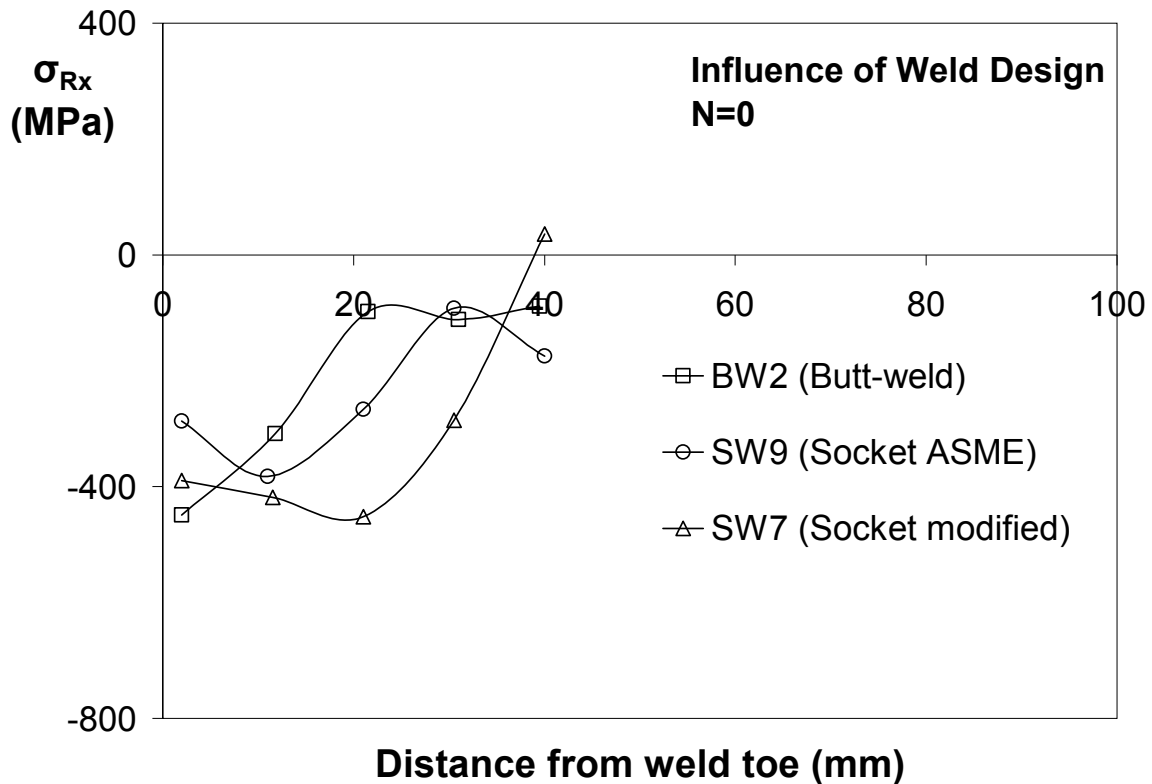


Fig. 3.5. Initial axial residual stresses in a butt weld, ASME socket weld and a modified socket weld

INFLUENCE OF WELD JOINT MATERIAL

The comparison of initial axial residual stresses in stainless steel and carbon steel socket welded joints are shown in Fig. 3.6. It is observed in this figure that for both materials large compressive residual stresses are developed in the axial direction due to welding within 10 mm from the weld toe. Also note for that all three carbon steel socket welded joints that the axial residual stresses are larger little away from the weld toe. Such distribution is observed only for one stainless steel socket weld specimen, SSPC3. For the other two stainless steel specimens, the residual stress distribution is erratic for making the same conclusion.

The residual stresses in stainless steel socket welded joints are greater than in the carbon steel socket welded joints. As the yield stress of stainless steel base metal is about 350 MPa, some of the initial residual stresses of stainless steel exceed the yield limit. On the other hand, the yield stress of carbon steel base metal is about 630 MPa. The maximum residual stress observed in carbon steel did not exceed the yield limit.

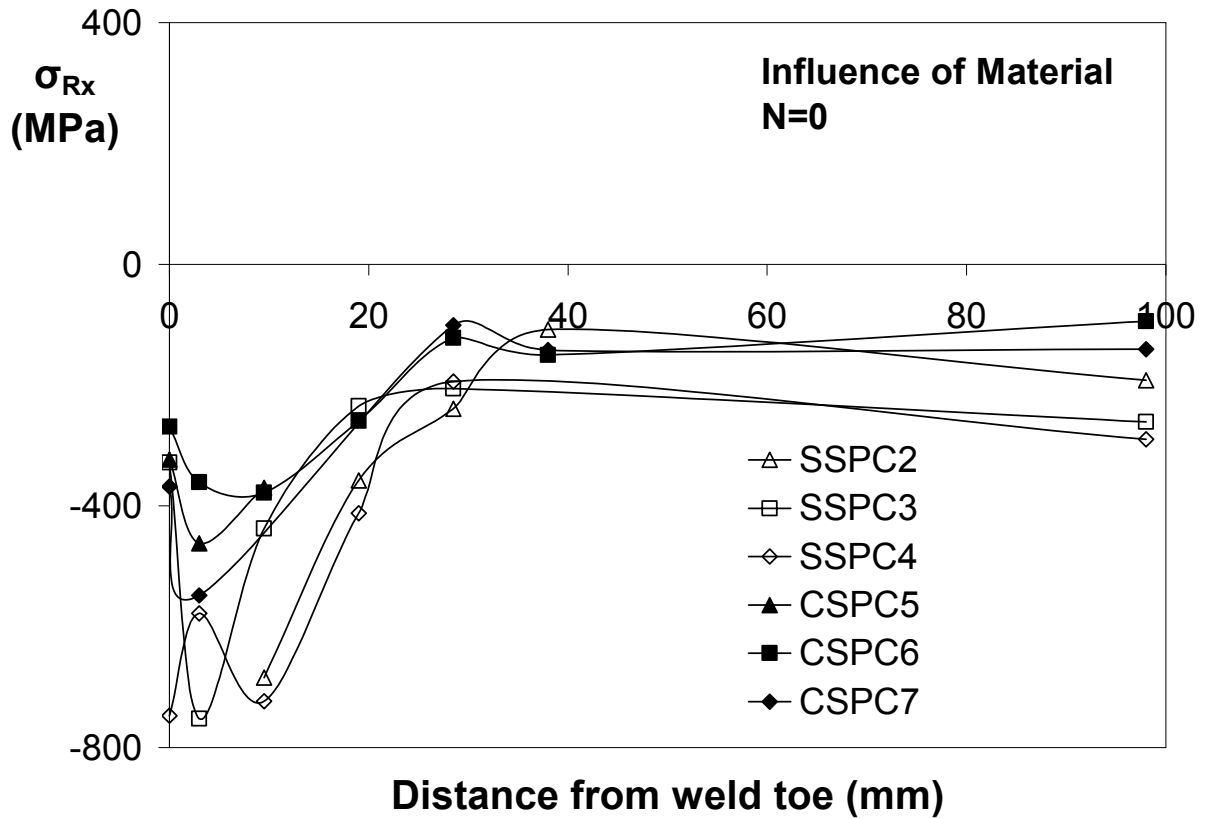


Fig. 3.6. Initial axial residual stress in stainless steel and carbon steel socket welded joints

INFLUENCE OF THE NUMBER OF FATIGUE CYCLE

In this study, the residual stress relaxation with fatigue cycles were initially demonstrated by Humphreys [2004], who measured the residual stresses of specimens BW2, and SW5 to SW9 in Table 3.1. A typical set of residual stress relaxation data with fatigue cycles is shown in Fig. 3.7. Residual stresses were almost completely relaxed after 160 cycles. In fact, Humphreys discovered that initial residual stresses were totally relaxed even with the least fatigue cycles (SW9 with 100 cycles), which indicated that residual stresses might have relaxed much earlier.

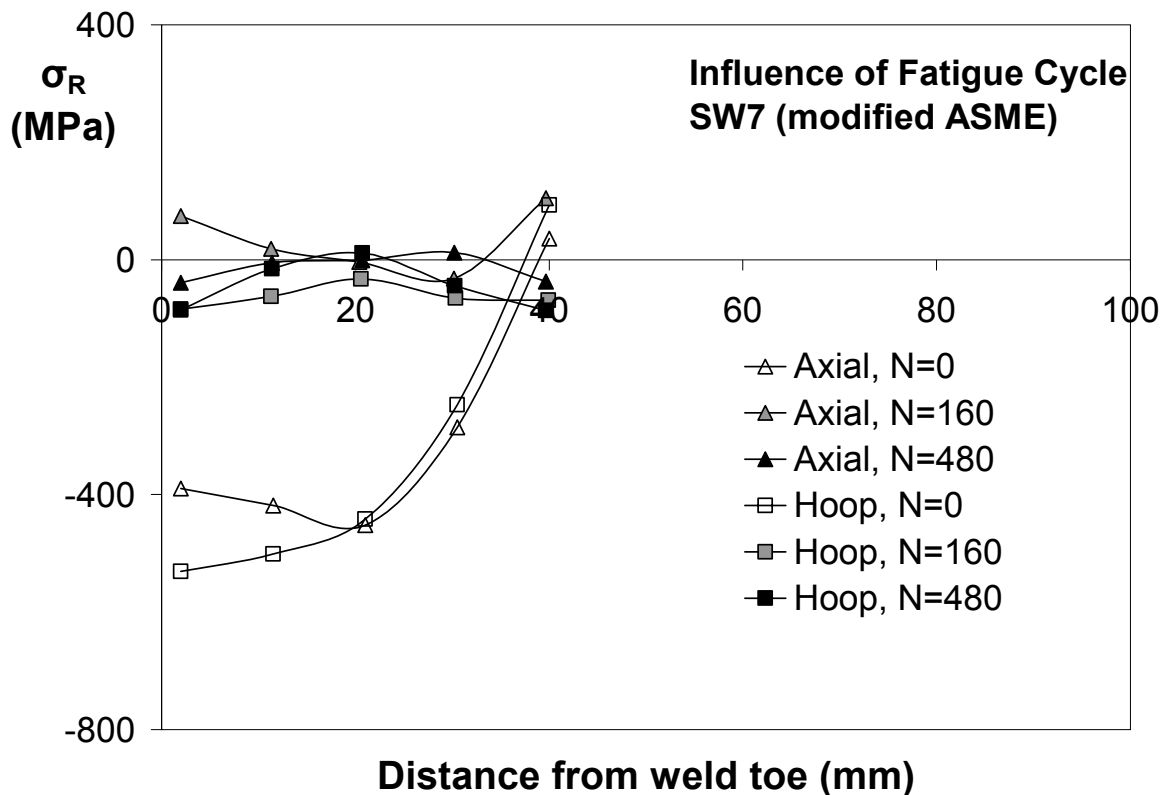


Fig. 3.7. Axial residual stress relaxation of SW7 stainless steel socket welded joint with fatigue cycle N

Subsequently, the tests of SSPC2, SSPC3, and SSPC4 socket welded joints were subjected to fewer cycles before the residual stress measurements. The measured axial residual stress data in these three specimens before and after fatigue loading cycles are plotted in Fig. 3.8. In Fig. 3.8, it is

observed that the residual stresses in all three specimens, subjected to 5, 20 and 100 fatigue cycles, relaxed to about the same level of residual stresses within the 20 mm of the weld toe. For more than 20 mm from the weld toe, no specific trend of stress relaxation is identified. The post-fatigue residual stresses of SSPC3 and SSPC2 can be considered to be of the same magnitude if error bars of x-ray diffraction measurements are taken into account, while SSPC4 relaxed less. The reason that residual stresses relaxed more near weld toe is that the strain amplitude near the weld toe experience large plastic strain cycles. It can be concluded from Fig. 3.8 that for stainless steel welded piping joints the residual stresses relaxed considerably by 5 fatigue cycles and almost no significant relaxation observed afterward.

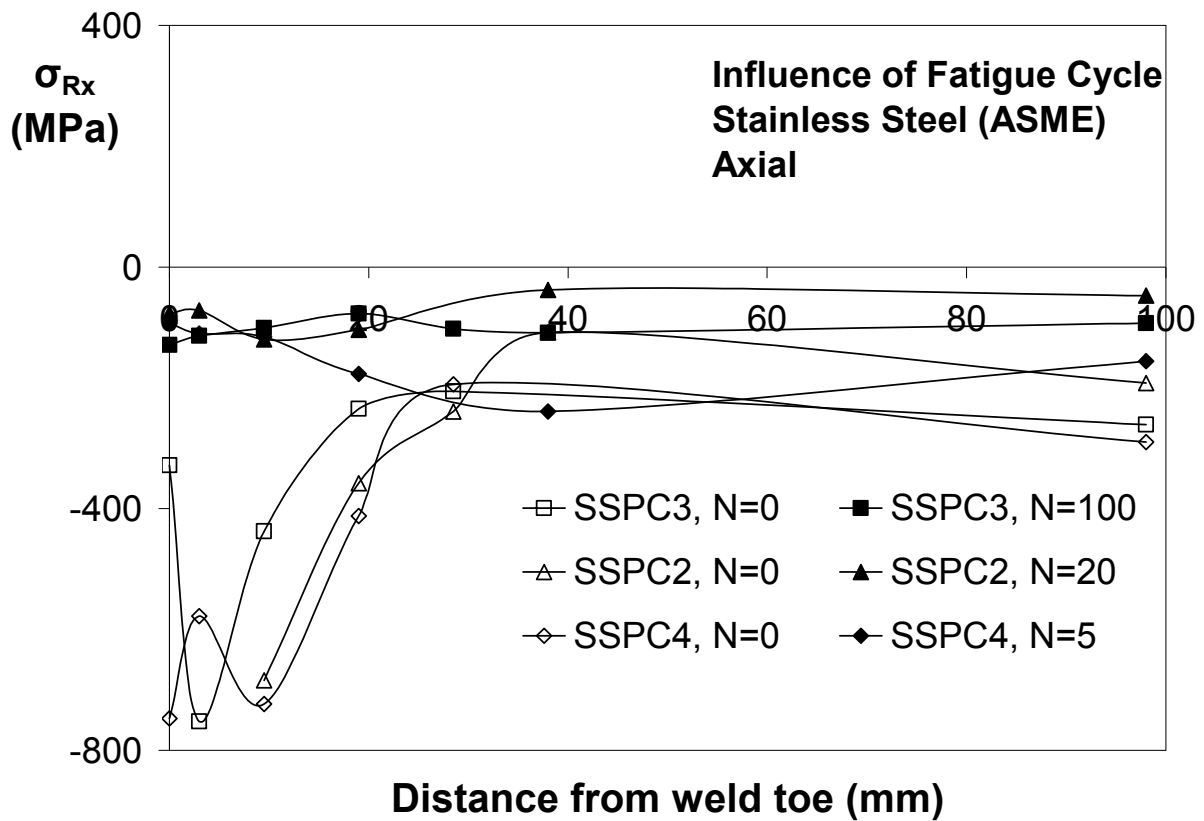


Fig. 3.8. Axial residual stress relaxation of stainless steel socket welded joints with fatigue cycle N

The relaxation of carbon steel socket welded joints after various fatigue cycles is plotted in Fig. 3.9, where it is observed that the level of relaxation is influenced by the number of fatigue cycles. The relaxation of residual stress gradually increases from 5 to 20 to 50 cycles. The residual stresses after 50 cycles seems to be completely relaxed near the weld toe. It also can be concluded that residual stress relaxation rate is lower in carbon steel than in stainless steel.

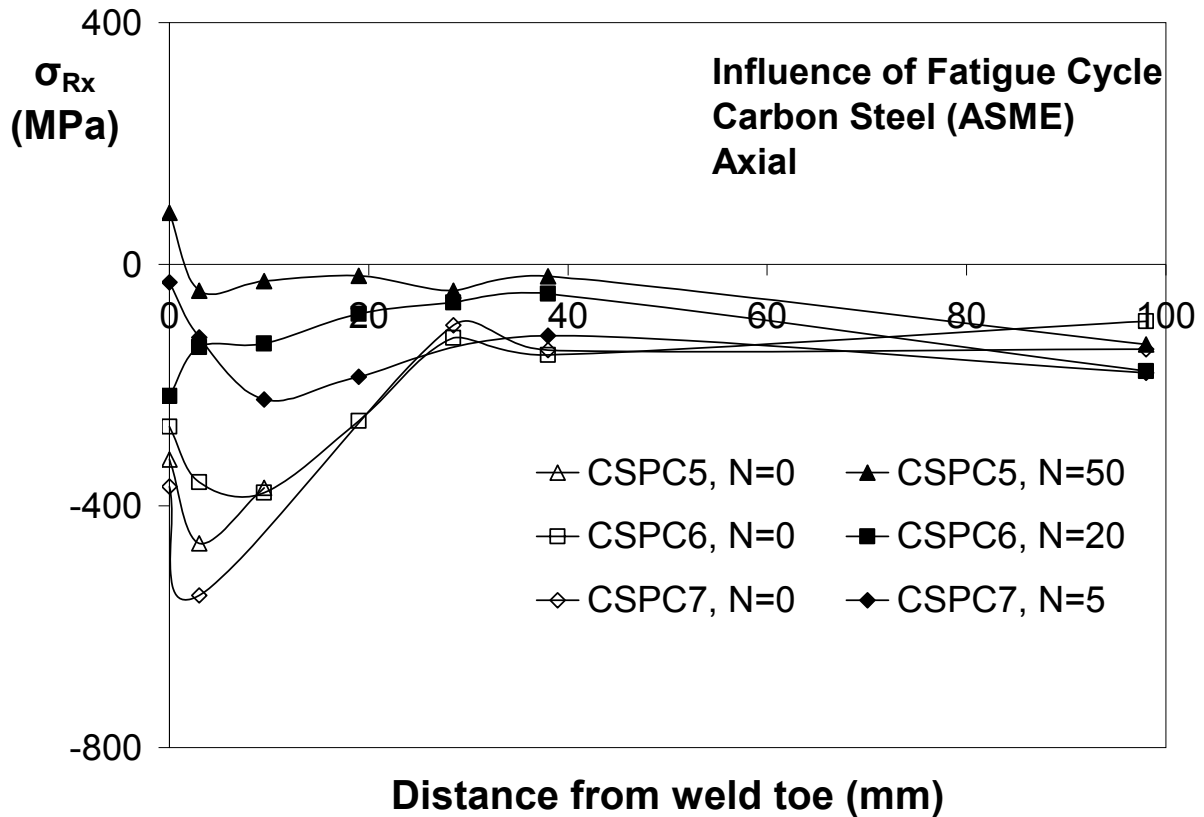


Fig. 3.9. Axial residual stress relaxation of carbon steel socket welded joints with fatigue cycle N

INFLUENCE OF FORCE VERSUS DISPLACEMENT-CONTROLLED CYCLES

To study the influence of the type of load control on residual stress relaxation, axial and circumferential residual stress data from specimen SW9 (subjected to force-controlled loading cycles) and SSPC3 (subjected to displacement-controlled loading cycles) are compared in Fig. 3.10. After 100 fatigue cycles, the residual stresses (both axial and circumferential) in the force-controlled

specimen seems to be tensile, whereas that in the displacement-controlled specimen they are compressive. As these stress levels after the 100 fatigue loading cycles are within the error bar, it is not possible to make any conclusion on the influence of load control on the stress relaxation. However, some light on this aspect can be shed from fatigue response simulation in the next chapter.

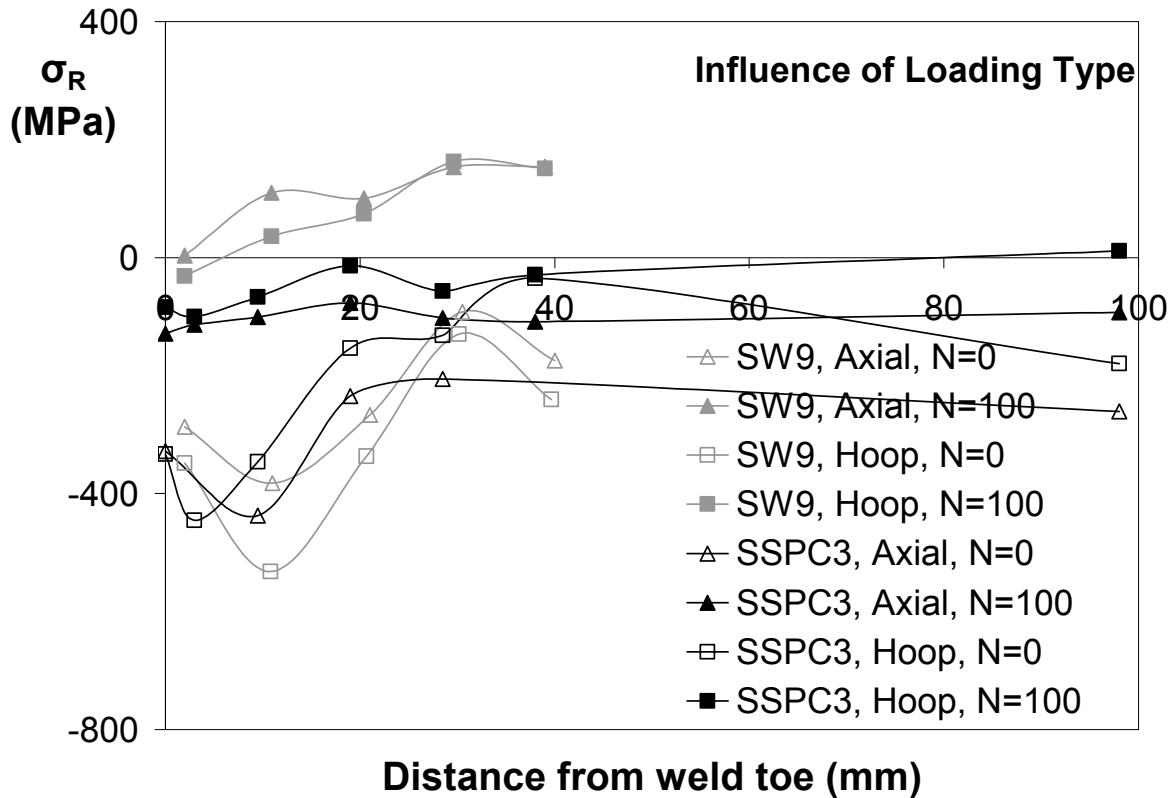


Fig. 3.10. Relaxation of residual stresses of SW9 (force-controlled) and SSPC3 (displacement-controlled) after 100 fatigue cycles.

INFLUENCE OF DEPTH AT THE WELD TOE ON RESIDUAL STRESS

The initial and intermediate fatigue life residual stresses of weld specimen SSPC3 were measured at various depths (1mm, 2.5mm, and 4 mm) from pipe outer surface at various distances from weld toe using the neutron diffraction technique. The results are shown in Fig. 3.11. The neutron diffraction residual stresses in Figs. 3.11a, 3.11b, and 3.11c along with the surface residual stresses from the x-ray diffraction in Fig. 3.6 demonstrate that the initial residual stress decreases with depth.

The difference between the surface and 1 mm depth could also be contributed by the different measuring techniques (x-ray vs. neutron). However, the decrease in residual stress with depth is observed for all directions, axial, circumferential and radial. From the trend in change of the residual stress with depth, it also seems that the residual stresses at the inner surface of the pipe might become tensile. It was not possible to measure residual stresses on the inner surface of the pipe using the neutron diffraction technique. In Fig. 3.11 d it is observed that the axial and hoop residual stresses become tensile at 1 mm depth after 100 fatigue cycles whereas these stresses at 2.5 mm depth remained compressive.

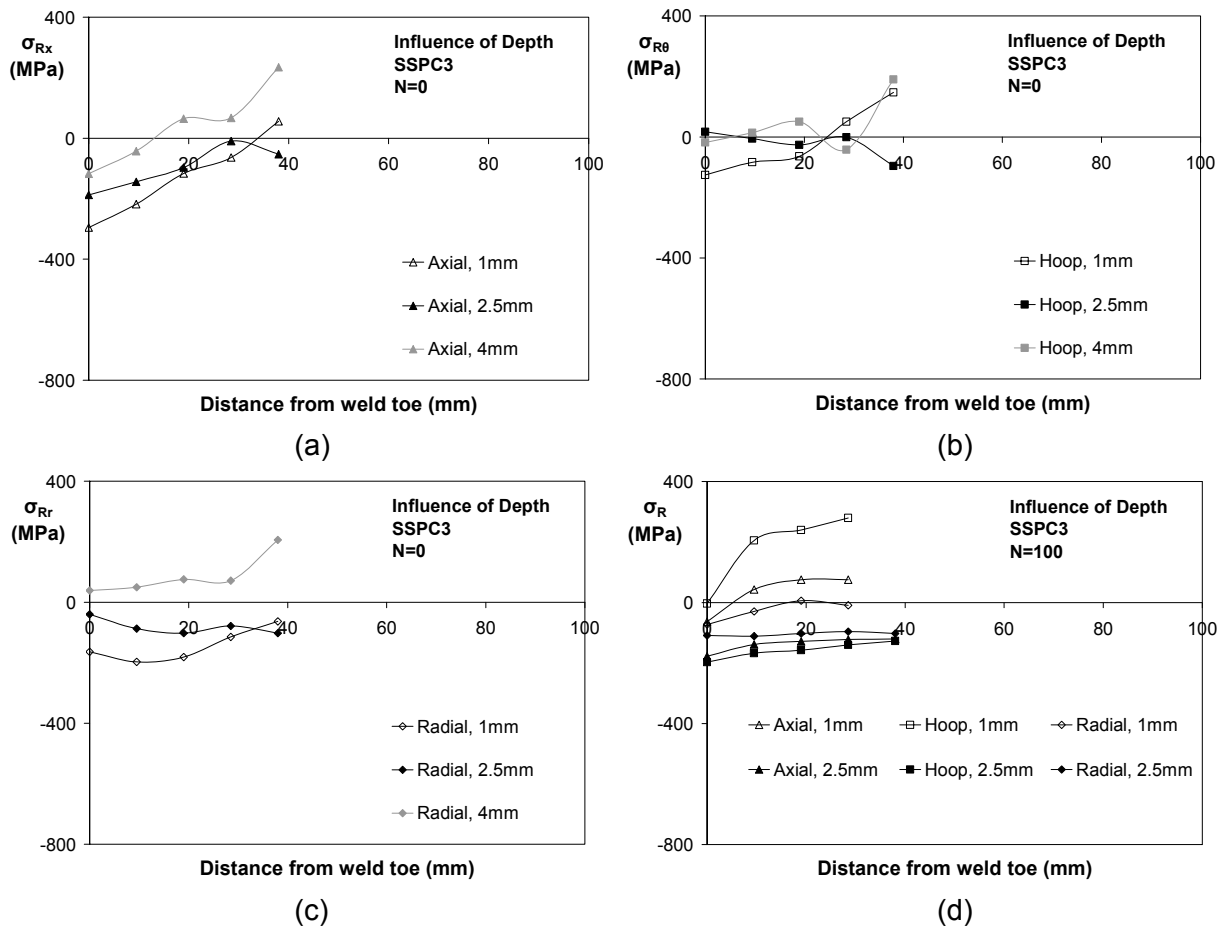


Fig. 3.11. Residual stresses measured at various depths from outer surface at various distances from the toe using neutron diffraction technique (a) axial data before fatigue loading, (b) circumferential data before fatigue loading, (c) radial data before fatigue loading, and (d) after 100 cycles.

SIMULATION OF RESIDUAL STRESS

In order to understand the overall residual stress distribution on welded piping joints, numerical simulations were performed using commercial finite element package. Sequentially uncouple nonlinear, transient thermo-mechanical analyses with element birth/death feature for the modeling of weld filler material were used in simulating the real-time welding process. Detailed simulation procedures are described in Lu [2003] and Chapter 2.

In Lu [2003] and Chapter 2 the residual stress simulation was first validated against the measured residual stresses of a butt-welded stainless steel pipe developed by Li [1995]. The agreement between simulated and measured residual stress data from Li [1995] was reasonable for most cases except near the weld toe. One of the possible reasons for this error might be the heterogeneity of heat affected zone (HAZ) metal which was exposed to high temperature cycles during welding process was not considered in the residual stress simulation. To improve the residual stress and subsequent fatigue response simulations, modeling of the material heterogeneity of the HAZ material properties is implemented in this study. The transformation of the homogeneous base metals to heterogeneous at the HAZ by welding and the application of heterogeneous material properties in the residual stress simulation are described below.

HETEROGENEOUS MATERIAL PROPERTIES DUE TO WELDING

The rapid increase of temperatures at three locations A, B and C near the weld toe during the filler metal deposition of a sequence and slow cooling after weld torch is removed is shown in Fig. 3.12. Material properties of the base metals exposed to high temperature changes because of their microstructural change. The zone in which base metal properties change during welding are referred to as the heat affected zone (HAZ). For instance, the base metal at location A is transformed by the peak temperature exposure of 1300°C during the welding process. On the other hand, the base metal at location B experiences different peak temperature (900°C) during welding, hence the metal at B

would be transformed to a different microstructure and hence will have different material properties than at A. Therefore, the material properties of the HAZ should be modeled as heterogeneous materials. A simple technique of modeling material heterogeneity of the HAZ is developed in this study and discussed below.

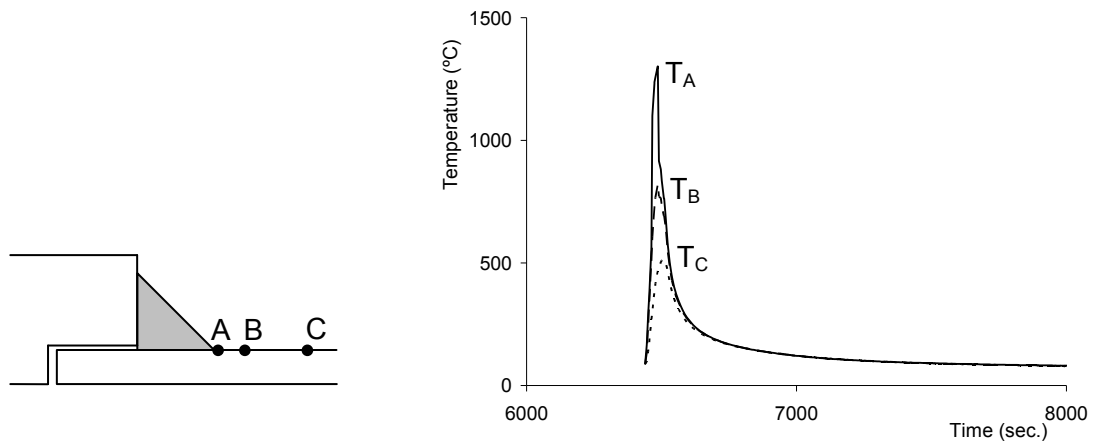


Fig. 3.12. Temperature history at various locations of the heat affected zone during welding.

To simulate the HAZ material state of a location, tubular specimens as shown in Fig. 3.13 machined from the same pipe stock used in the welded piping joints were exposed to a specified temperature cycle. Each specimen is exposed to an elevated temperature in a furnace for a short period and then slowly air cooled down to a room temperature. This temperature-conditioning procedure imitates the welding temperature cycle at a location of the HAZ during a weld sequence. In this study, specimens were conditioned by temperature cycles with peaks as 1080°C, 950°C, 800°C, 625°C, and 500°C. These specified temperatures were determined from the phase diagram and thermal analysis results discussed in Chapter 2. Next, cyclic loading tests were conducted on these temperature-conditioned specimens to determine their material properties. Three specimens were conditioned for each of the five conditioning temperature cycles. These three sets of specimens were

used for conducting three cyclic experiments: *axial strain-controlled cycle*, *axial forced-controlled cycle (uniaxial ratcheting experiment)*, and *biaxial experiment under steady internal pressure and axial strain-controlled cycle (biaxial ratcheting experiment)*. These loading paths prescribed in these experiments are shown in Fig. 3.13. In this study, only the monotonic responses from the axial strain-controlled experiments are used. Others experimental responses will be used in the next chapter where simulations of the fatigue responses are discussed.

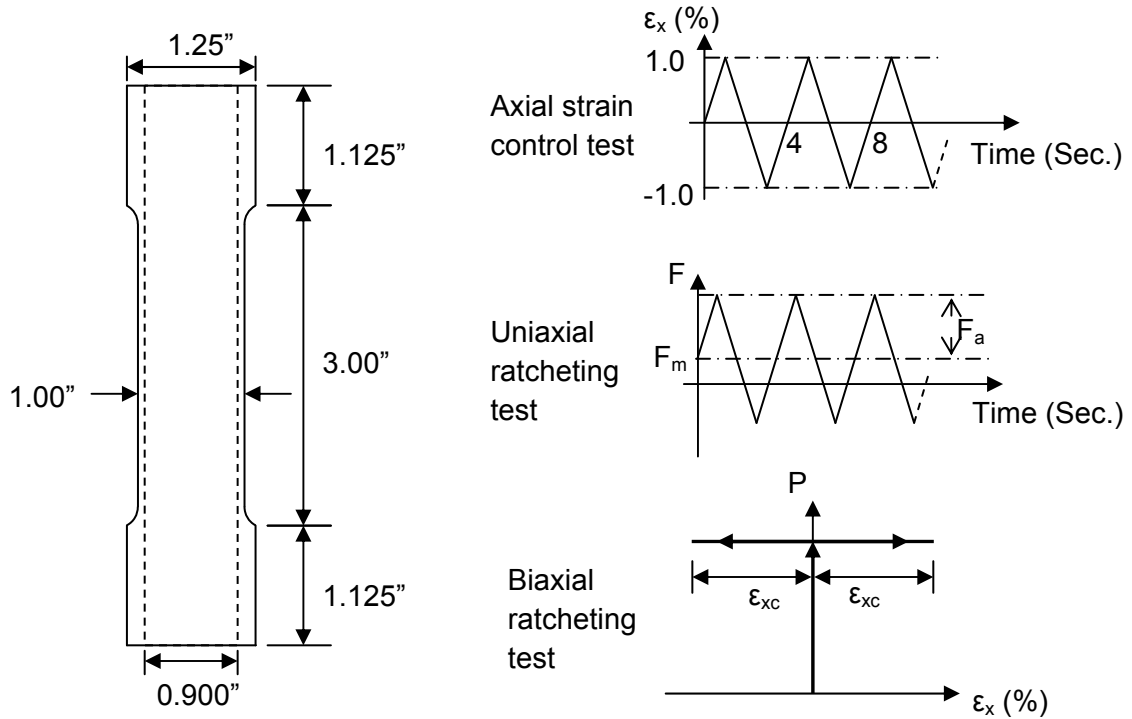


Fig. 3.13. Tubular specimen dimensions and the types of cyclic loading tests

The monotonic responses of the unconditioned and HAZ simulated specimens from the axial strain-controlled experiments are plotted in Fig. 3.14. Elastic modulus of all specimens is about the same, which is expected. However, it is interesting to note that the yield stress is changed significantly by the temperature conditioning. The yield stress of bilinear fit of the unconditioned specimen is 340 MPa and this value decreases as the conditioning peak temperature increases. This

yield stress change with the peak temperature conditioning ($T_{\text{peak}}^{\circ\text{C}}$) is plotted in Fig. 3.15. The tangent modulus of the bilinear fit also decreases by small amount with the peak conditioning temperature. These material results demonstrate that the material properties at the HAZ are heterogeneous because of the weld temperature exposure.

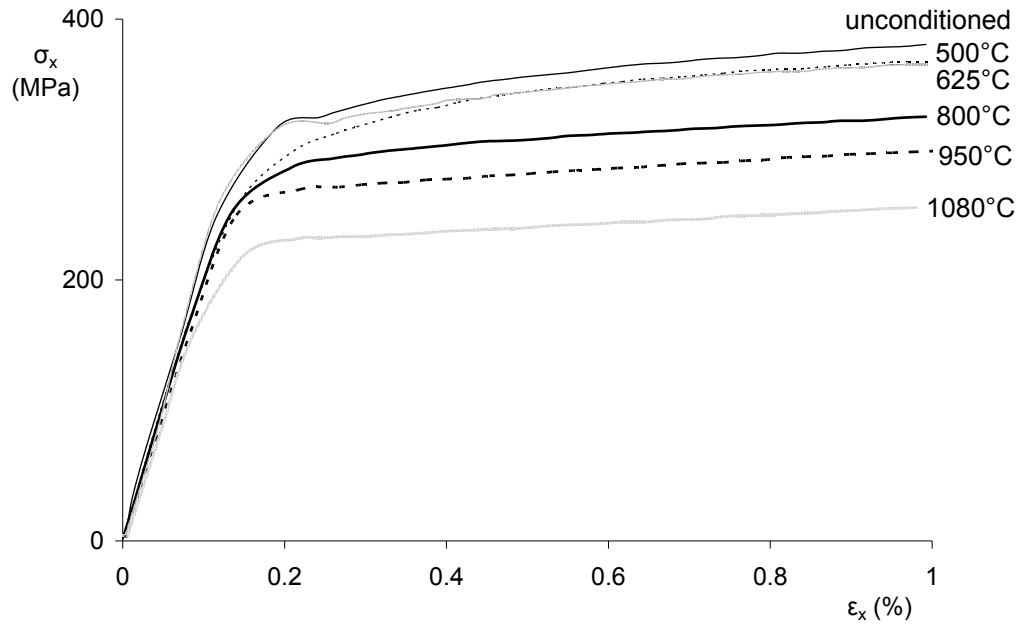


Fig. 3.14. Monotonic responses of unconditioned and temperature conditioned specimens

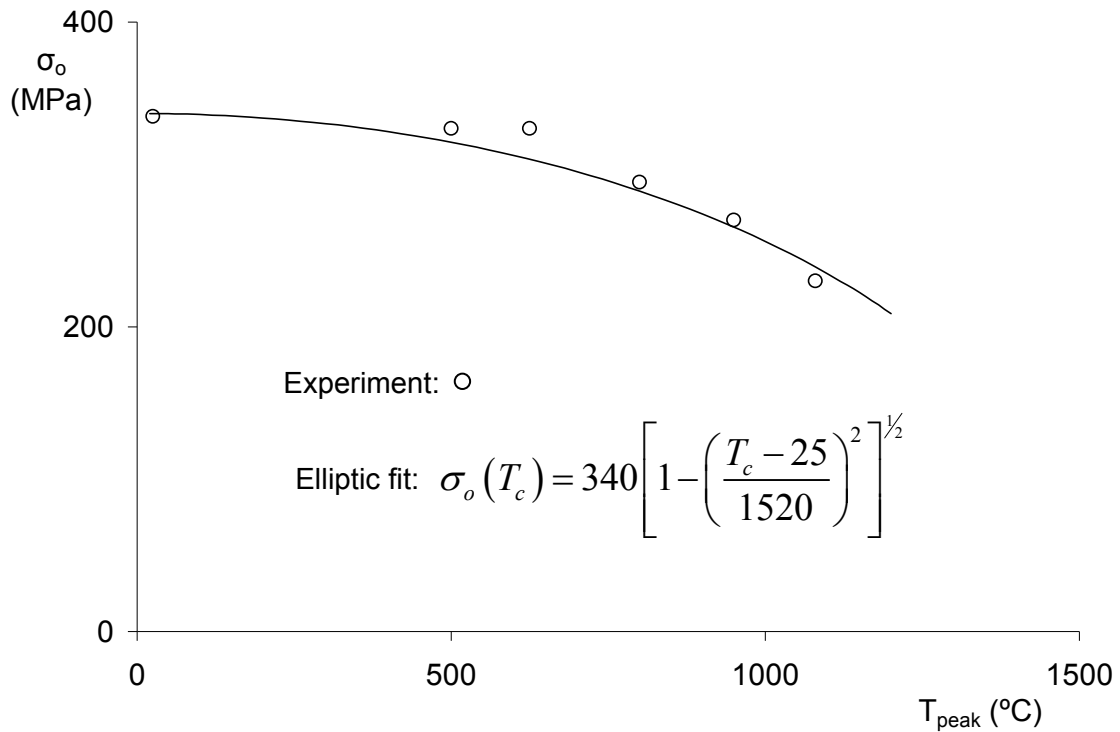


Fig. 3.15. Yield stress evolution of SS304 specimens with peak temperature of temperature conditioning cycle and an elliptic function fit of yield stress evolution.

To incorporate material heterogeneity into the residual stress simulation, the temperature dependent mechanical material properties which were used in Lu [2003] and Chapter 2 need to be modified. In the prior model, elastic modulus, yield stress and plastic modulus of bilinear fit decreases with increasing temperature and vice versa. That means when the material temperature decreases to the room temperature, the yield stresses increases to the level of uncondition specimens. This response is demonstrated by the solid curve in Fig. 3.16. However, it is observed in Figs. 3.14 and 3.15 that the actual phenomenon is different than assumed in the prior model. The actual evolutions of the yield stress with temperature cycles is modeled by the dashed lines as shown in Fig. 3.16. In Fig. 3.16 the solid circles represent experimental temperature-dependent yield stresses (from Kang et al. [2005], and Brickstad and Josefson [1998]), and open symbols represent room temperature

yield stresses after temperature-conditioning (obtained from Figs. 3.14 or 3.15). This modified thermal model is further explained below.

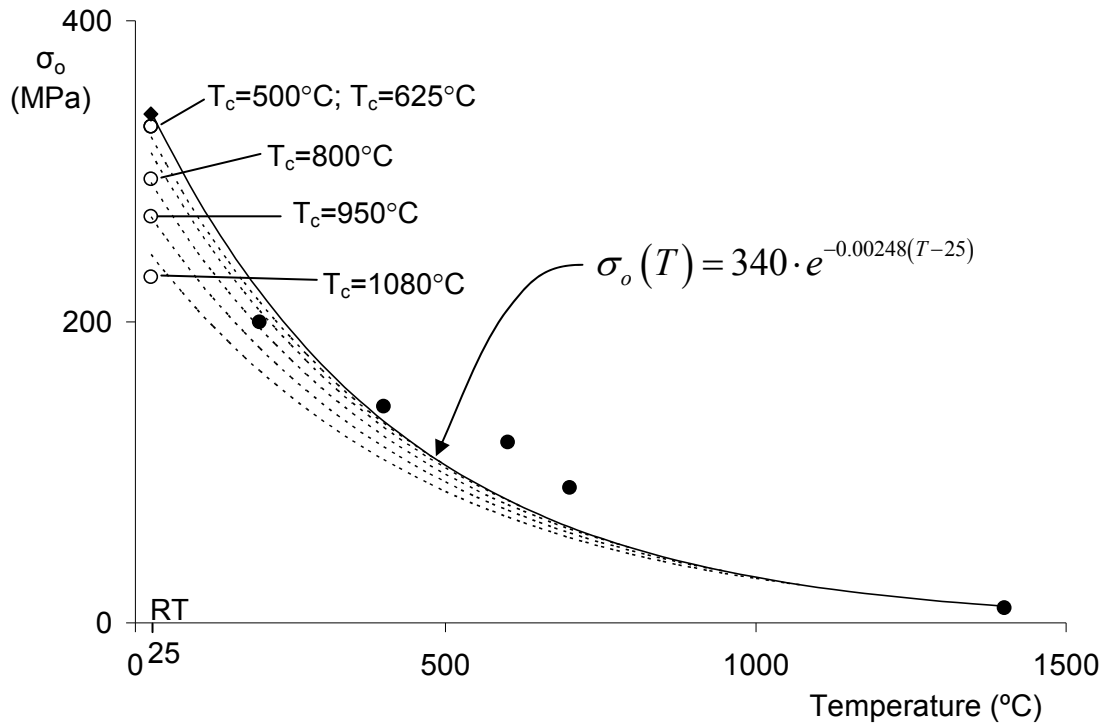


Fig. 3.16. Temperature dependent experimental yield stress of SS304 and their exponential function fit. Solid circles represent yield stresses data obtained from Kang et al. [2005] and Brickstad and Josefsen [1998].

The difference between the earlier residual stress analysis (basic thermal model in Lu [2003] and Chapter 2) and the modified residual analysis using the heterogeneous material properties (modified thermal model) is demonstrated in the sketched in Fig. 3.17. With the basic thermal model, when the material is heated up or cooled down, the yield stress evolution is determined by the solid line ABCD in Fig. 3.17. Consequently, the yield stress at 25°C (room temperature) is always determined by point A, no matter what was the peak temperature of the material during the last weld sequence. With the modified thermal model, the room temperature yield stress with prior peak temperature up to C would be given by E, arrived by following the path CFE during cooling. Similarly, with prior peak

temperature up to D the yield stress upon cooling would be given by H. Furthermore, during temperature increase from E, the yield stress evolution would follow the path EFCD.

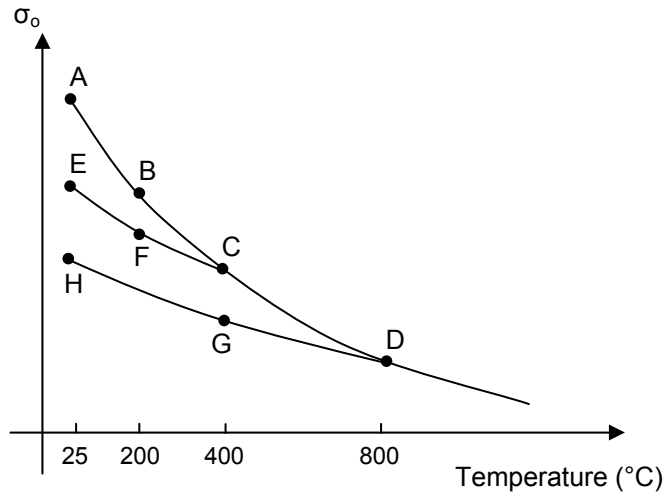


Fig. 3.17. Basic thermal model (ABCD) and modified thermal model for determining temperature-dependent yield stress evolution.

In the modified thermal model in Fig. 3.17, there is no experimental data available to define the paths CFE or DGH. In the present work, an assumption was made that the evolution of yield stress during cooling follow the same equation as the basic thermal model (solid line in Fig. 3.16).

Therefore, the yield stress as a function of temperature (basic thermal model) has to be determined first. By least-square fit of the solid circles in Fig. 3.16 (data from Kang et al. [2005] and Brickstad and Josefsen [1998]), an exponential fit, plotted as the solid line in Fig. 3.16, was determined as:

$$\sigma_o(T) = 340 \cdot e^{-c_o(T-25)} \text{MPa} \quad (3.1)$$

where, $c_o = 0.00248$ is determined by the least-square fit,

340 MPa is the yield stress of the unconditioned base metal, and

T is the current temperature (°C)

The yield stresses in the modified thermal model (plotted as dash lines in Fig. 3.16) would be given by:

$$\sigma_i(T, T_c) = 340 \left[1 - \left(\frac{T_c - 25}{1520} \right)^2 \right]^{\frac{1}{2}} \cdot e^{-c_i(T-25)} \quad (3.2)$$

$$\text{where, } c_i = \frac{\left[\ln \left(\frac{e^{-0.00248(T_c-25)}}{\left(1 - \left(\frac{T_c - 25}{1520} \right)^2 \right)^{\frac{1}{2}}} \right) \right]}{(25 - T_c)}$$

T_c : conditioned temperature/ updated peak temperature (°C)

In Eq. (3.2), the coefficient of the exponential term was determined by fitting the yield stress evolution data in Fig. 3.15; c_i was determined using the recent peak temperature T_c .

For the stainless steel material SS304, Johnson and Ramirez [SAC/BD-00/13] showed that after a single weld pass the base metal generally has five different microstructures depending on the temperature levels: Coarse-grained HAZ (1100°C and above), Fine-grained HAZ (875-1100°C), Intercritical HAZ (700-875°C), Subcritical HAZ (575-700°C) and the base metal is unaffected below 575°C. According to these five temperature levels the SS304 temperature-dependent yield stress of the modified thermal model is illustrated in Fig. 3.18a. Following the similar technique of determining yield stress described above, temperature-dependent tangent modulus of SS304 were also obtained as shown in Fig. 3.18b.

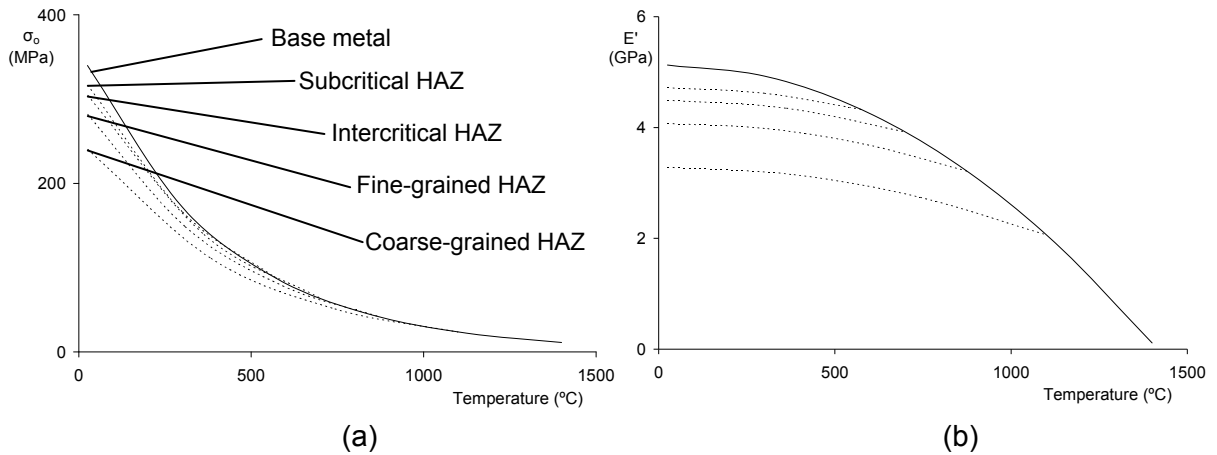


Fig. 3.18. Temperature-dependent yield stress and plastic modulus of SS304 for five temperature levels in modified thermal model: (a) yield stress evolution, (b) tangent modulus evolution.

RESIDUAL STRESS SIMULATION USING THE MODIFIED THERMAL MODEL

A thermal simulation and subsequent residual stress simulation using the modified thermal model were performed for SS304 socket welded piping joint using ANSYS. The 3D finite element mesh used is shown in Fig. 3.19. On residual stress simulation, five sets of mechanical material properties representing five temperature levels described above were assigned. Each set of material properties is temperature dependent. In ANSYS, the material set of an element can be assigned or changed by issuing command MPCHG. In the beginning of residual stress simulation, all of the elements are assigned with material set#1, which is for base metal. As the welding process progresses, each element's peak temperature would be updated by tracking temperature history from the results of thermal simulation. The updated peak temperatures at simulation steps determine the material set number assigned to the elements. The process of tracking temperature history and assigning material set are executed automatically by using ANSYS Parametric Design Language (APDL). An example of elements with material sets at various welding steps during residual stress simulation are shown in Fig. 3.20. In Fig. 3.20a, before the welding starts all the elements are represented by the base material set#1. In Fig. 3.20b, during the first tack weld, the updated material state around the tack weld based

on the peak temperature exposure is demonstrated. In Fig. 3.20c that after the final weld pass and cooling down to room temperature, the pipe metal outside 9mm from weld toe remains as the base metal (material set#1). Whereas, the material within 9mm of weld toe changes with distance from the weld toe.

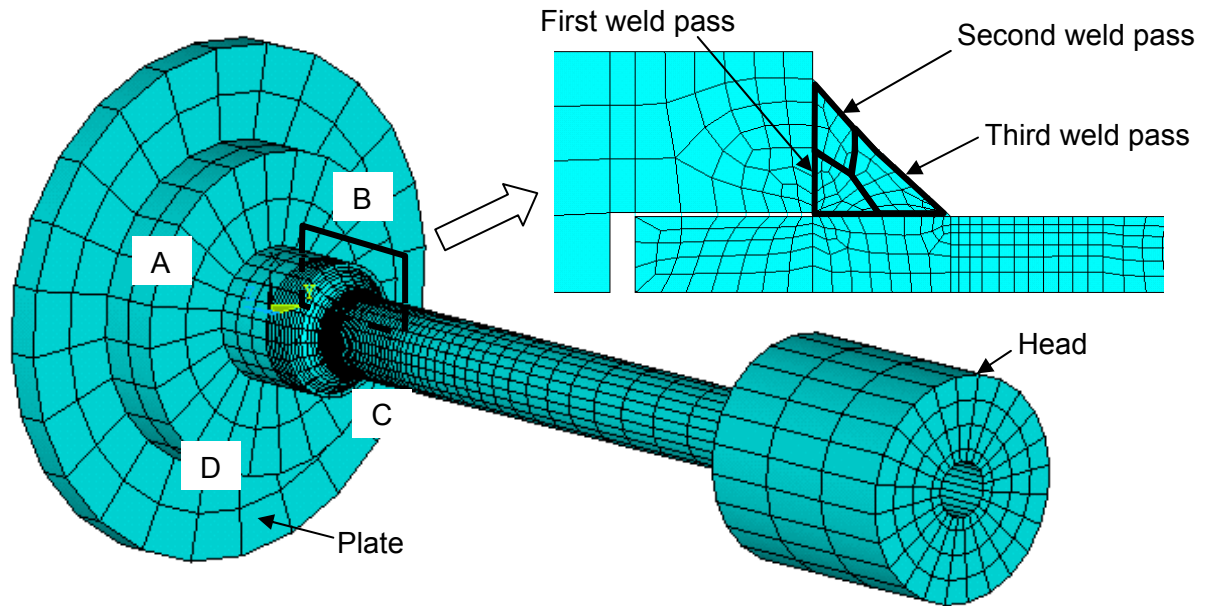


Fig. 3.19. Finite element mesh of the three-pass SS304 socket-welded piping joint

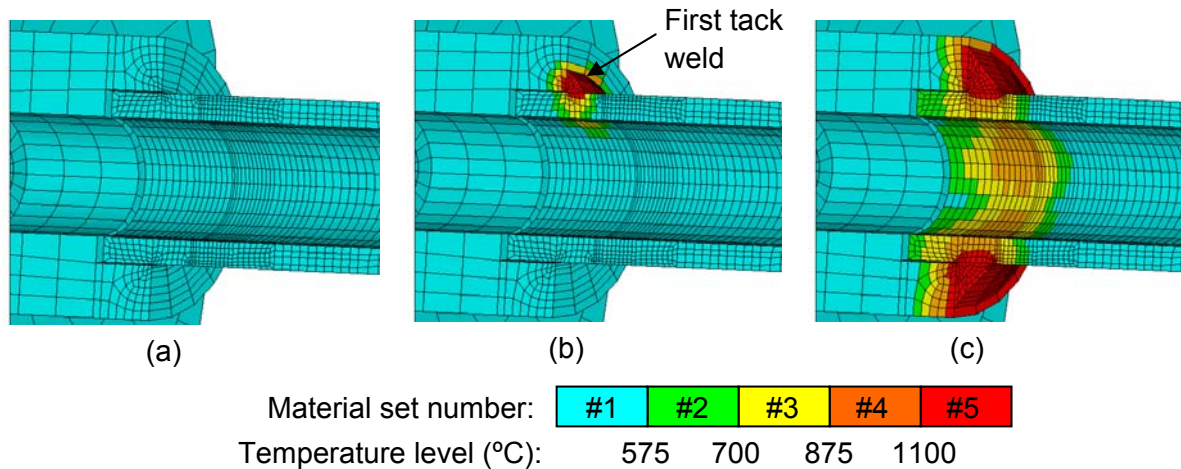


Fig. 3.20. Material state of elements near welding zone. Material sets assigned to elements depend on the peak temperature of the element before and after specific welding steps. (a) before weld starts, (b) after the first tack weld, and (c) after all weld passes are completed and the specimen reaches room temperature.

Initial residual stress data from x-ray and neutron diffraction measurements and finite element simulations using the original and modified thermal model are compared in Fig. 3.21. The data shown in Fig. 3.21 are at top of pipe outer surface (x-ray diffraction data) and 1mm depth from the surface (neutron diffraction data). The axial residual stress results from simulations using homogeneous material properties (basic thermal model) and using heterogeneous material properties (modified thermal model) are both plotted in this figure. The measured data at the surface (x-ray diffraction) and at 1 mm depth (neutron diffraction) show 100-300 MPa differences at various locations except the weld toe. Whereas, simulations from both the basic and modified models do not show much difference for surface and 1mm depth residual stresses. A possible reason that experimental data are different on the surface and at 1mm depth is the difference of measurement techniques. Surface measurements using x-ray diffraction technique is susceptible to surface condition and thus is not as accurate as neutron diffraction technique. The residual stress prediction by the modified thermal model is quite accurate near the weld toe, where the materials are heterogeneous because of the

welding. The basic thermal model overpredicted the residual stress at the weld toe by about 100 MPa. However, both model simulations compare well to the neutron diffraction data beyond 10mm from the weld toe. Hence, modeling of the heterogeneous material properties of the HAZ is essential to simulate the residual stress at weld toe accurately.

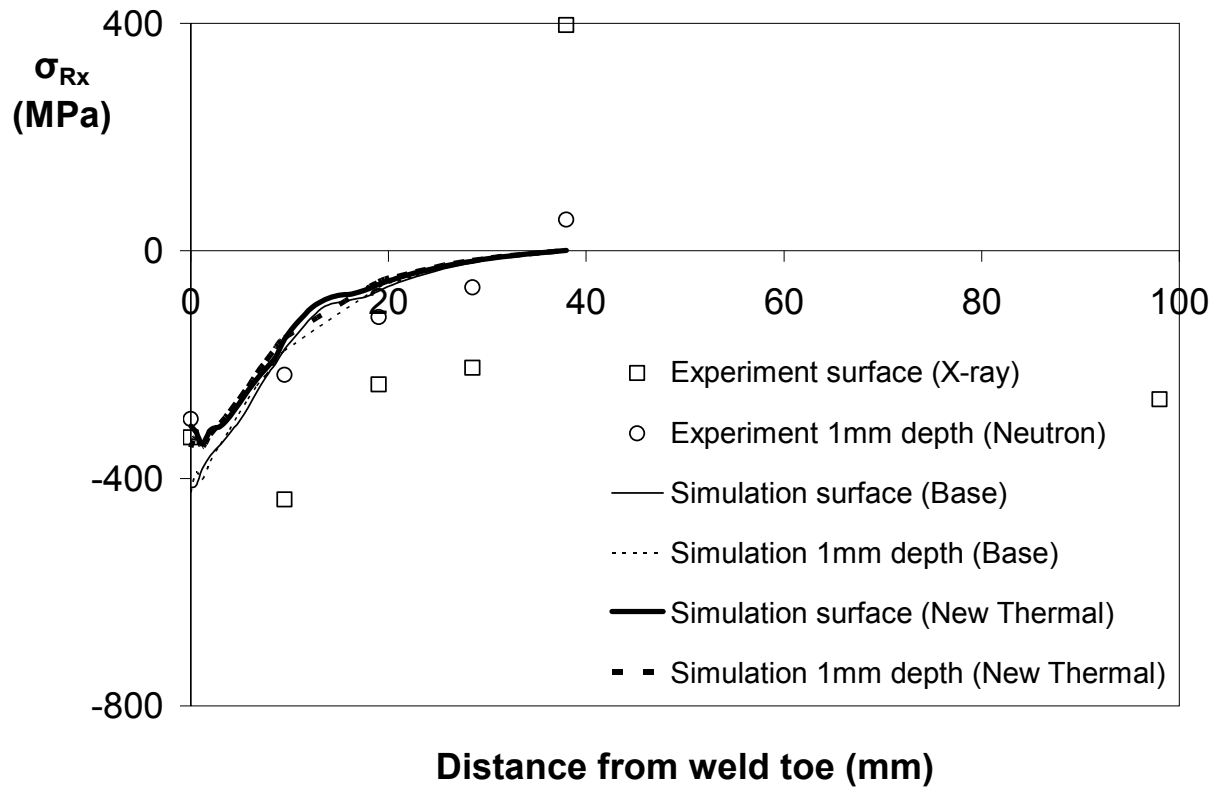


Fig. 3.21. Initial axial residual stresses from x-ray and neutron diffraction and finite element simulations.

EFFECT OF WELD SEQUENCE ON THE INITIAL RESIDUAL STRESS

A set of residual stress simulations was performed to study the influence of weld sequence and weld pass number on the initial residual stress. Four weld sequences were studied as shown in Table 3.2. The first three of these sequences yielded different fatigue lives as shown in Table 3.2. The weld sequence of these examples and their axial residual stress distribution results from simulations are illustrated in Figs. 3.22 to 3.25. For quarter sequence, quarter circumferential length of weld was laid at a time in the order indicated by 1-1, 1-2, ... until 3-4 (Sequence 1; Fig. 3.22) or until 4-4 (Sequence 2; Fig. 3.23). For full sequence, full circumferential length of weld was laid at a time in the order indicated by 1-1, 2-1,..4-1 (Sequence 3, Fig. 3.24 for same start-stop location) and (Sequence 4, Fig. 3.25 for different start-stop location). In 3D plots of axial residual stress distribution, angles of 0°, 90°, 180°, and 270° represents location A, B, C, and D, respectively (See Figs. 3.22 to 3.25).

Table 3.2. Weld sequences for initial residual stress simulation

Sequence Number	Type of weld sequence	Number of weld pass	fatigue life (cycles)
1	Quarter (Fig. 3.22)	3	680
2	Quarter (Fig. 3.23)	4	900
3	Full (Fig. 3.24; same start-stop)	4	470
4	Full (Fig. 3.25; different start-stop)	3	No Data

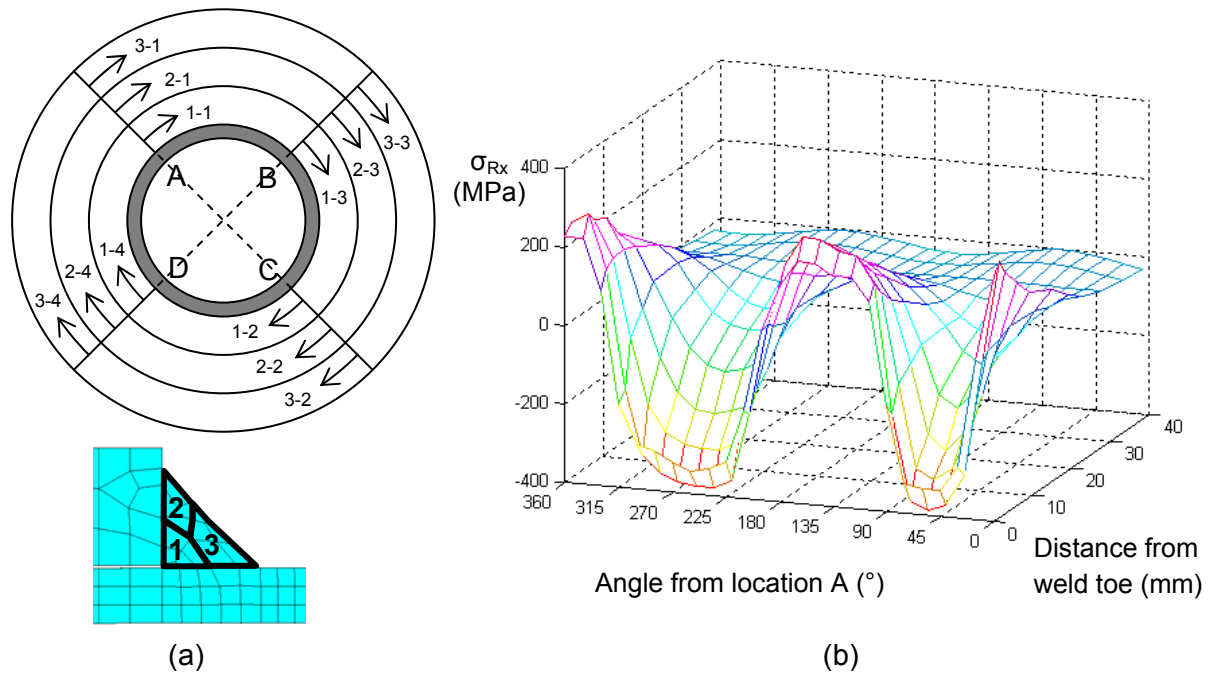


Fig. 3.22. (a) Three-pass quarter-weld sequence. (b) Simulation results of axial residual stress distribution along pipe outer surface from weld toe.

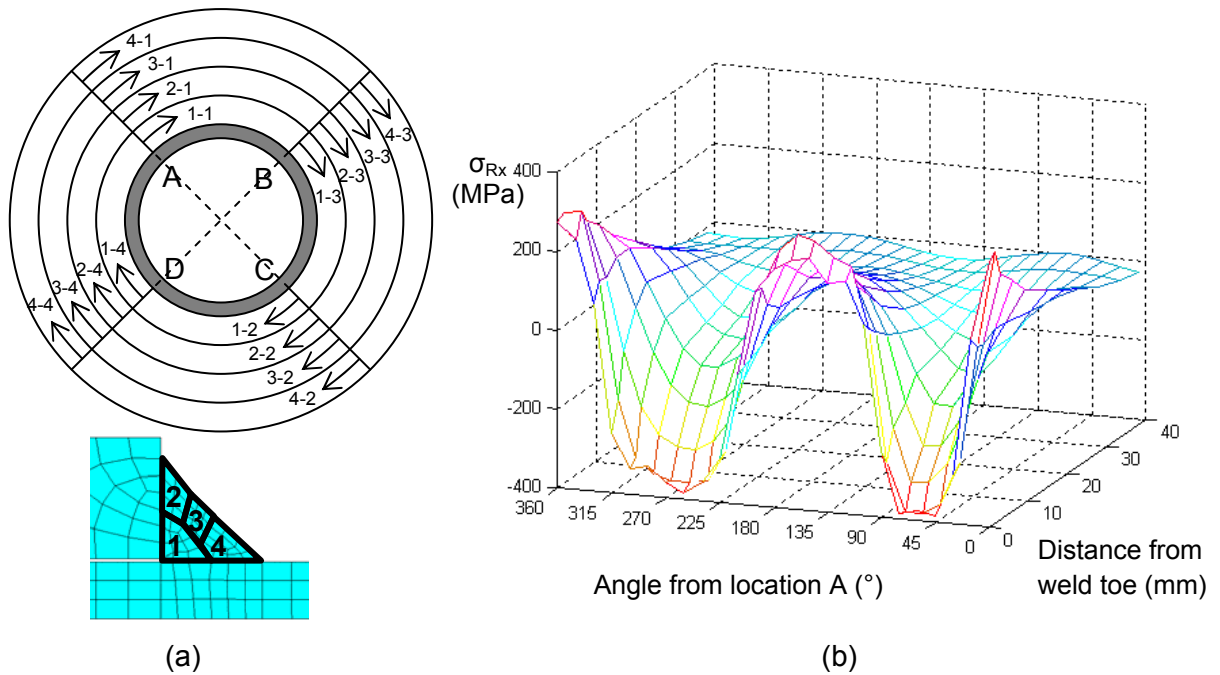


Fig. 3.23. (a) Four-pass, quarter-weld sequence. (b) Simulation results of axial residual stress distribution along pipe outer surface from weld toe.

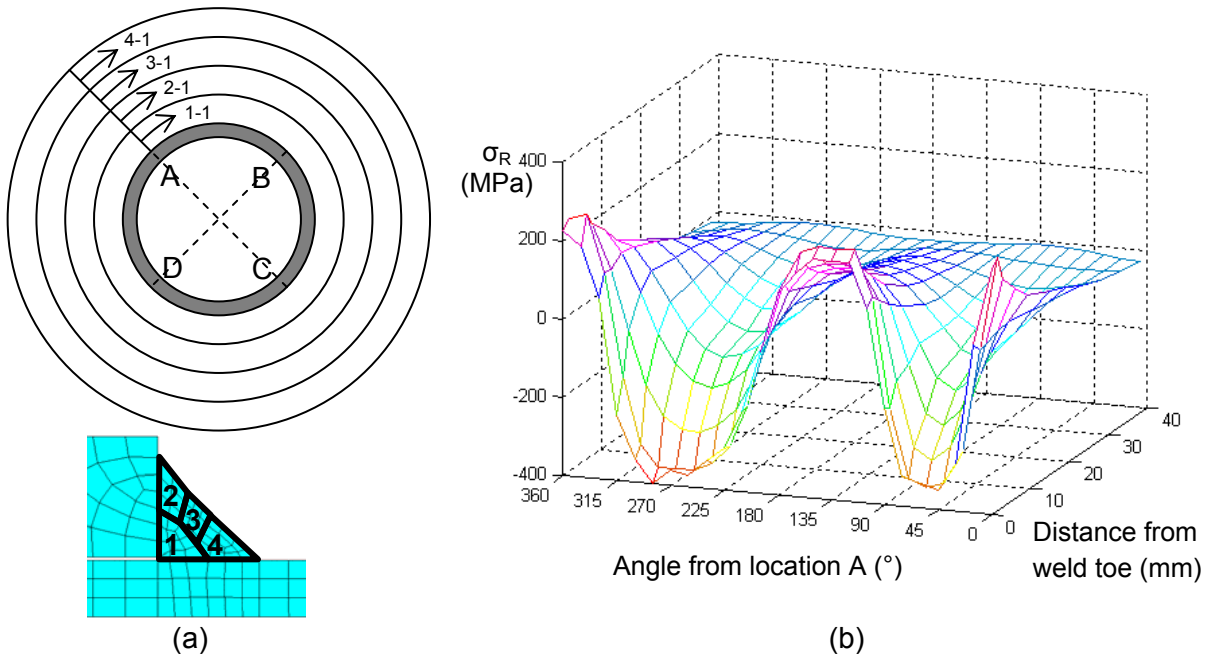


Fig. 3.24. (a) Four-pass, full-weld sequence (same start-stop location) (b) Simulation results of axial residual stress distribution along pipe outer surface from weld toe.

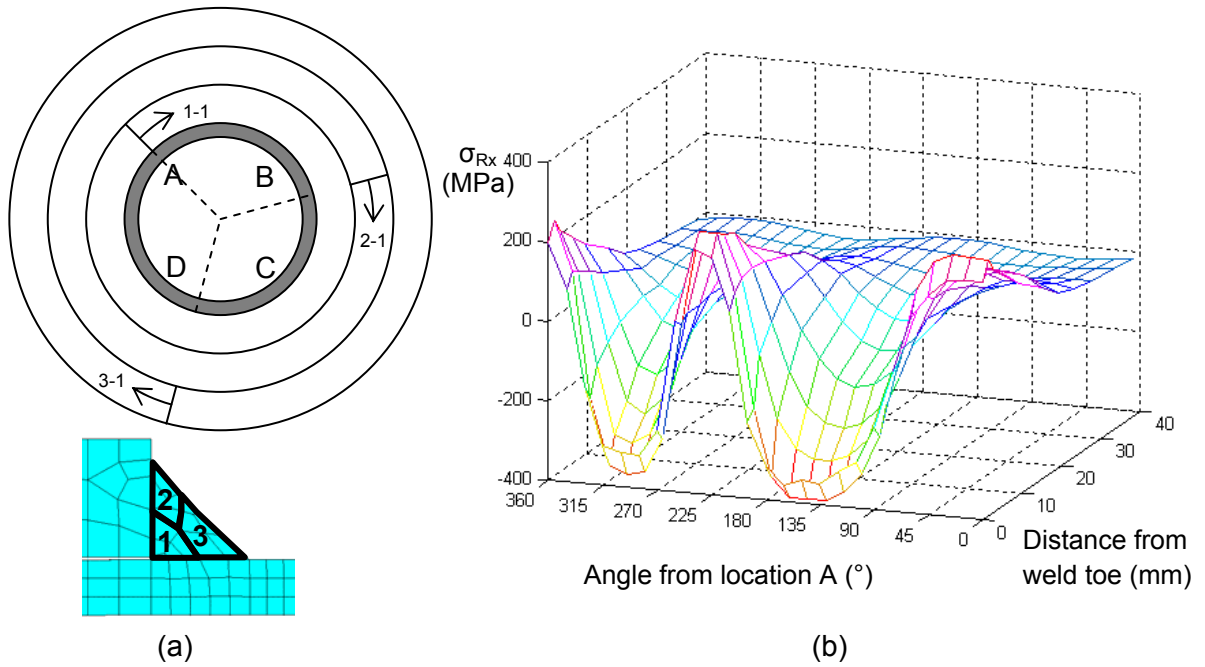


Fig. 3.25. (a) Four-pass, full-weld sequence (different start-stop locations). (b) Simulation results of axial residual stress distribution along pipe outer surface from weld toe.

By comparing the residual stress distributions in Figs. 3.22, 3.23, and 3.24, it is observed that their residual stress distributions are very similar. Residual stress magnitudes were large at weld toe and decreased with distance from weld toe. Maximum tensile residual stress was around 250 MPa near weld toes of location A and location C; maximum compressive residual stress was around -400 MPa near weld toes between A and B and between C and D. Since the residual stress distributions from these three examples were not much different, the difference of their fatigue lives (see Table 3.2) might not be related to initial residual stress induced by welding.

The main difference of Sequence 4 from other three sequences is the welding start-stop location is changed from one bead to the other. The first pass of sequence 4 started at location A, while the second and third passes started from 120° and 240° from A, respectively. This factor could be the reason that residual stress distribution in Fig. 3.25 showed different trend comparing to other sequences in Figs. 3.22-3.24. In sequence 4 maximum tensile residual stress was around 250 MPa near weld toes between A and B and between C and D; maximum compressive residual stress was around -400 MPa near weld toe at D and between A and B.

A possible reason that residual stress distributions for sequences 1, 2, and 3 are similar because of same start-stop location. For these three sequences welding in each pass started from location A and also the final pass ended at location A. As some research like Dong et al. [1997] assumed that the stresses that were induced prior to the final weld pass are relaxed by the temperature resulting from the final weld pass, the residual stresses in the sequences 1, 2, and 3 could be primarily determined by the final pass which for all sequences ended at location A. Thus the residual stress distributions were similar. On the other hand, the welding start-stop location of final pass in sequence 4 was not at location A, so its stress distribution is different.

CONCLUSIONS

A set of residual stress measurements on welded piping joints are presented. Welded piping joints with various material, weld design type, fatigue loading type, and number of cycles were measured using x-ray diffraction and neutron diffraction methods. Measured residual stresses on welded piping joints were plotted and compared, and following features were concluded.

1. Initial residual stresses on AB side at HAZ are compressive in all joints. Magnitude of residual stresses is large near weld toe and decreases with distance from weld toe as expected.
2. For stainless steel welded piping joints, the initial maximum compressive residual stress is higher than the yield stress of base metal; For carbon steel welded joints the initial maximum compressive residual stress does not exceed the yield stress of base metal.
3. For stainless steel piping joints, the axial residual stresses are relaxed significantly after 5 cycles and remains stationary during the following cycles. Axial residual stress in carbon steel welded joints relax slower with fatigue cycles compare to the stainless steel welded joints.
4. The initial residual stresses of stainless steel material are larger on outer surface and gradually decrease with depth from outer surface.

Numerical simulations of the initial residual stress of socket welded piping joints demonstrate dependence on the material heterogeneity at the heat affected zone (HAZ). The change in material properties at the HAZ due to high temperature cycle exposure was implemented in developing a modified thermal model that improved the residual stress simulation at the weld toe. Finally, the initial axial residual stress distributions were simulated for four weld sequences. Observations made from the simulations study are:

1. Material properties like yield stress (σ_0) and plastic modulus of bilinear fit (E') are changed due to high temperature cycles of welding. The parameters σ_0 and E' decreases as the peak exposure temperature during welding increases .
2. Since peak temperature during welding is different at different distacnes from the weld toe, the materials of the HAZ becomes heterogeneous.
3. The initial residual stress simulation using the basic thermal model is generally reasonable, but the prediction of the residual stress at the weld toe improved with the modified thermal model.
4. The initial residual stress distribution are mainly determined by the start-stop location of the final weld pass.

The experimental data indicated that residual stresses are relaxed largely within the first few loading cycles, and numerical simulation results demonstrated similar initial residual stress distribution for specimens with different weld sequence. Therefore, the different low-cycle fatigue life may not be related to the initial residual stresses.

ACKNOWLEDGEMENTS

All of the residual stress measurements were conducted at Oak Ridge National Laboratory (ORNL) through the user program of the High Temperature Materials Laboratory (HTML). The author would like to thank Dr. Camden R. Hubbard and Dr. Thomas R. Watkins for the help in scheduling, setting, and conducting residual stress measurements. The financial support from the NSF Grant #DMR-0408910, and the Center from Nuclear Power Plant Structures, Equipment and Piping

and Department of Civil, Construction and Environmental Engineering at North Carolina State University are gratefully acknowledged.

CHAPTER 4

Improved Numerical Scheme for Simulating Fatigue Responses of Small Bore Welded Piping Joints

ABSTRACT

The evaluation of premature fatigue failures in nuclear power plants revealed that the failures mostly occurred at weld joints. To understand the failure responses of welded joints under fatigue loading, numerical simulations have been used by the researchers. The numerical simulation of welded piping joints under fatigue loading basically can be performed into two main steps: the simulation of initial residual stresses and the simulation of fatigue responses. In previous researches the initial residual stresses can be simulated well, but the fatigue response simulations are not sufficient for understanding fatigue failure responses and hence improved simulation methods would be needed for better prediction of fatigue failure responses of welded joints. This study attempts to achieve the improvement by using various material properties with various material models and quarter-point element at the stress-concentration areas. The study of using various material properties and various material models involves fatigue tests on temperature-conditioned tubular coupons and subsequent material parameters determination. The simulation results revealed that the combination of the heterogeneous material properties and the Chaboche model can simulate the force and strain responses best and also simulate the residual stress relaxation well. Finally, the influence of initial welding residual stress on fatigue failure response of socket-weld joints is investigated. It is concluded that the ratcheting rate and strain amplitude near weld toe are both influenced significantly by the initial residual stresses.

INTRODUCTION

The evaluation of premature fatigue failures in nuclear power plants revealed that the failures mostly occurred at weld joints [Gosselin, 1994]. To understand the failure responses of welded joints under fatigue loading, numerical simulations have been used by the researchers [Barsoum, 2006; Lachmann et al., 2000, and Smith et al., 2001]. The numerical simulation of welded piping joints under fatigue loading basically can be performed into two main steps: the simulation of initial residual stresses and the simulation of fatigue responses. The simulation of residual stress requires modeling of welding process using finite element methods [Abid and Siddique, 2005; Jiang et al., 2005, and others]. The basic concept of simulating welding process is one of the sequentially uncoupled steps of welded joint fatigue response simulation, in which nonlinear, transient thermal analysis is conducted for calculating temperature history during welding. The computed temperature history is used as input in a subsequent thermo-mechanical analysis for residual stresses simulation. The residual stresses induced by welding process have been considered as an important factor that influences fatigue life of welded joints [Higuchi et al., 1998; Iida et al., 1997, and others]. Hence, in the subsequent fatigue response simulation, the initial residual stresses are prescribed to the finite element analysis as an initial condition. Strain response and residual stress relaxation under fatigue loading cycles are calculated from this step. The computed stress and strain responses are usually used for fatigue failure response analysis or determining fatigue lives of welded joints.

Previous studies on fatigue response simulation of welded joints [Lu, 2003; Barsoum, 2006] developed numerical scheme for three-dimensional finite element analysis of welded piping joints using ANSYS or ABAQUS commercial software package. Lu [2003] used a bilinear material model for both residual stress and subsequent fatigue response simulations. Lachmann et al. [2000] used a 2D finite element model with a multilinear material model for simulating fatigue response of a welded plate. Smith et al. [2001] also used the multilinear material model for fatigue response

simulation of a welded steel bar. The calculated strain and residual stress relaxation responses from these fatigue simulations only qualitatively agreed with the experimental responses. These simulation methods are not sufficient for understanding fatigue failure responses and hence improved simulation methods would be needed for better prediction of fatigue failure responses of welded joints.

One of the improvements that can be made is the use of heterogeneous material properties instead of homogeneous base metal material properties for the elements in the heat affected zone. Murugan et al. [1998] demonstrated that elevated temperature cycles during welding changes the microstructure of the heat affected zone metals. Johnson and Ramirez [SAC/BD-00/13] showed that after a single weld pass the base metal generally has five different microstructures induced by different temperature cycles. Lachmann et al. [2000] used four sets of material properties on various regions of a 2D model for fatigue response simulation.

Another improvement can be made is use of advanced material model. Bilinear and multilinear models that were used in the studies mentioned above have been shown not suitable for simulating ratcheting responses [Bari and Hassan, 2000; Rahman et al., 2008]. An option to make significant improvement could be the use of the Chaboche model with the four decomposed rule [Chaboche, 1991] available in ANSYS. The Chaboche model has been proven to simulate ratcheting and other cyclic response quite well [Chaboche, 1991; Bari and Hassan, 2000, 2002; Rahman et al., 2008 and others]. Another choice is using the recently developed modified Chaboche model [Krishna et al. 2009], which can simulate a broad set of cyclic and ratcheting responses. However, this model needs to be customized for ANSYS in order to use it for structural response simulations. Hence, this study will make use of the Chaboche model [1991] in ANSYS for improving the simulation of the welded piping joint fatigue responses.

Selection of elements and mesh could also have an effect on predicting strains and stresses of welded joints. The basic concept is to use finer mesh at critical areas, such as, at stress concentration areas of geometrical discontinuity and heat affected zone (HAZ) of temperature variations during welding. Lu [2001] determined mesh density based on the calculation of crack-tip equivalent plastic stress. Duranton et al. [2004] used an adaptive mesh generation and moving refinement procedure, which can refine mesh locally depending on the position and nature of the source (form, intensity, etc.). Besides the refinement, element selection at stress-concentration areas, such as quarter-point element [Shi et al., 1998] for weld toe and root, is important.

The main objective of this study is to improve the fatigue response simulations of welded piping joints. This objective is achieved by using heterogeneous material properties with Chaboche model and quarter-point element at the stress-concentration areas. This chapter first discusses each of these simulation improving features. Next, the new fatigue response simulation scheme that improves the simulation scheme of Lu [2003] and Chapter 2 are presented. The stainless steel SS304 socket welded piping joints used in the experimental study in Chapter 2 is illustrated in Fig. 4.1. An example of the finite element mesh composed of 8-node SOLID 185 elements used in the simulation is shown in Fig. 4.2. The strain and stress responses from new fatigue response simulation scheme will be compared to experimental responses from Chapter 2 and Chapter 3, in order to validate the modified simulation scheme.

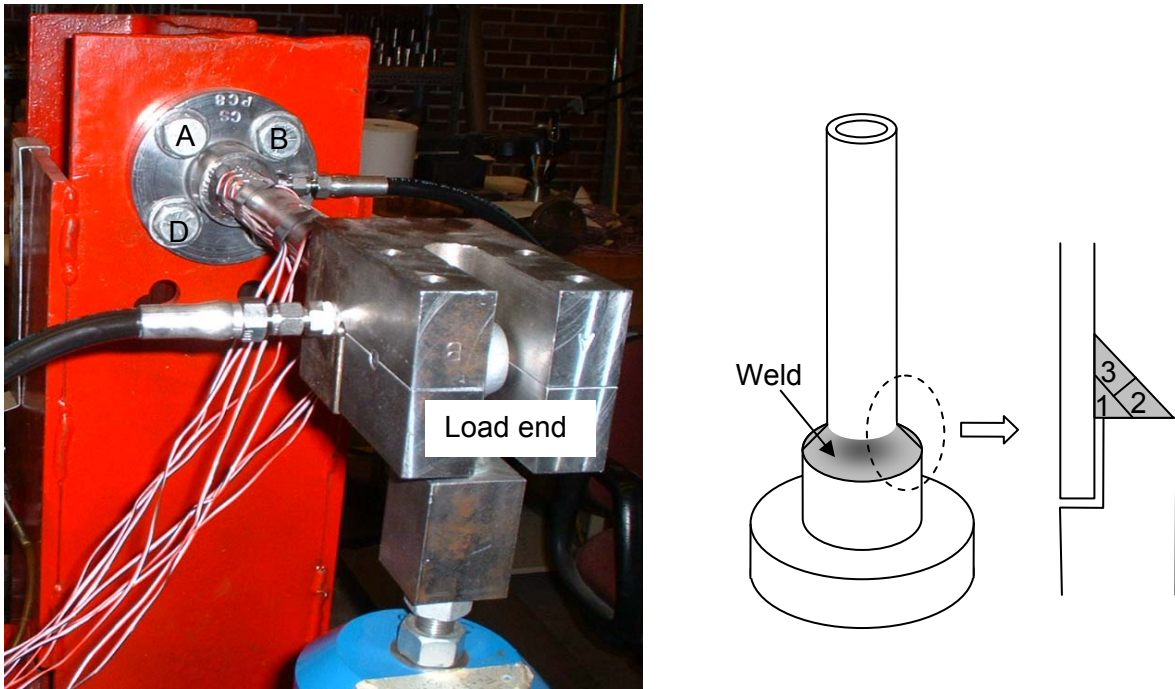


Fig. 4.1. Cantilever set-up for socket welded piping joint fatigue tests, and weld bead sequence of the specimen

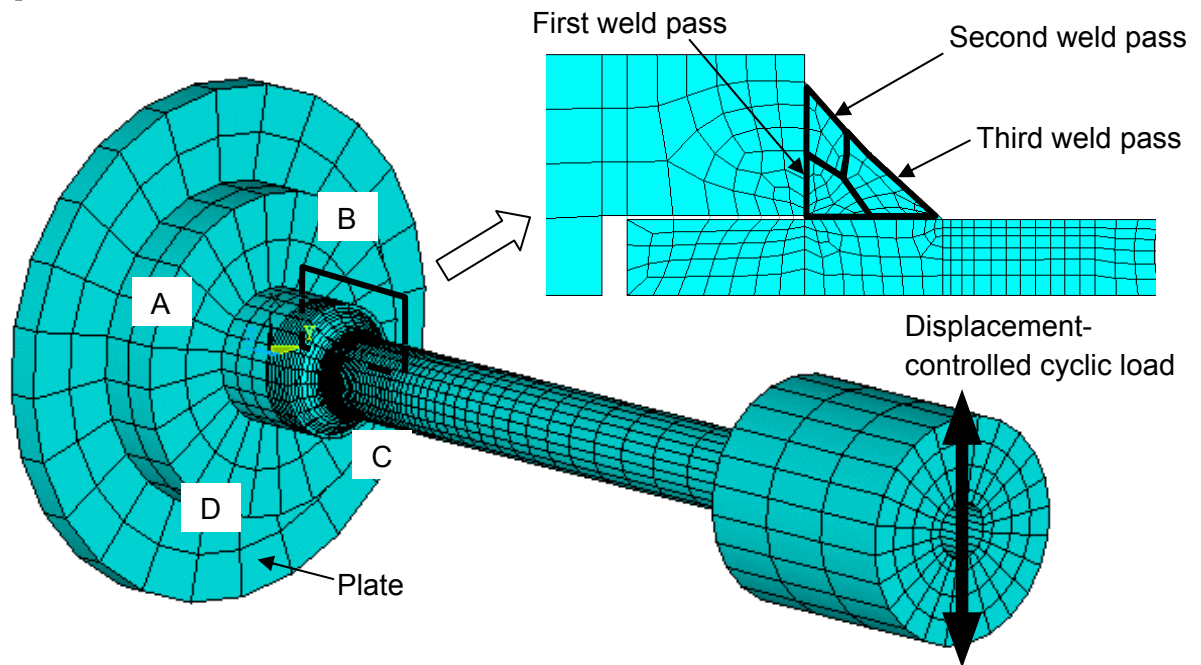


Fig. 4.2. Finite element mesh of the three-pass SS304 socket-welded piping joint. The elements used in generating the mesh are 8-node SOILD 185.

FATIGUE RESPONSE SIMULATION SCHEME

The fatigue response simulation scheme implemented three modifications: used heterogeneous material properties instead of the homogeneous base metal properties, use Chaboche model [1991] instead of the bilinear or multilinear model, and use quarter-point elements at weld toe and root. In the following sections the details of these features are discussed and their applications using ANSYS are presented.

HETEROGENEOUS MATERIAL PROPERTIES

In the previous fatigue response simulation [Lu, 2003] and Chapter 2, material properties of the welded specimen were assumed homogeneous base metal. The whole specimen was modeled using one set of material properties. In a welded joint, the material at the heat affected zone (HAZ) is heated rapidly to elevated temperatures when weld filler material is deposited and subsequently temperatures decrease slowly as welding ceases as illustrated in Fig. 4.3. As stated in the introduction, such temperature cycles may change microstructure of metals resulting in changed material properties compare to the initial base metal. The material property at different locations of the HAZ would be different depending on the highest temperature that a location was exposed to during welding. As the example shown in Fig. 4.3, the material properties at locations E, F, and G after the specimen cooled down to room temperature (at 8000 sec.) would change differently since these locations experience different peak temperatures during the welding process. Hence, at the completion of the welding process, the material property at the HAZ will be heterogeneous, which would influence the fatigue response simulation.

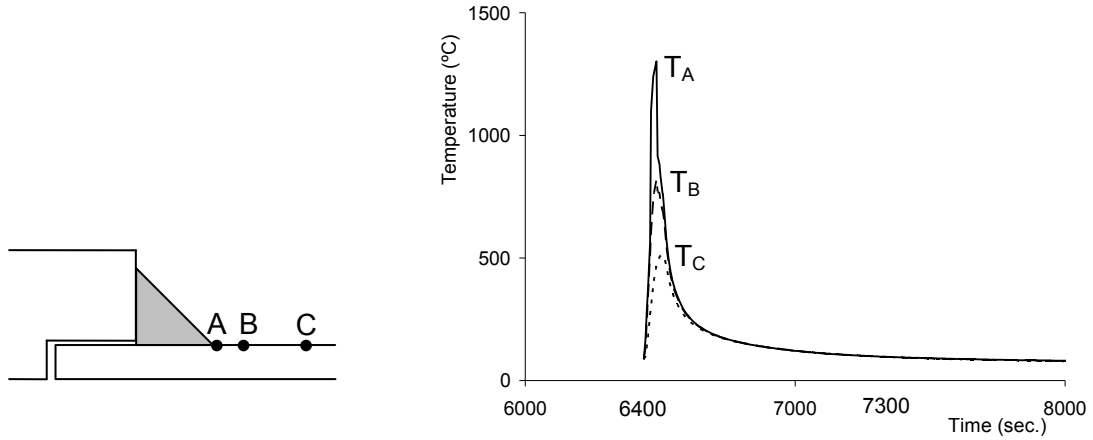


Fig. 4.3. Temperature history at various locations of the heat affected zone during a weld sequence.

To determine the heterogeneous material properties of the HAZ, cyclic loading tests on temperature-conditioned tubular specimens were conducted. This involves conditioning tubular specimens through quick heating to a specific peak temperature, followed by slow air cooling to room temperature before conducting various cyclic loading tests. Base metal coupons subjected to such temperature cycles are anticipated to simulate the HAZ material state. The procedure of temperature conditioning and types of loading tests are described in Chapter 3. Example of axial strain-controlled cyclic experiment responses is shown in Fig. 4.4. The stress-strain responses of five temperature conditioned coupons and one unconditioned base metal coupon from the first cycle are compared in Fig. 4.4a. Decrease in the yield and peak axial stresses, and hysteresis curve shapes with the increase in conditioning peak temperature are clearly observed in Fig. 4.4a. Axial stress amplitude from each cycle for the six strain-controlled experiments are calculated using: $\sigma_{xa} = \frac{\sigma_{\max} - \sigma_{\min}}{2}$ and plotted against the number of cycles N as shown in Fig. 4.4b that the base metal softens as the conditioning peak temperature increases. These results also demonstrate the heterogeneous material properties at the HAZ.

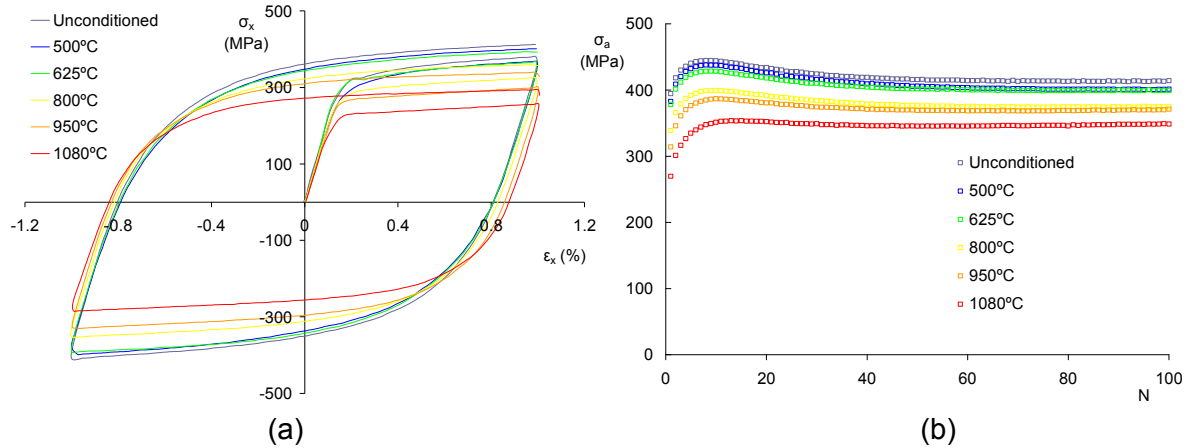


Fig. 4.4. Experimental results of conditioned and unconditioned stainless steel SS304 specimens from uniaxial strain-controlled experiments. The temperatures shown in the figure are the specimen conditioning peak temperatures. (a) Axial stress-strain responses from the first cycle. (b) Amplitudes of axial stress peaks from each cycle versus the number of cycles.

Biaxial ratcheting experimental were conducted on four conditioned and one unconditioned coupons. These experiments were conducted by prescribing a steady internal pressure of 1 ksi and 0.4% axial strain-controlled cycles as shown in Fig. 4.5a. Circumferential strain ratcheting driven by the steady internal pressure is obtained from this experiment. Mean circumferential strain in each cycle calculated using: $\epsilon_{\theta m} = \frac{\epsilon_{\max} + \epsilon_{\min}}{2}$ is plotted against the number of cycles N as shown in Fig.

4.5b. The results in Fig. 4.5b shows the trend of higher circumferential strain ratcheting rate from coupons conditioned under higher peak temperature. Again, it is demonstrated that the amount of softening of the base metal depends on the peak conditioning temperature.

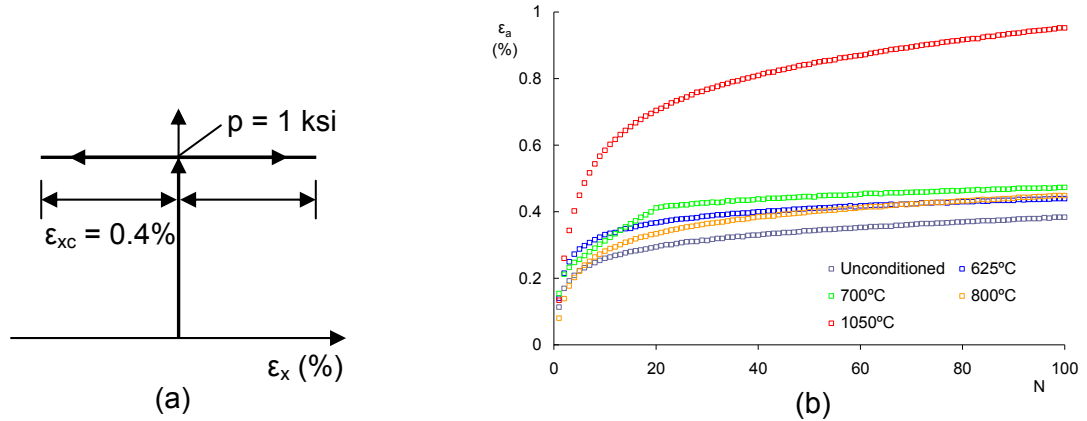


Fig. 4.5. Biaxial ratcheting experiments on conditioned and unconditioned stainless steel SS304 coupons. (a) Loading path prescribed. (b) Means of circumferential strain from each cycle versus the number of cycles.

The third type experiment conducted prescribed axial, unsymmetrical force-controlled cycles as shown in Fig. 4.6. As the temperature-conditioned coupons have different yield stresses, the mean and amplitude of the prescribed force-controlled cycles were determined based on the first cycle, negative peak force from the 1% strain-controlled cycle shown in Fig. 4.4a. The amplitudes were set to 80% of the 1st negative peak force and mean the remaining 20%. An example of axial stress-strain response from this type of experiment for a coupon conditioned by peak temperature of 1050°C is shown in Fig. 4.7a. The positive axial mean force (positive axial mean stress) is inducing axial strain ratcheting in the tensile direction as demonstrated by the gradual shift of the hysteresis loops. Mean and amplitude of axial strain response from each cycle calculated using:

$$\varepsilon_{xm} = \frac{\varepsilon_{\max} + \varepsilon_{\min}}{2} \text{ and } \varepsilon_{xa} = \frac{\varepsilon_{\max} - \varepsilon_{\min}}{2}$$

axial force-controlled cyclic experimental results from other specimens are not compared in Fig. 4.7b because the prescribed cyclic loading parameters on each coupon are different. The responses from the experiments under axial strain-controlled cycles, axial strain-controlled cycles under steady

internal pressure and axial force-controlled cycles are used to calibrate the Chaboche model parameters as presented later.

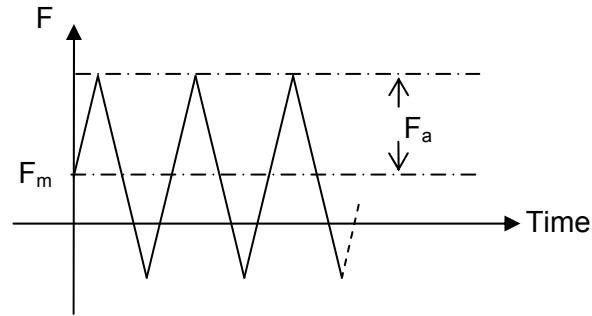


Fig. 4.6. Axial, force-controlled loading cycles prescribed in the uniaxial ratcheting experiments.

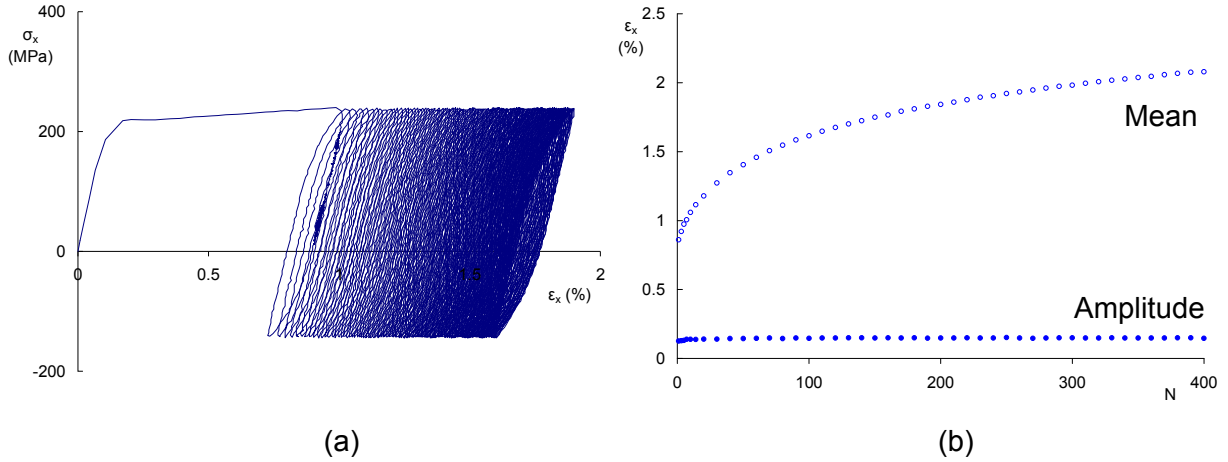


Fig. 4.7. Axial force-controlled experimental results of 1050°C-conditioned SS304 coupon, (a) axial stress-strain responses. (b) Mean and amplitude of axial strain from each cycle versus the number of cycles.

CHABOCHE MODEL PARAMETERS DETERMINATION

To improve the low-cycle fatigue response simulation, the Chaboche model with four decomposed hardening rule [Chaboche, 1991] combined with the Voce hardening law [Voce, 1955] in ANSYS was used. The Chaboche model parameters were determined by using the experimental

responses from the temperature-conditioned and unconditioned coupons discussed above. As the cyclic response simulation of the welded piping joint is of interest, the Chaboche model parameters were determined using the cyclic responses, rather than the monotonic responses of the materials. The elastic parameters E , ν , σ_o were determined from the 1st hysteresis curve, plotted in Fig. 4.4a. The Chaboche kinematic hardening rule parameters C_i ($i = 1$ to 4) and γ_i ($i = 1, 2,$ and 4) were determined from the 1st hysteresis curve in Fig. 4.4a, while the γ_3 is determined by fitting the axial strain ratcheting rate as shown in Fig. 4.7b. A systematic approach for determining C_i and γ_i is presented in Bari and Hassan [2000]. Cyclic hardening response is determined by the Voce hardening model, whose parameters R_∞ and b were determined from axial stress amplitude responses in Fig. 4.4b. The parameters for the Chaboche model and Voce hardening model in ANSYS determined for conditioned and unconditioned SS304 coupons are listed in Table 4.1. The fit of the 1% axial, strain-controlled cyclic responses from conditioned and unconditioned coupons using the parameters listed in Table 4.1 are shown in Fig. 4.8.

Table 4.1. Chaboche model and Voce hardening model parameters of temperature conditioned and unconditioned SS304.

Peak conditioning temperature (°C)	E (GPa)	ν	σ_o (MPa)	C_1 (MPa)	C_2 (MPa)	C_3 (MPa)	C_4 (MPa)
25	210	0.31	240	205003	73501	38506	2562
625	210	0.29	230	165167	68014	42312	2555
800	210	0.22	185	166050	55473	35759	2430
1050	210	0.32	152	145600	51499	35122	2358

Peak conditioning temperature (°C)	γ_1	γ_2	γ_3	γ_4	R_∞ (MPa)	b
25	5824	1985	341	1.10	26	120
625	7569	2349	358	1.10	32	120
800	7441	2241	348	4.17	34	120
1050	8340	9717	418	5.23	36	120

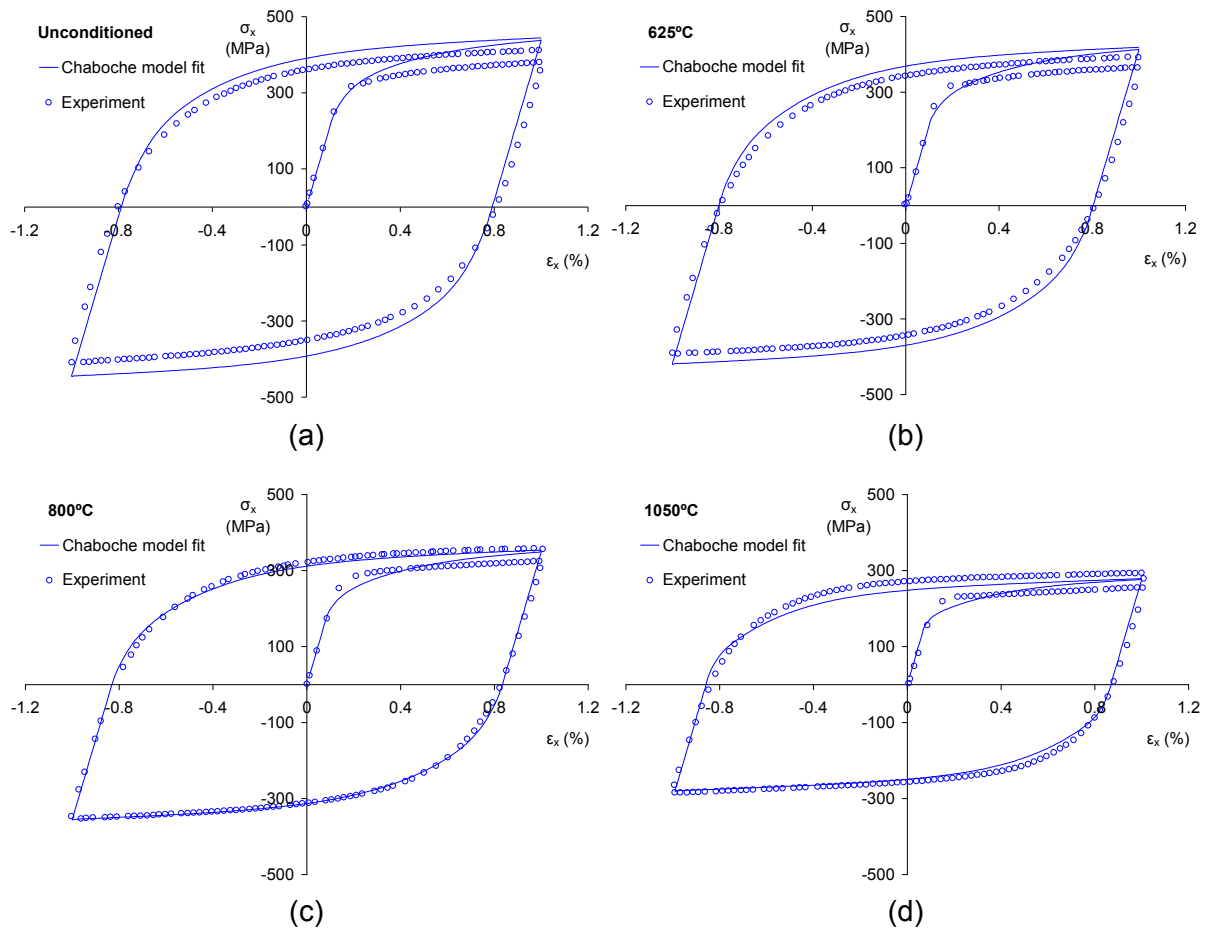


Fig. 4.8. Axial stress-strain responses of unconditioned base metal and temperature-conditioned coupons from uniaxial strain-controlled experiments and fit for Chaboche model parameter determination.

For the stainless steel SS304, Johnson and Ramirez [SAC/BD-00/13] showed that after a single weld pass the base metal generally has five different microstructures depending on the temperature levels: Coarse-grained HAZ (1100°C and above), Fine-grained HAZ (875-1100 °C), Intercritical HAZ (700-875 °C), Subcritical HAZ (575-700 °C) and the base metal is unaffected below 575 °C.

According to these temperature levels five sets of material properties were employed on fatigue simulation. The Chaboche model parameters of these five material sets, determined by linear interpolation of the parameters in Table 4.1, are listed in Table 4.2.

Table 4.2. Chaboche model and Voce hardening model parameters of five material sets for fatigue simulation.

Material set	Temperature range (°C)	E (GPa)	ν	σ_o (MPa)	C_1 (MPa)	C_2 (MPa)	C_3 (MPa)	C_4 (MPa)
1	~575	210	0.30	235	185085	70758	40410	2559
2	575~700	210	0.29	230	165167	68014	42313	2556
3	700~875	210	0.22	185	166050	55473	35760	2430
4	875~1100	210	0.29	160	150713	52492	35282	2376
5	1100~	210	0.32	124	122500	49000	35000	2400

Material set	γ_1	γ_2	γ_3	γ_4	R_∞ (MPa)	b
1	6697	2167	349	1.10	29.0	120
2	7569	2349	358	1.10	32.0	120
3	7441	2241	348	4.17	34.0	120
4	8115	7848	400	4.97	35.5	120
5	9400	12000	500	6.00	38.0	120

TECHNIQUE OF INCORPORATING MATERIAL HETEROGENEITY IN ANSYS

The technique of incorporating heterogeneous material into ANSYS computation involves assigning a specified material set to an element based on the peak temperature experienced by the element during welding. The peak temperature of each element was obtained from the thermal simulation (see Chapter 3). By using the ANSYS Parametric Design Language (APDL), each elements of the welded joint mesh can be assigned a material set based on its peak temperature automatically by issuing the command MPCHG. An example of elements with various material sets near weld for fatigue response simulation is shown in Fig. 4.9. The material set number 1 thru 5 in Fig. 4.9 are the ones shown in Table 4.2, and material set number 6 is for weld metal determined sperately from experiments of welding metals SS308.

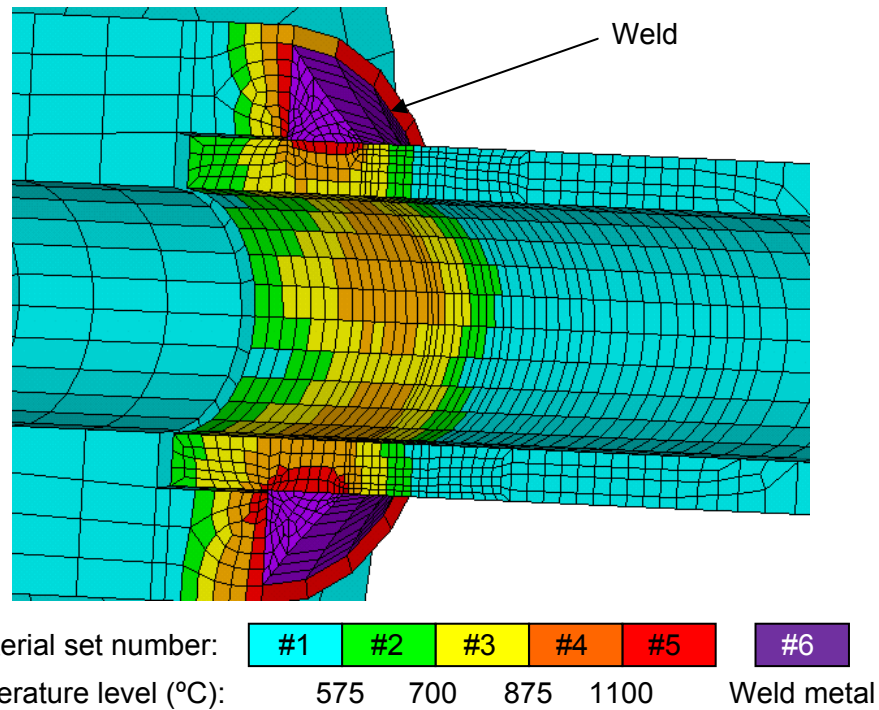


Fig. 4.9. Material sets assigned to elements for fatigue response simulation.

The fatigue response simulation should start in the presence of the initial welding residual stress. However, initial residual stresses were calculated using the bilinear material model in ANSYS. Change of the material model from bilinear model to Chaboche model for fatigue response simulation is not allowed by ANSYS because of compatibility reasons. Hence, to perform the fatigue response simulation with the Chaboche model in ANSYS, first the residual stress field was assigned as input. This requires that the finite element mesh for residual stress and fatigue response simulations has to be the same. The initial welding residual stresses was prescribed to the fatigue response simulation mesh by issuing the command INISTATE, which reads the stress values from results of residual stress simulation.

QUARTER-POINT ELEMENTS AT WELD TOE AND CONVERGENCE STUDY

To optimize the mesh density, the convergence study was performed with three mesh densities. The profiles of these meshes are shown in Fig. 4.10. The convergence study was performed by prescribing displacement-controlled loading at the load end as shown in Fig. 4.2. The calculated axial strain nodal responses on pipe top outer surface near weld toe for the three meshes are compared in Fig. 4.11. It can be observed in Fig. 4.11 that nodal strain response at weld toe is not converging. It is also interesting to observe that the maximum strain is not occurring at the weld toe as expected. Also, the non-convergence is observed only at the very 1st element at the weld toe. The strain responses from the three meshes from the elements outside the very 1st element at the weld toe are not much different from each other. This convergence problem at the weld toe is anticipated to be related to the geometrical discontinuity and related stress concentration. The eight-node hexahedral element SOLID185 even with the smallest Mesh C could not reproduce the strain profile at the weld toe.

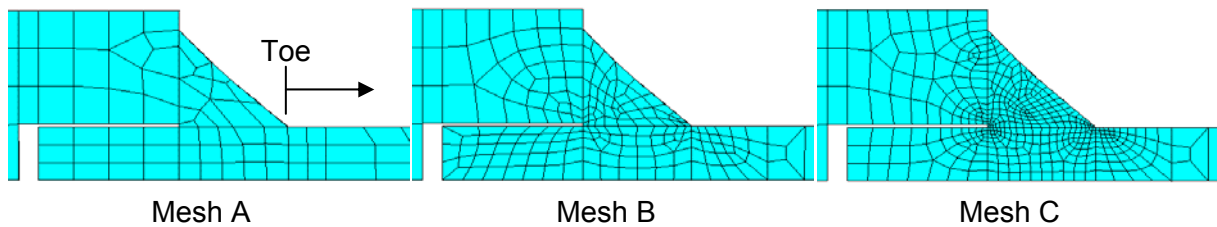


Fig. 4.10. Profile of various 3D mesh densities near weld for convergence study

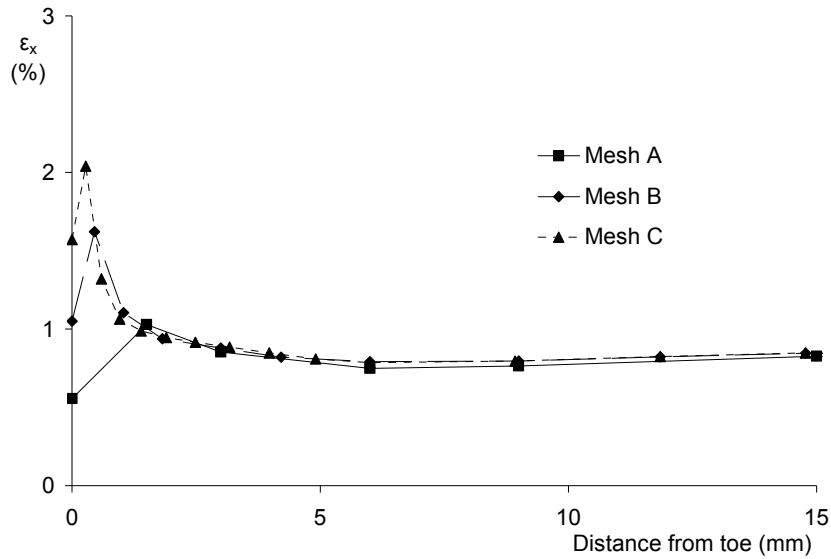


Fig. 4.11. Numerical simulations of axial strain response at weld toe under a displacement-controlled load from three mesh models. All of the elements are eight-noded SOLID185 elements.

Shi et al. [1998] demonstrated that stress concentration around the crack tip could be computed by moving the mid-side nodes to the quarter points towards the crack tip. Quarter-point element (also called *singular element*) is evaluated in representing the stress concentration at the weld toe. The 8-node SOLID 185 elements around weld toe were replaced by twenty-node SOLID186 *singular elements* as shown in Figs. 4.12a and 4.12b. Note the quarter-point nodes on the SOLID186 element sides connected to the weld toe. The transition from twenty-node SOLID186 to eight-node SOLID185 is achieved through the *connecting elements* as shown in Fig. 4.12b. The mid-side nodes of the common sides between the *connecting* and SOLID185 elements are removed.

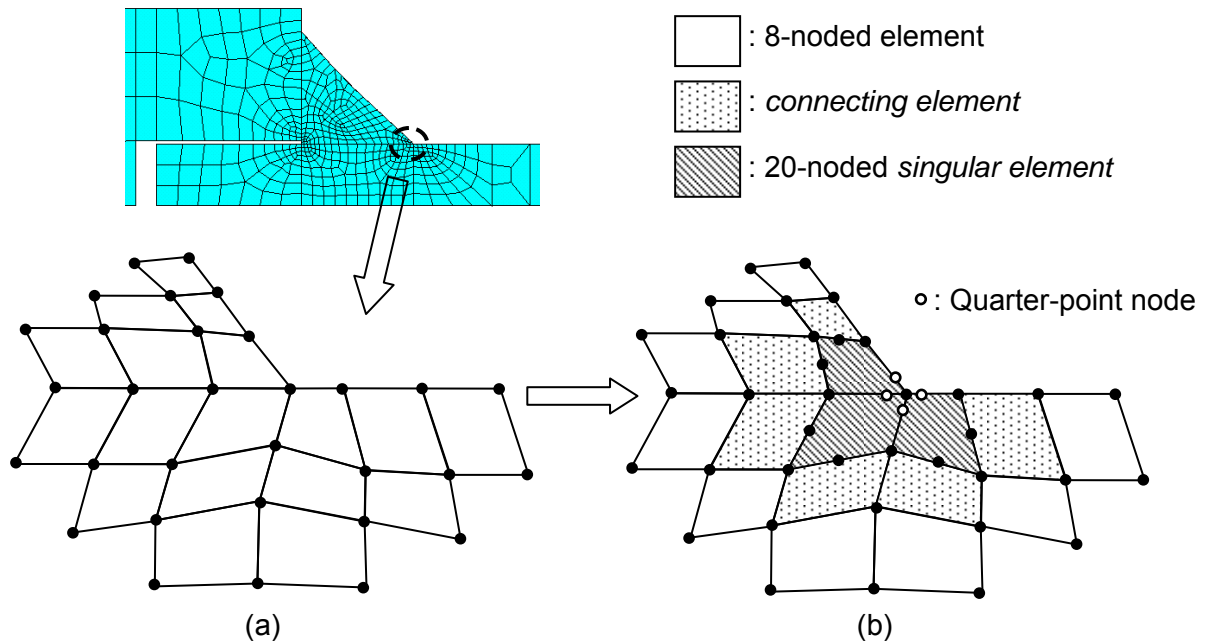


Fig. 4.12. Eight-node SOLID185 elements around weld toe are replaced by twenty-node SOLID186 elements for representing the stress-concentration at the weld toe. (a) initial mesh around weld toe composed of SOLID185 elements, (b) modified mesh around weld toe composed of twenty-node SOLID186, connecting and eight-node elements.

The strain profiles under displacement-controlled loading from the three modified meshes which include singular elements at the weld toe are compared in Fig. 4.13. It is observed in this figure that the axial strain profiles from Meshes B and C matches really well. Also, the maximum strain from all the meshes is occurring at the weld toe. The results in Fig. 4.13 also show that the Mesh B is fine enough for fatigue response simulation of the socket welded joints.

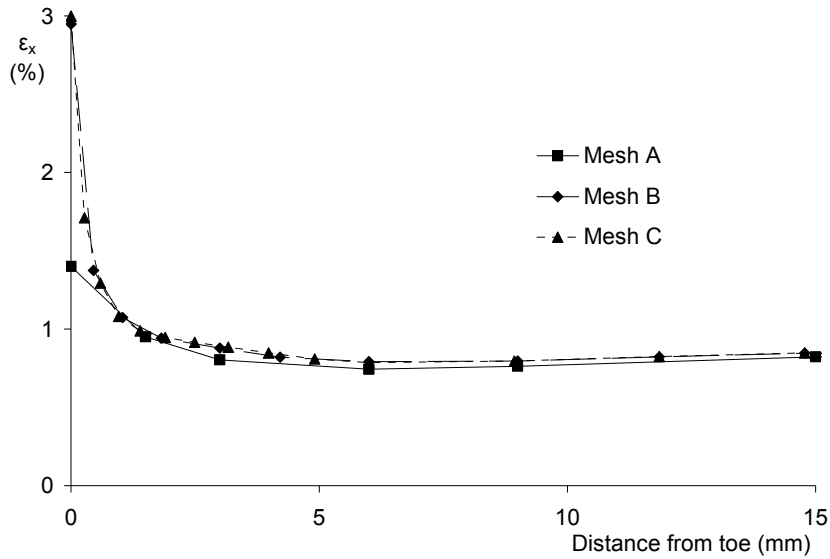


Fig. 4.13. Numerical simulations of axial strain response at weld toe under a displacement-controlled load from three modified mesh models with singular elements (SOLID186) at the weld toe.

FATIGUE RESPONSE SIMULATIONS FOR SOCKET WELDED JOINTS

INFLUENCE OF MATERIAL TYPES AND MATERIAL MODELS

Fatigue response simulations for three-pass quarter-sequence SS304 socket-welded piping joint were performed by prescribing displacement-controlled cyclic loading (amplitude, $\delta_c = 14.5$ mm). Four simulations using various combinations of material types (homogeneous and heterogeneous materials) and material models (bilinear model and Chaboche model) were performed. The simulation results are plotted and compared to the experimental responses in Figs. 4.14, 4.15, and 4.16. Load responses and strain responses were recorded every 0.03 seconds. Experimental data of the test were presented and discussed in Chapter 2. The simulation with the heterogeneous material properties and Chaboche model was performed for 100 cycles, while all other simulations were performed for 20 cycles.

The force-displacement simulations in the 1st cycle are compared to corresponding experimental response in Fig. 4.14. The Chaboche model simulates the 1st cycle force-displacement loop quite well

(Figs. 4.14c and 4.14d). The bilinear model overpredicts at the yield load significantly (Figs. 4.14a and 4.14b). The use of the heterogeneous material over the homogeneous material does not change the force-displacement simulation much.

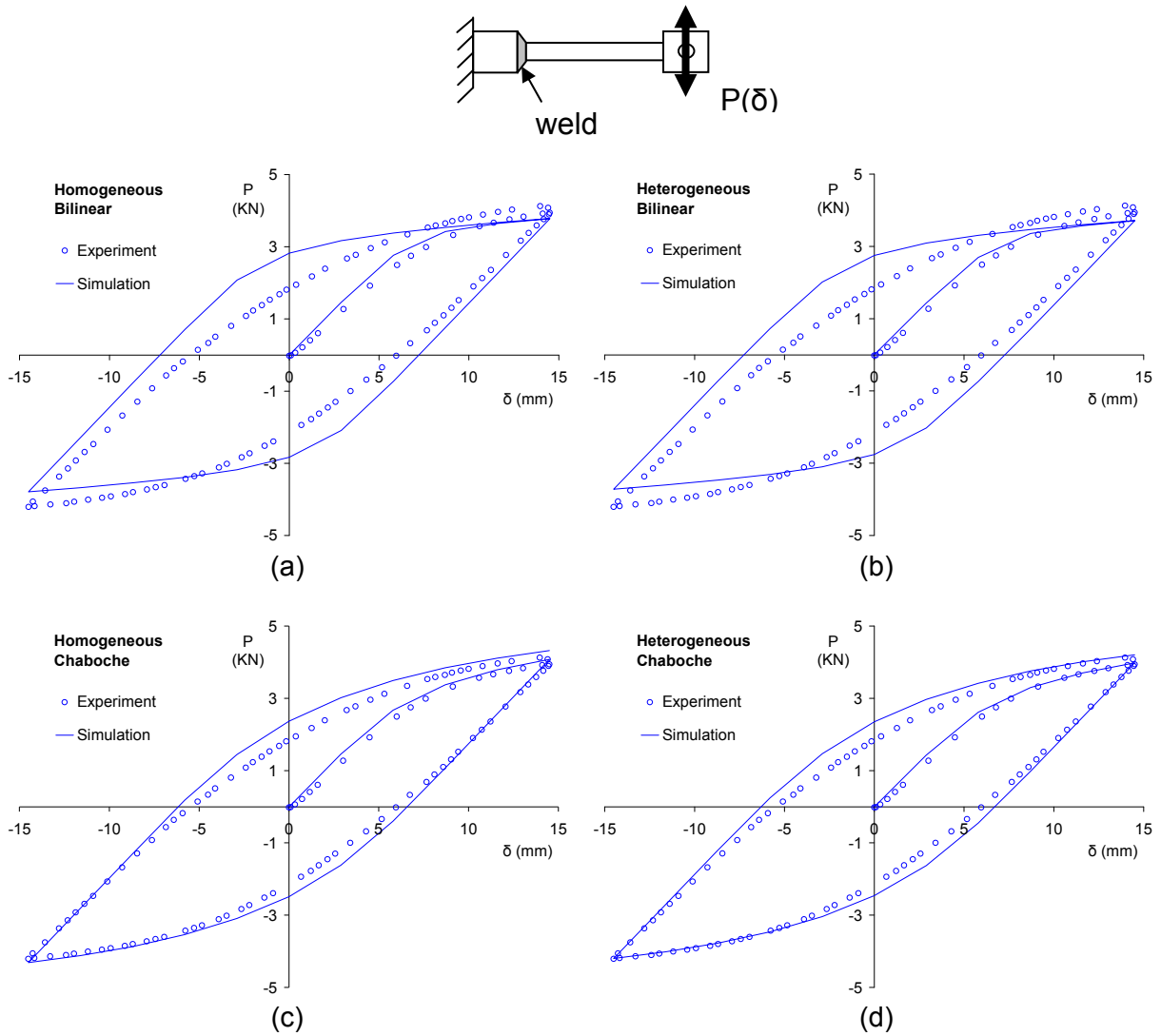


Fig. 4.14. Force-displacement responses from experiment and simulations using various material types and models. (a) Homogeneous and bilinear (b) Heterogeneous and bilinear (c) Homogeneous and Chaboche (d) Heterogeneous and Chaboche

Mean and amplitude force responses from each cycle are calculated using: $P_m = \frac{P_{\max} + P_{\min}}{2}$

and $P_c = \frac{P_{\max} - P_{\min}}{2}$, respectively, and are plotted against the number of cycles in Fig. 4.15. Mean

forces are simulated quite well with either model or material type, but the force amplitudes are simulated best by the Chaboche model with heterogeneous material. This combination of material model and type simulates the force amplitude exactly during the first five cycles as shown in Fig. 4.15d, but failed to simulate the subsequent cyclic softening.

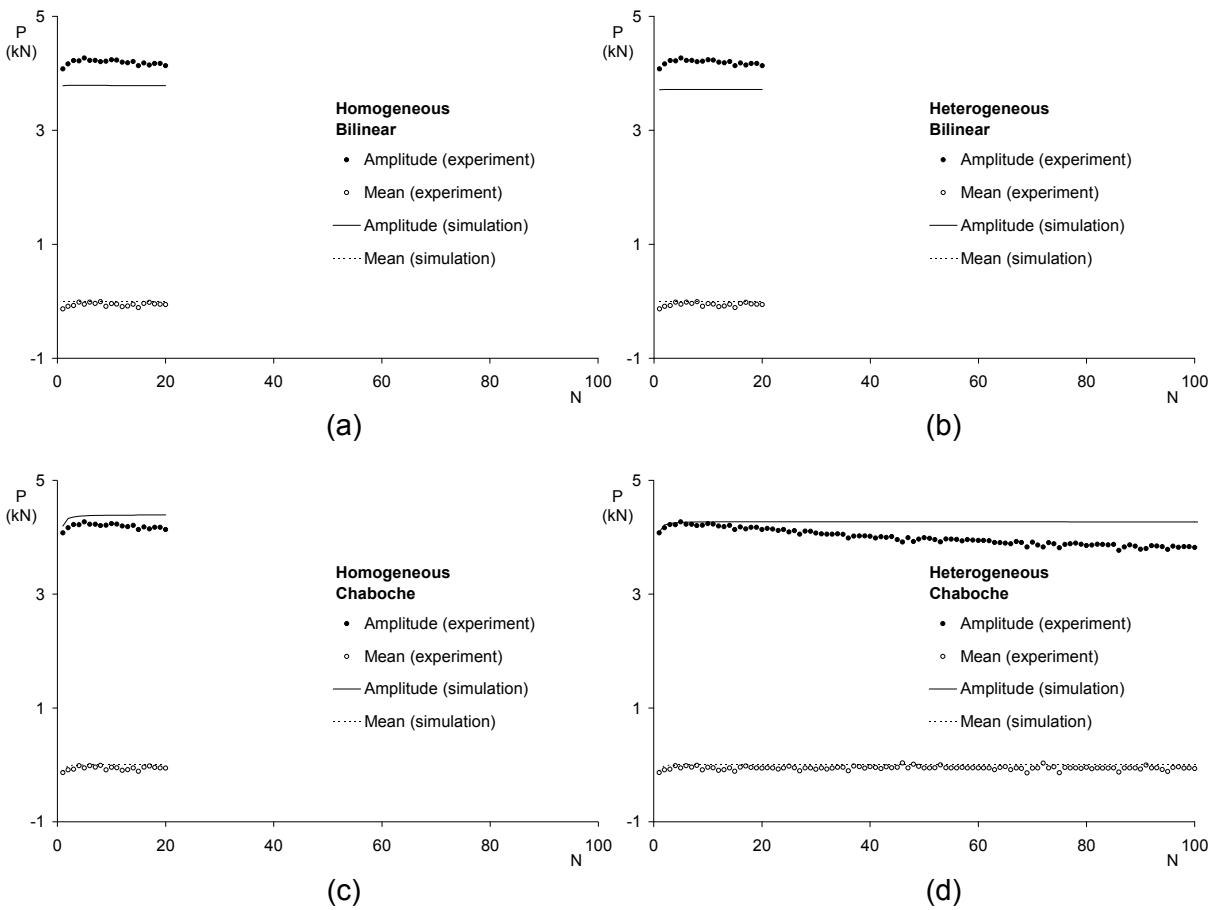


Fig. 4.15. Load response versus number of cycles from experiment and simulations using various material types and material models.

It was demonstrated in Fig. 4.4 that the SS304 pipe material cyclically hardens during the initial few cycles followed by cyclic softening. There is no material model available to the knowledge of the author that can simulate initial cyclic hardening and subsequent cyclic softening. The Voce hardening model in ANSYS was calibrated for simulating initial cyclic hardening followed by cyclic stabilization. This explains the force amplitude simulation in Fig. 4.15d, which shows initial cyclic hardening followed by cyclic stabilization, and hence the overprediction of the experimental force amplitudes during the later cycles. It is interesting to observe that the use of the homogeneous base metal increases the force amplitude simulation (Compare Fig. 4.15c to 4.15d and Fig. 4.15a to 4.15b).

Axial strain amplitude and mean simulations on the top pipe surface at 5 mm from the weld toe are compared to experimental responses in Fig. 4.16. All four simulations overpredicted the strain amplitudes, though the Chaboche model performance is the best in strain amplitude simulation. With the Chaboche model, the strain amplitude overprediction increases as the material type is changed from homogeneous to heterogeneous. However, the axial strain ratcheting rate (rate of change of mean strain per cycle) is simulated best by the Chaboche model with the heterogeneous material.

In conclusion, the Chaboche model in combination with the Voce hardening model can simulate the force-displacement and axial strain responses better than the bilinear model for the welded piping joints. Use of the heterogeneous material properties at the HAZ can slightly improve ratcheting response prediction than use of the homogeneous material properties. The reasons for strain amplitude overprediction need further investigation.

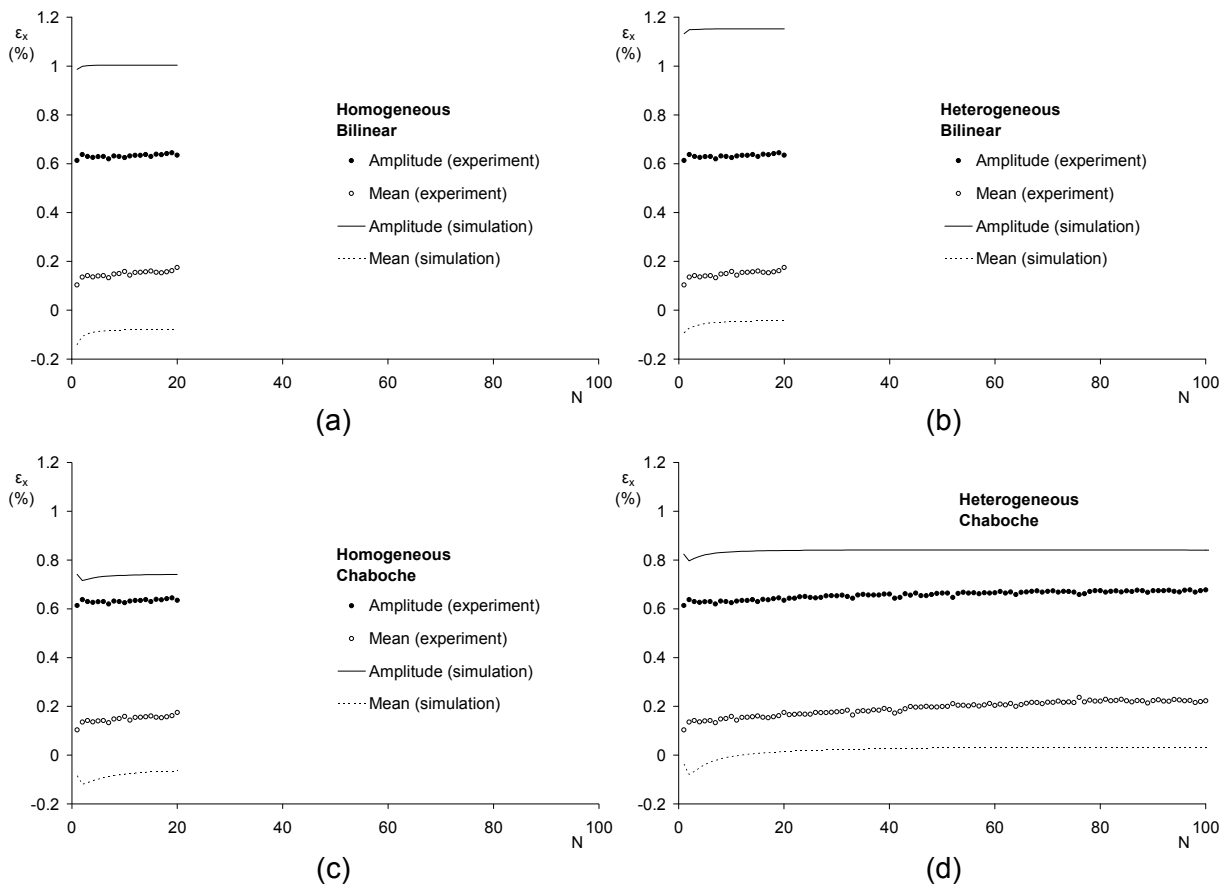


Fig. 4.16. Axial strain mean and amplitude responses on top pipe surface at 5mm from weld toe from experiment and simulations using various material types and models.

SIMULATION OF RESIDUAL STRESS RELAXATION

A new set of simulation is performed for a three-bead, quarter-sequence, SS304 welded piping joint by prescribing 10 mm amplitude displacement-controlled cycles. The Chaboche model in combination with the Voce hardening model and the heterogeneous material properties at the HAZ were used in this simulation. The initial residual stresses of the welded joints were computed using the method presented in Chapter 3. Initial residual stresses in three specimens, each fabricated with three-bead, quarter-sequence welding process, were measured at Oak Ridge National Laboratory (ORNL) using x-ray and neutron diffraction techniques. Subsequent to the initial residual stress measurements, these specimens were brought back to NC State University to conduct low-cycle fatigue tests by prescribing 10 mm displacement-controlled cyclic loads. One specimen was

subjected to 5 cycles, the other 20 cycles, and the third one 100 cycles, and residual stresses were measured again at ORNL. As mentioned in Chapter 3 that the x-ray diffraction technique was used to measure residual stresses on the surface, while neutron diffraction technique was used to measure residual stresses at 1mm depth from surface. X-ray measurements were made on all four fatigue life stages mentioned above, but neutron measurements were made only for before fatigue and 100 fatigue cycles. The simulation of residual stress relaxation has to include a final step for load relief. An example of loading path for one cycle displacement-controlled test is plotted in Fig. 4.17. When the displacement-controlled loading proceeds, force-displacement relationship follows the solid lines to end in point A of Fig. 4.17. After the test is done, the piping joint is removed for residual stress relaxation measurement. This removal procedure involves a linear relief of force at loading end, so the force-displacement relationship should follow the dash line to end in point B of Fig. 4.17. On numerical simulation, the relief of force can be simulated by switching the load control from displacement to force, and prescribing the zero force. This force relief step is added as the final step to all three residual stress simulations. These measured and simulated residual stresses at top surface of the pipe are plotted in Fig. 4.18.

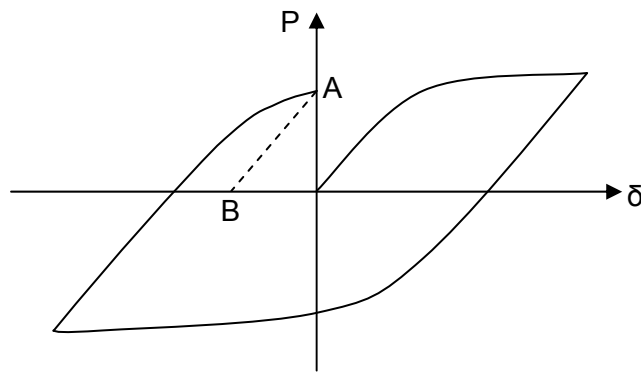


Fig. 4.17. Loading path at loading end of welded piping joints for residual stress relaxation measurements and simulations.

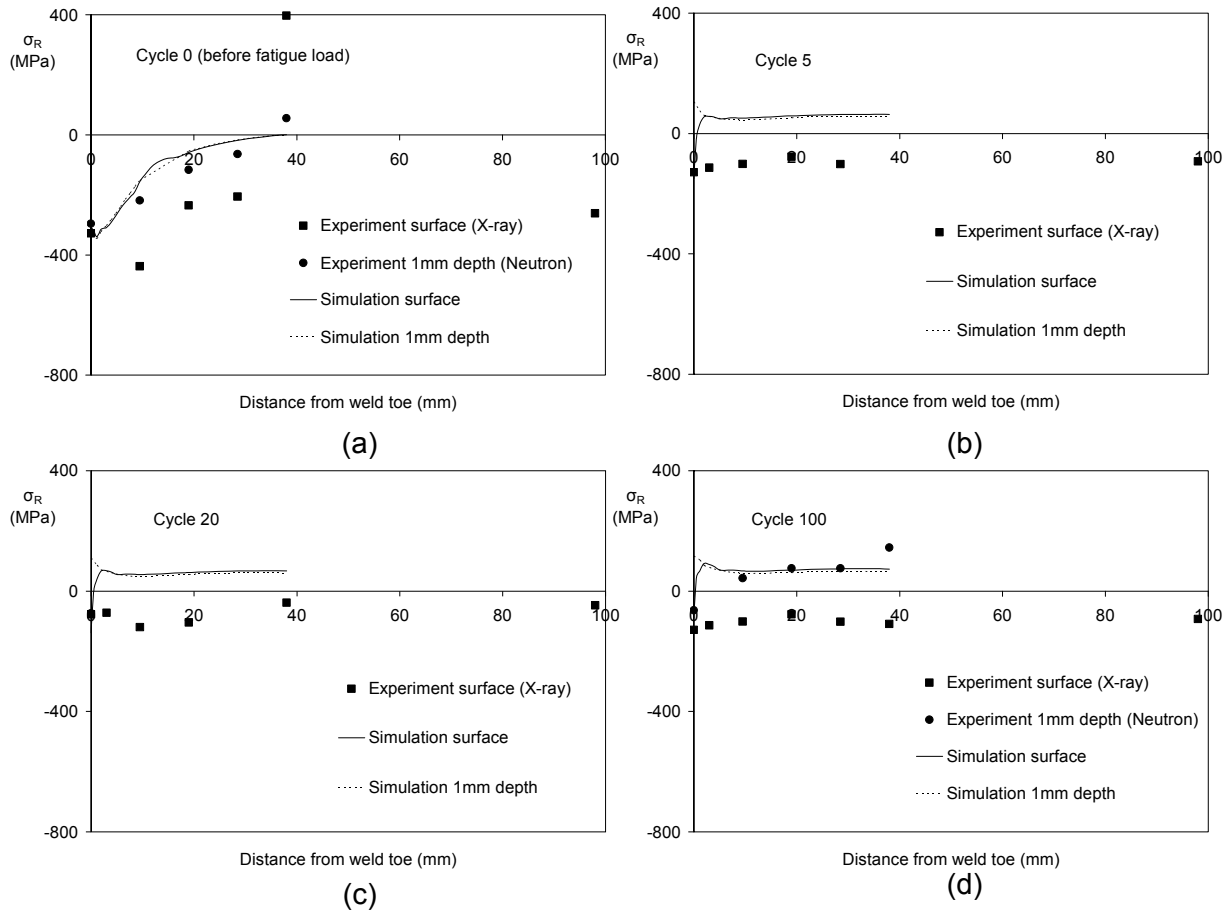


Fig. 4.18. Axial residual stress results on top from simulation and experiment (a) before fatigue loading, (b) after 5 cycles, (c) after 20 cycles, (d) after 100 cycles.

The comparisons of the simulated and measured residual stresses in Figs. 4.18a and 4.18d show that neutron diffraction measured residual stresses are simulated well by the finite element simulations for both before fatigue and after 100 fatigue cycles. These comparisons indicate that the x-ray diffraction measured residual stresses have an error bar of about 150 MPa. A possible reason for such big error is that the surface measurements using x-ray diffraction technique is susceptible to surface condition and thus is not so accurate as the neutron diffraction technique. The simulated and neutron diffraction measured residual stresses in Figs. 4.18a and 4.18d also demonstrates the relaxation of residual stresses with progressive fatigue cycles. The initial residual stresses in Fig.

4.18a were all compressive, but after five fatigue cycles the residual stresses at most locations becomes tensile. During the subsequent cycles, not much change in residual stresses is observed. One discrepancy observed between the simulation and measured residual stresses at the weld toe at 1 mm depth is that the measured residual stress seems to be compressive, whereas the simulated residual stress seems to be tensile.

INFLUENCE OF RESIDUAL STRESS ON FATIGUE RESPONSE

To understand the effect of initial residual stress on the weld toe strain responses under low-cycle fatigue loading, two more simulations for the experimental responses in Chapter 2 were performed. This experiment involved a 10 mm displacement-controlled cyclic loading prescribed on a three-pass, quarter-sequence, SS304 socket-welded piping joint. Both simulations were performed using the heterogeneous material properties at HAZ and the Chaboche model combined with Voce hardening model. The difference between these two simulations was that one simulation included the initial welding residual stresses while the other did not. The simulation that included the initial residual stresses was subjected to 100 cycles, whereas the other for 40 cycles.

Force-displacement simulations of the 1st cycle are compared to the experimental response in Fig. 4.19. Mean and amplitude force response in each cycle are plotted against the number of cycles and compared to experimental response in Fig. 4.20. In Figs. 4.19 and 4.20, the differences between the force responses from the two simulations are very small. Hysteresis loops from both simulations matches the experimental loop real well. Force amplitude from the simulation that included the initial residual stresses is closer to the experimental response than that from the simulation without the initial residual stresses. Again, the mean forces are simulated well by both cases.

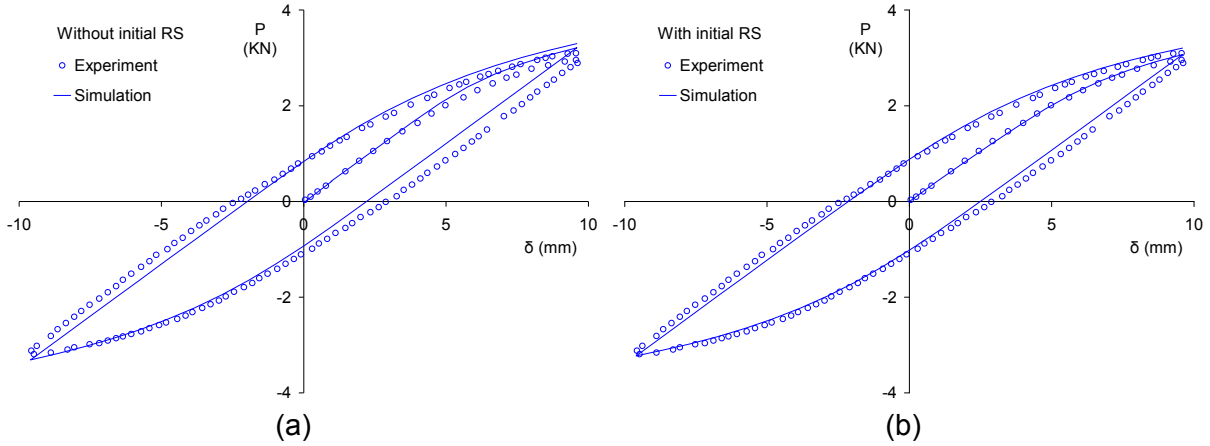


Fig. 4.19. Comparison of force-displacement responses from experiment and simulations; (a) simulation without initial residual stresses (b) simulation with initial residual stresses.

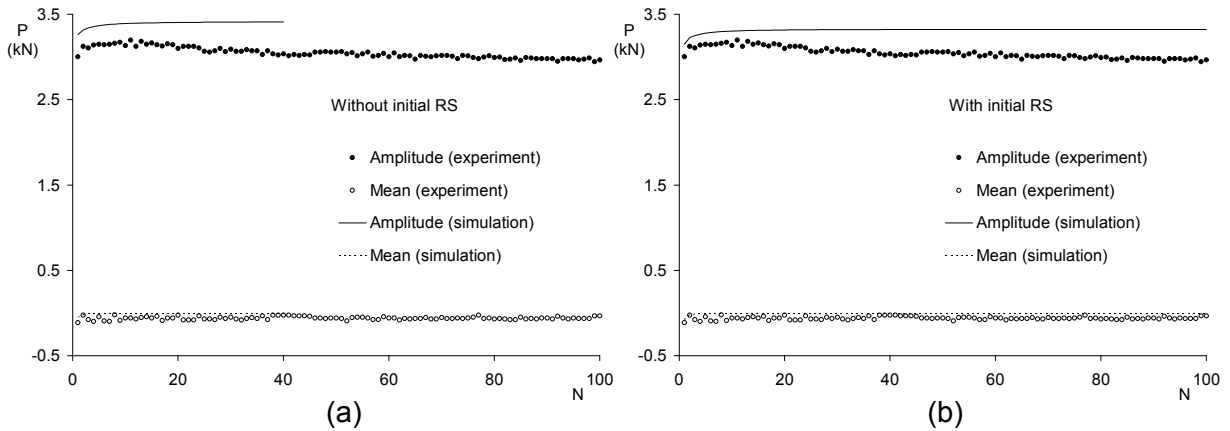


Fig. 4.20. Mean and amplitude force responses against the number of cycles from experiment and simulations; (a) simulation without initial residual stresses, (b) simulation with initial residual stresses.

Simulated and experimental axial strain responses at top pipe surface at 3, 19 and 38 mm away from the weld toe are compared in Fig. 4.21. The axial strain means from the simulation with the initial residual stresses is closer to the experimental responses better than that from the simulation without the initial residual stress (Fig. 4.21). In the latter simulation, the mean strains are zero at all three locations. That means, the metal around the weld toe does not ratchet in the absence of residual stress. The axial strain amplitudes from both simulations either overpredicts or underpredict the

experimental responses. Overall, the axial strain amplitude simulations without the initial residual stresses are better than the other simulation (Fig. 4.21).

Above simulations demonstrate that the residual stresses play an important role in determining the strain responses at the weld toe. First, no ratcheting response was observed in the simulation without the initial residual stresses as shown in Fig. 4.21a. Noticeable ratcheting only occurred at 3mm from weld toe in the simulation with the initial residual stresses. At this location the initial compressive residual stress could be the reason of negative ratcheting rate response. Second, the initial residual stresses influence the strain amplitude responses. Strain amplitudes at 3mm from weld toe increases significantly as the initial residual stresses are included in the analysis. On the other hand, strain amplitudes at 38mm from weld toe are not much different in the two simulations, which could be due to small or zero initial residual stresses away from the toe.

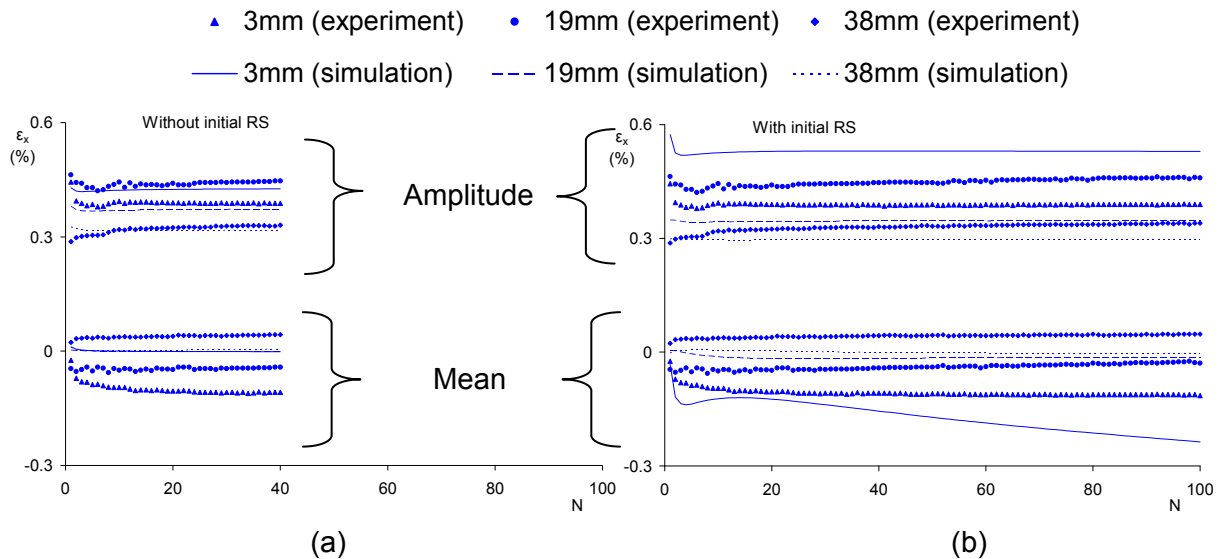


Fig. 4.21. Axial strain response at various distances (3mm, 19mm, and 38mm) from weld toe versus number of cycles from experiment and simulations of (a) without initial welding residual stress (b) with initial residual stress

Strain response at weld toe is also investigated because cracks at the weld toe were the main reason for fatigue failure of all our welded piping joint specimens. We do not have any measured strains at the weld toe because it was not possible to mount a strain gage exactly at the toe. Hence, only the simulation results are discussed here. The comparison of strain amplitudes and means at top weld toe from both simulations with and without initial residual stresses are shown in Fig. 4.22. Note in Fig. 4.22, the significant difference in the mean strain ratcheting rates between the simulations with and without residual stresses. First, the axial strain ratchets with a very small rate without any initial compressive residual stress present at the weld toe. However, in the presence of the initial compressive residual stresses, the axial strain ratcheting rate increases significantly. One reason for such a big difference in the ratcheting rates between the two simulations is the difference in the strain amplitudes as shown in Fig. 4.22. The strain amplitude increases significantly (1.2% to 3%) as the initial compressive residual stress is added. The strain amplitude does not change much as the cycle progresses but the ratchet continues with gradually decaying rate with progressive cycle, despite the fact that the residual stresses relax significantly within 5 cycles (see Fig. 4.18). It is quite surprising to observe that the strain ratcheting is occurring in the tensile direction while the residual stresses are compressive. Also note that the first peak of the axial strain response shifted by about 0.65% in the compression direction as the initial compressive residual stress is included in the simulation.

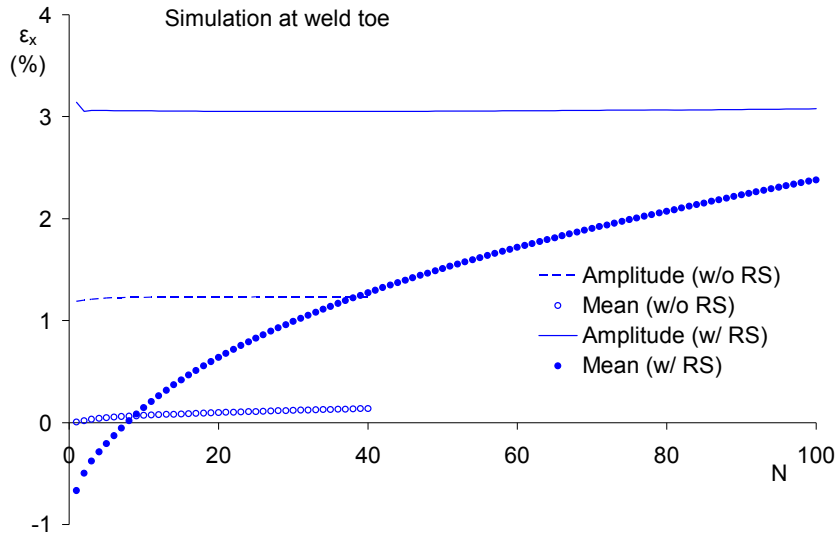


Fig. 4.22. Axial strain responses at the weld toe as a function of the number of cycles from simulations with and without initial compressive residual stresses.

To conclude the influence of initial residual stresses, force response is slightly influenced but the strain responses near weld toe are significantly influenced by initial compressive residual stresses. The first cycle axial strain mean was determined by the magnitude and sign of the initial residual stresses. The ratcheting rate in the subsequent cycle is significantly influenced by the initial residual stresses. Strain amplitude is also influenced significantly by the initial residual stresses.

CONCLUSIONS

Improved techniques for welded piping joint fatigue response simulation were presented. Three features of improving fatigue response simulation were discussed, and their implementations in the finite element analysis were introduced. Temperature-conditioned materials were tested to obtain heterogeneous material parameters for the Chaboche and Voce models. Convergence study was performed to determine optimum mesh and the need of using the quarter-point singular elements at the weld toe stress concentration location. Fatigue simulations using various material types and material models were performed, and the results were compared with the experimental data. The

simulations to study the residual stress relaxation were performed. Finally, the influence of initial welding residual stress on fatigue failure response of socket-weld joints is investigated. Important observations made from the study are summarized in the following.

1. The high temperature cycles from welding change the material properties at the HAZ.
2. The employment of quarter-point elements at the weld toe for fatigue simulation is essential.
3. The Chaboche model combined with Voce hardening model improve the weld toe strain response simulations significantly compare to the bilinear model.
4. Use of heterogeneous material properties at the HAZ can slightly improve ratcheting response prediction than using homogeneous material properties.
5. The combination of the heterogeneous material properties and the Chaboche model can simulate the residual stress relaxation well.
6. Under low-cycle fatigue loading, the initial axial strain mean and its ratcheting rate at the toe was determined by the magnitude and sign of the initial residual stresses. Significant tensile strain ratcheting and large strain amplitudes at the toe from the simulation with the initial compressive residual stresses indicates the reasons of the occurrence of fatigue crack exactly at the weld toe.

The strain responses at the HAZ from different simulations presented above could not predict the experimental responses well. A possible reason could be that the material heterogeneity at the HAZ was not simulated closely. The temperature change while conditioning the coupons was not as quick as at the HAZ during welding. Another improvement can be made by using advanced material model

with improved time- and temperature dependence. The advanced model should also be able to predict cyclic hardening and subsequent cyclic softening of a material.

CHAPTER 5

Conclusions and Recommendations

CONCLUSIONS

A systematic study of fatigue failure on welded piping joints under low-cycle fatigue loading was presented. The study consists of experiments and numerical simulations on specimens. The experimental part includes temperature measurement during welding, residual stress measurement, and fatigue loading test on welded piping joints. In addition, temperature-conditioning and cyclic loading test on tubular specimens were conducted to simulate material properties of heat affected zone. The numerical simulation includes temperature history simulation, residual stress simulation, and fatigue response simulation of welded piping joints. The research procedure and results are systematically presented in Chapters 2, 3, and 4. Each chapter contains conclusions of its part of study. A summary of all these conclusions is presented in the following.

Fatigue failure mechanism (Chapter 2)

The technique of using sequentially uncoupled nonlinear, transient, thermo-mechanical analysis for welding process simulation can predict the temperature history well and also calculate the initial residual stress representative of the experimental data.

The employment of bilinear kinematic hardening model on fatigue simulation could not predict fatigue strain response well. Material hardening behavior observed from experiments could not be simulated using bilinear model. In addition, strain amplitudes near weld toe were overpredicted.

Residual stress (Chapter 3)

A series of residual stress data were measured for welded piping joints. It was observed that the initial residual stresses at HAZ could be both large tensile and compressive and the magnitude of residual stresses is large near weld toe and decreases with distance from weld toe. The initial maximum compressive residual stress on top of stainless steel piping joints is higher than the yield stress of base metal, while the initial maximum compressive residual stress on carbon steel piping joints does not exceed the yield stress of base metal. Moreover, the axial residual stresses of stainless steel piping joints are mostly relaxed after 5 cycles. The residual stress relaxation in carbon steel welded joints is slower with fatigue cycles than in the stainless steel welded joints.

The change of mechanical material properties due to high temperature exposure was studied. It was obtained that some mechanical material properties like σ_0 and E' changed after subjecting to high temperature cycles, and the changed material was correlated to the peak temperatures. Thus, since peak temperature near weld is different at different location, the material near weld becomes heterogeneous. A modified thermo-mechanical material heterogeneity model was developed for residual stress simulation. The residual stress simulation using the modified model improved the initial residual stress prediction at the weld toe. Finally, the initial residual stress simulations were performed for four weld sequences, and the results illustrated that the initial residual stress distribution could be mainly determined by the welding start-stop location of the final pass.

Improved fatigue response simulation (Chapter 4)

In order to improve the fatigue response simulation obtained in Chapter 2, modifications of material properties and meshing were incorporated. One of the modifications is using heterogeneous material properties, which involves material tests on temperature conditioned coupons. Another modification is using the Chaboche model for fatigue response simulation. The material parameters

determined from the experimental data revealed that the parameters are changed by the conditioning temperature significantly. The third modification includes quarter-point elements for the stress concentration location.

The results of four fatigue response simulations using various material properties and modified model depicted that the heterogeneous material properties with the Chaboche model can simulate fatigue response and residual stress relaxation well. Simulations were performed to study the effect of the presence of initial welding residual stress on strain response. These results showed that the presence of initial residual stress influences strain amplitude and strain mean, both of which could influence the fatigue life of welded joints.

RECOMMENDATIONS FOR FUTURE RESEARCH

From the results of experiments and simulations in this study, some recommendations for future research are made in the following.

Using a proper method to measure strain response at weld toe is important, as weld toe is the location where crack initiates. Strain gages that were used in this study cannot be installed right at the weld toe due to geometry discontinuity. Another drawback of strain gage is the zero-shift which changes the ratcheting strain responses. Other strain measurement technique is needed to overcome these two problems.

The second suggestion is both strain gage and residual stress measurement related. As strain gages were installed on material surface using adhesive, the removal of strain gages would cause surface condition changes, which could influence the residual stress measurement using x-ray

diffraction method. It would be better if a strain measurement technique that does not alter surface condition of measurement locations could be used.

The third suggestion is about temperature-conditioning procedure on tubular specimens for material heterogeneity study. The temperature conditioning of tubular specimens to 1050°C in this study took about 5 minutes to reach desired temperature, which is slower than in the real welding approach that can heat up material to 1050°C in few seconds. The difference in heating rate could influence material properties after cooled down to room temperature.

The fourth suggestion for future research is to understand the effect of circumferential residual stress on strain response. The residual stress discussion in this study was mainly focused on axial direction because the crack initiates along circumferential direction. However, as the strain response in Fig. 4.22 of Chapter 4 is not clearly understood, the study of circumferential residual stress may be essential. This suggestion also involves the material model used on fatigue response simulation. A material model which can simulate well biaxial strain responses will be needed.

REFERENCES

- ABAQUS Version 6.4-3, Hibbitt, Karlsson and Sorensen, Inc., Pawtucket, RI, 2004.
- Abdel-Karim, M. and Ohno, N. (2000), "Kinematic hardening model suitable for ratcheting with steady-state", *International Journal of Plasticity*, Vol. 16, pp. 225-240.
- Abid, M. and Siddique, M. (2005), "Numerical Simulation of the Effect of Constraints on Welding Deformations and Residual Stresses in a Pipe-flange Joint", *Modelling and Simulation in Materials Science and Engineering*, Vol. 13, pp. 919-933.
- ANSYS Version 11.0, Swanson Analysis Systems, Inc., Houston, PA, 2007.
- Bari, S. and Hassan, T. (2000), "Anatomy of Coupled Constitutive Models for Ratcheting Simulation", *International Journal of Plasticity*, Vol. 16, pp. 381-409
- Bari, S. and Hassan, T. (2002), "An Advancement in Cyclic Plasticity Modeling for Multiaxial Ratcheting Simulation", *International Journal of Plasticity*. Vol. 18, pp. 873-894.
- Barsoum, Z. (2006), "Residual Stress Prediction and Relaxation in Welded Tubular Joints under Constant Cyclic Loading", *Materials Science Forum*, Vol. 524-525, pp. 323-330.
- Barsoum, Z. (2008), "Residual Stress Analysis and Fatigue of Multi-pass Welded Tubular Structures", *Engineering Failure Analysis*, Vol. 15, pp. 863-874.
- Blom, A.F. (1995), "Spectrum Fatigue Behaviour of Welded Joints", *International Journal of Fatigue*, Vol. 17, no. 7, pp. 485-491.

- Brickstad, B. and Josefsen, B.L. (1998), "A Parametric Study of Residual Stresses in Multi-pass Buttwelded Stainless Steel Pipes", *International Journal of Pressure Vessels and Piping*, Vol. 75, pp. 11-25.
- Chaboche, J.L. (1991), "On some modifications of kinematic hardening to improve the description of ratchetting effects", *International Journal of Plasticity*, Vol. 7, pp. 661-678.
- Chiarelli, M., Lanciotti, A. and Sacchi, M. (1999), "Fatigue Resistance of MAG Welded Steel Elements", *International Journal of Fatigue*, Vol. 21, pp. 1099-1110.
- Corona, E. (1996), Straight pipe ratcheting data developed at the University of Notre Dame (unpublished).
- Corona, E., Hassan, T. and Kyiakides, S. (1996), "On the performance of kinematic hardening rules in predicting a class of biaxial ratcheting histories", *International Journal of Plasticity*, Vol. 12, no. 1, pp. 117-145.
- Dong, Y., Hong, J.K., Tsai, C.L. and Dong, P. (1997), "Finite Element Modeling of Residual Stresses in Austenitic Stainless Steel Pipe Girth Welds", *Welding Journal*, Vol. 10, pp. 442s-449s.
- Duranton, P., Devaus, J., Robin, V., Gilles, P. and Bergheau, J.M. (2004), "3D Modelling of Multipass Welding of a 316L Stainless Steel Pipe", *Journal of Materials Processing Technology*, Vol. 153-154, pp. 457-463.
- Gosselin, S. (1994), "Proposed ASME Section XI Philosophy Related to Operating Plant Fatigue Protection", WRC Progress Report.
- Gosselin, S. (2008), "Fatigue in operating nuclear power plants components after 60 years", Workshop on U.S. nuclear power plant life extension research and development issues.

- Hassan, T. and Kyriakides, S. (1992), "Ratcheting in cyclic plasticity, part I: uniaxial behavior", International Journal of Plasticity, Vol. 8, pp. 91-116.
- Hassan, T. and Kyriakides, S. (1994), "Ratcheting of Cyclically Hardening and Softening Materials: I. Uniaxial Behavior", International Journal of Plasticity, Vol. 10, pp. 149-184.
- Hassan, T. and Kyriakides, S. (1994), "Ratcheting of Cyclically Hardening and Softening Materials: II. Multiaxial Behavior", International Journal of Plasticity, Vol. 10, pp. 185-212.
- Hassan, T., Corona, E. and Kyriakides, S. (1992), "Ratcheting in cyclic plasticity, part II: multiaxial behavior", International Journal of Plasticity, Vol. 8, pp. 117-146.
- Higuchi, M., Nakagawa, A., Iida, K., Hayashi, M., Yamauchi, T., Saito, M. and Sato, M. (1998), "Experimental Study on Fatigue Strength of Small-Diameter Socket-Welded Pipe Joints", Journal of Pressure Vessel Technology, Vol. 120, pp. 149-156.
- Humphreys, A.E. (2004), "Influence of Residual Stress on the Initiation of Fatigue Cracks at Welded Piping Joints", MS Thesis, North Carolina State University.
- Iida, K., Yamamoto, S. and Takanashi, M. (1997), "Residual Stress Relaxation by Reversed Loading", Welding in the World, Vol. 39, no. 3, pp. 138-144.
- Jiang, W., Yahiaoui, K., Hall, F.R. and Laoui, T. (2005), "Finite Element Simulation of Multipass Welding: Full Three-dimensional versus Generalized Plane Strain or Axisymmetric Models", Journal of Strain Analysis, Vol. 40, no. 6, pp. 587-597.
- Johnson, M.Q. and Ramirez, J.E. (2000), "Preliminary evaluation of heat affected zone toughness in structural shapes used in the construction of seismic moment frames", SAC Joint Venture, SAC/BD-00/13.

- Joseph, A., Rai, S.K., Jayakumar, T. and Murugan, N. (2005), "Evaluation of Residual Stresses in Dissimilar Weld Joints", *International Journal of Pressure Vessels and Piping*, Vol. 82, pp. 700-705.
- Kang, G., Li, Y. and Gao, Q. (2005), "Non-Proportionally Multiaxial Ratcheting of Cyclic Hardening Materials at Elevated Temperatures: Experiments and Simulations", *Mechanics of Materials*, Vol. 37, pp. 1101-1118.
- Krishna, S., Hassan, T., Naceur, I.B., Sai, K. and Cailletaud, G. (2009), "Macro versus micro scale constitutive models in simulating proportional and nonproportional cyclic and ratcheting responses of stainless steel 304", *International Journal of Plasticity*, accepted for publication in the international journal of plasticity.
- Lachmann, C., Nitschke-Pagel, Th. and Wohlfahrt, H. (2000), "Characterisation of Residual Stress Relaxation in Fatigue Loaded Welded Joints by X-Ray Diffraction and Barkhausen Noise Method", *Material Science Forum*, Vol. 347-349, pp. 374-381.
- Li, M. (1995), "An Experimental and Finite Element Analysis of Temperature and Stress Fields in Girth Welded 304L Stainless Steel Pipes", PhD Dissertation, Oregon Graduate Institute of Science and Technology, Portland, Oregon.
- Liu, Z. (1998), "A study on fatigue failures and design methods of piping welded joints", MS thesis, North Carolina State University.
- Lu, J., Bouhelier, C., Lieurade, H.P., Baralle, D., Miege, B. and Flavenot, J.F. (1994), "Study of Residual Welding Stress using the Step-by-Step Hole Drilling and X-Ray Diffraction Method", *Welding in the World*, Vol. 33, no. 2, pp. 118-128.

- Lu, P.C. (2001), "The FEM Based Calculation of Crack-tip Strain Rate for Determining the Crack Growth Rate of 304 Stainless Steel in BWR Environments", Nuclear Engineering and Design, Vol. 205, pp. 227-240.
- Lu, X. (2003), "Influence of Residual Stress on Fatigue Failure of Welded Joints", PhD Dissertation, North Carolina State University.
- Mochizuki, M., Hattori, T. and Nakakado, K. (2000), "Residual Stress Reduction and Fatigue Strength Improvement by Controlling Welding Pass Sequences", Journal of Engineering Materials and Technology, Vol. 122, pp. 108-112.
- Murugan, S., Kumar, P.V., Gill, T.P.S., Raj, B. and Bose, M.S.C. (1999), "Numerical Modelling and Experimental Determination of Temperature Distribution during Manual Metal Arc Welding", Science and Technology of Welding and Joining, Vol. 4, no. 6, pp. 357-364
- Murugan, S., Kumar, P.V., Raj, B. and Bose, M.S.C. (1998), "Temperature distribution during multipass welding of plates", International Journal of Pressure Vessels and Piping, Vol. 75, pp. 891-905.
- Murugan, S., Rai, S.K., Kumar, P.V., Jayakumar, T., Rai, B. and Bose, M.S.C. (2001), "Temperature Distribution and Residual Stresses Due to Multipass Welding in Type 304 Stainless Steel and Low Carbon Steel Weld Pads", International Journal of Pressure Vessels and Piping, Vol. 78, pp. 307-317.
- Nikitin, I. and Besel, M. (2008), "Correlation between Residual Stress and Plastic Strain Amplitude during Low Cycle Fatigue of Mechanically Surface Treated Austenitic Stainless Steel AISI 304 and Ferritic-Pearlitic Steel SAE 1045", Materials Science and Engineering A, Vol. 491, pp. 297-303.

Noyan, I.C. and Cohen, J.B. (1987), Residual Stress Measurement by Diffraction and Interpretation.

Materials Research and Engineering, pp. 75-116, 164-208.

Radaj, D. (1992), Heat effects of welding, Springer-Verlag, ISBN 3-540-54820-3

Rahman, S.M., Hassan, T. and Corona, E. (2008), "Evaluation of cyclic plasticity models in ratcheting simulation of straight pipes under cyclic bending and steady internal pressure", International Journal of Plasticity, Vol. 24, pp. 1756-1791.

Riccardella, P.C., Pan, S.H., Sullivan, M., Schletz, J. and Gosselin, S.R. (1998), "Vibration Fatigue Testing of Socket Welds", Pressure Vessel and Piping Codes and Standards, Vol. 360, pp. 453 -463.

Ruud, C. (2002), "Measurement of Residual Stresses", Handbook of Residual Stress and Deformation of Steel, pp. 99-117.

Shi, Y., Sun, S., Murakawa, H. and Ueda, Y. (1998), "Finite Element Analysis on Relationships between the J-integral and CTOD for Stationary Cracks in Welded Tensile Specimens", International Journal of Pressure Vessels and Piping, Vol. 75, pp. 197-202.

Smith, D.J., Farrahi, G.H., Zhu, W.X. and McMahon, C.A. (2001), "Experimental Measurement and Finite Element Simulation of the Interaction between Residual Stresses and Mechanical Loading", International Journal of Fatigue, Vol. 23, pp. 293-302.

Smith, J.K. (1996), "Vibrational Fatigue Failures in Short Cantilevered Piping With Socket-Welded Fittings", ASME PVP-Vol. 338, Pressure Vessels and Piping Codes and Standards, Vol. 1, pp. 21-24.

Teodosio, J.R., Fonseca, M.C. and Pedrosa, P.D. (2003), “Relaxation of Residual Stresses during Fatigue Cycles in Steels”, Materials Science Forum, Vol. 426-432, pp. 3981-3988.

Vecchio, R.S. (1996), “Fatigue Evaluation of Socket Welded Piping in a Nuclear Power Plant”, ASME PVP-Vol. 338, Pressure Vessels and Piping Codes and Standards, Vol. 1, pp. 25-41.

Virginia Power Company (1993), “Reactor Coolant System Loop Stop Valve Disk Pressurization Line Evaluation, North Anna Power Station, Units 1 and 2”, Report NP-2700, June.
(Restricted access).

Voce, E. (1955), “Practical strain-hardening function”, Metallurgia, Vol. 51, no. 307, pp. 219-226.

Webster, G.A. (2000), “Role of Residual Stress in Engineering Applications”, Material Science Forum, Vol. 347-349, pp. 1-11.

Withers, P.J. and Bhadeshia, H.K.D.H. (2001), “Residual Stress Part 1 – Measurement Techniques”, Material Science and Technology, Vol. 17, pp. 355-365.

Zhang, Y., Pratihari, S., Fitzpatrick, M.E. and Edwards, L. (2005), “Residual Stress Mapping in Welds using the Contour Method”, Material Science Forum, Vol. 490-491, pp. 294-299.